

**OPTICAL METHODS IN EXPERIMENTAL MECHANICS****Milan Držík,<sup>1\*</sup> Juraj Chlpík<sup>\*†</sup>***\*Department of Applied Optics, International Laser Centre, Ilkovičova 3, 841 04 Bratislava**†INPE, FEI Slovak University of Technology in Bratislava*

Received 31 March 2015, in final form 20 May 2015, accepted 21 May 2015

Optical metrology methods are an integral part of experimental mechanics. In this communication a systematic study of a variety of these methods is presented concerning the origin and subsequent development over the following period of a few decades. Particularly, the advancement of coherent light imaging in the field of diffraction optics based measuring procedures is described. Primarily, holographic/speckle interferometry used in surface deformation measurements in deformable body mechanics is treated from the viewpoint of optical scheme optimization. Topics such as image plane holography, pulsed ruby laser holography, electronic speckle pattern interferometry (ESPI) and double-channel speckle interferometry, hybrid experimental-numerical stress state analysis, light diffraction testing of surface roughness are discussed as well as their primary applications. Theoretical fundamentals and conditions for realization of each method are shown. The main aim of this study is to point out the basic features and potential exploitation of physical phenomena which are related to interference and diffraction of coherent light.

DOI: 10.2478/apsrt-2014-0002

PACS: 42.25.Hz, 42.30.Ms, 42.40.-i, 42.40.Kw, 42.40.My, 62.20.-x, 78.20.hb, 85.85.+j

KEYWORDS: Experimental mechanics, Holographic interferometry, Speckle interferometry, Electronic speckle pattern interferometry, Double-aperture speckle interferometry, Pulsed holography, Phase visualization, Micro-interferometry, Vibration analysis

**Contents****1 Introduction****103**

---

<sup>1</sup>E-mail address: drzik@ilc.sk

<b>2</b>	<b>Holographic interference method</b>	<b>105</b>
2.1	Holographic interferometry on transparent objects and objects with specularly reflected surfaces . . . . .	106
2.2	Pulsed laser holographic interferometry . . . . .	112
2.3	Holographic shearing interferometry . . . . .	117
2.4	Holographic interferometry and photoelasticimetry . . . . .	121
2.4.1	Polarisation holography . . . . .	124
2.4.2	Interpretation of interference pattern . . . . .	128
2.5	Visualisation of ultrasonic bending wave propagation . . . . .	129
2.6	Interferometrical evaluation of the temperature distribution inside transparency .	134
2.7	Membrane thickness mapping by Fizeau interferometry . . . . .	140
<b>3</b>	<b>Speckle interferometry</b>	<b>143</b>
3.1	Optical system of holographic/speckle interferometer . . . . .	143
3.1.1	Experimental application of interferometer . . . . .	157
3.1.2	Two-channel speckle interferometer . . . . .	160
3.2	Reconstruction of records in speckle interferometry using polychromatic light . .	161
3.2.1	Application conclusions . . . . .	164
3.3	Speckle interferometry by sandwich principle . . . . .	164
3.4	Speckle interferometry utilizing digitization of image . . . . .	167
3.4.1	Electronic speckle interferometry . . . . .	167
3.4.2	Double-aperture speckle interferometer with electronic record . . . . .	173
3.4.3	Experimental realization . . . . .	176
3.5	Diffraction of light on the surface microroughness . . . . .	176
3.6	Evaluation of elasto-plastic stresses by surface spectrum analysis . . . . .	184
3.6.1	Experimental results . . . . .	184
3.6.2	Separation of the principal strains . . . . .	188
<b>4</b>	<b>Laser and optical measurement techniques for testing in microelectronics</b>	<b>191</b>
4.1	Specular and diffuse-like reflected surface flatness testing . . . . .	191
4.2	Residual stress measurement of thin films, membranes and MEMS components .	199
4.3	Microinterferometry . . . . .	202
4.4	Vibration measurement of multilayer membrane-like microcomponents . . . . .	207
4.4.1	Visualization of different mode shapes of thin membranes . . . . .	210
<b>5</b>	<b>Conclusions</b>	<b>214</b>
	<b>Acknowledgement</b>	<b>214</b>
	<b>References</b>	<b>215</b>

## 1 Introduction

The role of experimental mechanics involves the measurement of material parameters and physical-mechanical characteristics, the non-destructive flaw detection tests and development or advancement of computational models as well as design of structures. Optical methods represent the most important methods among of experimental mechanics tools. Up to the 60-ies of the last century the only one tool practically useful for the purposes of experimental stress analysis was photoelasticity. Photoelasticity is an optical metrology tool which can be used for engineering purposes. It makes use of stress-induced birefringence in transparent polymeric materials and provides a relationship between the change in state of stress and strain-induced interference pattern. Photoelasticity can directly visualize only curves of principal stress difference and maximum in-plane shear stress.

An important impuls for the further development of optical methods was the advent of the laser light source. As the lasers with coherence light have become relatively accessible, it has stimulated the development of applications of laser technology including development of interferometrical measurements. The crucial in this respect was a tendency to apply for this purpose holography and afterward also speckle interferometry. Feasibility to use the holography for interferometric measurements was firstly demonstrated in 1965. After the first enthusiasm with observation of interference fringes resulting from double-exposure holographic record of the two states of deformation of the object, the problem was discovered, with correct interpretation of interference maxima and minima. Now, the interferograms were generated also on diffuse-like objects, the effect previously unknown for classical interferometry.

In this matter in terms of physical interpretations, work by Alexandrov and Bonč-Brujevič of 1967 [1] became fundamental. Authors announced the hypothesis that the arbitrary point of diffuse surface reflects light into all the directions, that is it reflects the light also in any chosen direction of observation. Thus, we can use the principle of path and consequently phase difference, as in the classical interferometry, where it was realizable only in the direction of specular reflection or passing through the transparent material. Another important finding was that, in the vicinity of the observed point, within the speckle conjugated to him, the light is spatially coherent. Therefore, the light from the area of two reconstructed hologram exposures may interfere with each other.

The capability to measure the displacement field on diffuse-like surface is one of the most important properties of holographic interferometry. Unfortunately, in the classic schema of Fresnel holograms record the path/phase difference evaluation is rather complicated. For each point of the object, solution of the system of linear equations is required for all the three orthogonal components of displacement. For this reason, further developments in this area were focused on the development of optical schemes of holographic interferometry with simplified direct optical separation of the three displacement vector components. By choosing the selected appropriate illumination angles of the measured object and its observation individual displacement components can be optically separated.

Typical examples of such appropriate arrangement of recording geometry are speckle interferometric methods. The key point in introduction of speckle interferometry was the publication of experimental results carried out by Burch and Tokarski in 1968 [2]. The experiments showed analogy between the diffraction effect on chaotically distributed identical structures and the diffraction on one of these structures. The photographic plate with two speckle fields shifted

one to another diffracts the laser beam in like manner as a screen with two openings away from each other to the same shift.

The methods of holographic interferometry as well as speckle interferometric principle found their place in many variations in solving problems of experimental mechanics, namely in experimental model testing evaluating stress/strain state. Applications for measurement of nonlinear material behavior but also for material testing in dynamic conditions was an indispensable part of the genesis of these methods over the past decades.

Now, optical experimental techniques have expanded from basic stress analysis of large structures or models to include the electromechanical analysis of micron-sized mechanical elements. Study of mechanical behavior of Micro Electro Mechanical Systems (MEMS) and microstructures by optical methods is undoubtedly promising approach for both inspection and diagnostic purposes. At the present state of art, there are various forms of experimental-analytical techniques which can be applied to mechanical/thermomechanical testing and characterization of microelectronics materials and components. Laser based and other optical metrology tools in this field owe much of their existence to noninvasive and contactless nature and also to the ability of easy depiction of microworld. Considering the employment of photoelectric sensing by photodiodes detectors or by CCD the dynamic periodic as well as one-shot surface motions can be successfully detected. Soon, such capabilities addressed the experiments to be used for the detection of forced vibrations of thin membranes and membrane-like components. The laboratory evaluation has been carried out to determine the mechanical stress state, frequency characteristics of thin layers damping properties.

Particular attention has to be dedicated to the optical principles which allow their realization for in-situ mode of operation. Conditions for immediate tracking of the process as a rule require the optical observation through the glass window from a longer distance or the device has to be installed and operating inside the vacuum chamber. However, in-situ measurements usually provide valuable information on thermal/mechanical characteristics discovering their evaluation.

The application of the well-known principles likewise the development of new procedures has proved as a tool to solve many issues connected with mechanical and even thermal characterization of microcomponents, particularly those of the MEMS. In this aspect, the Laser Doppler Vibrometry is shown to be a very perspective technique for such a purpose.

Nevertheless, the category of tasks solvable by optical techniques can be very large and irretrievable role falls to pointwise probing but also to the different variations of wide-field CCD based optical techniques. Thus, the specific features of optical sensing make use of the optics still promising in the field of experimental mechanics not only in solution of variety "non-standard" problems but also MEMS and microelectronics technologies applications.

## 2 Holographic interference method

The problem of complete assessment of 3-D displacement vector in holographic interferometry belonged to the most important and spotted problems of optical interference measurements. One of the unique properties of holographic interferometry is the possibility of phase comparison of wavefronts diffusely scattered off the body surface generally with 3-D shape. In the double-exposure hologram interferometry where the holographic plate is exposed twice, the changes of object induced between two exposures are visualized due to loading by mechanical stress, acoustic loading, temperature deformation and temperature or pressure change of transparent material refractive index.

Using the Fresnel type holographic scheme for double-exposure recording, the obtained displacements interference fringes e.g. provide information on surface points displacements without simplifying assumptions. The holographic record of interference fringes by conventional photographic procedure is a known and well-established method. In spite of that the double-exposure holographic interferograms mostly are limited into qualitative description of the studied problem showing that the quantitative determination of the three orthogonal components of the 3-D displacement vector is a troublesome and complicated task. The main reason is that the interference fringes formed provide information about the motion of object along the sensitivity vector. At each point of the object's surface the separated interference fringes include common information about all three orthogonal components. The separation of the components has to be carried out independently point by point by appropriate selection of three different directions of illumination and observation, respectively. Interference records evaluation by standard procedure came to be inaccurate in the case when one or two of displacement components are quite different compared to the others. The work of Alexandrov and Bonč-Brujevič [1] was crucial from the viewpoint of physical interpretation of the formed fringe patterns. In the work there was a hypothesis proved about the diffraction of light reflected off the diffuse-like surface as an optical phenomenon where every point on the surface scatters the light in each of spatial directions. It means that we can use the "standard" interferometrical principle of path difference determination in each of chosen directions. Another important physical factor is observation that in the vicinity of the observed point the scattered light is spatially coherent within the appertaining laser speckle, consequently, the light reconstructed from both the hologram exposures can interfere with one another. The mentioned notes lead to the possibility of quantitative evaluation of paths differences for all the points covered by interference pattern.

Nevertheless, to do it, we have to solve a system of three linear algebraic equations for each of the points. Such an evaluation is time consuming, hence in seventies, an effort to propose the optical scheme where the displacement components in a certain coordinate system considerably simplify the whole procedure of object deformation description emerged as a basic tendency of experimental studies. As a rule this demand called for direct optical separation of in-plane and out-of plane displacements. In experimental practice the description of the double exposure interferograms was based on the choice of suitable conditions of object illumination as well as angles of observation. Even today, there is not yet a simple and reliable quantitative method to obtain information on spatial displacements on objects. Fig. 2.1 illustrates the Fresnel type double-exposure holographic interferogram observed from two different angles of observation and illumination.

One of the unique properties of the lens is the feasibility to separate the spatial frequencies.



Fig. 2.1. Double-exposure Fresnel type holographic interferogram of the gun deformation between two subsequent shots. The interference fringes represent isolines of equal magnitude of deformations.

Using a lens to image a given object near the hologram recording plane creates a hologram in which the image of the object can be located near the hologram plane. Such an image-plane hologram has some specific features, one of them is the peculiarity of the reconstruction by white light illumination. However, when the developed hologram is illuminated at the reconstruction process we cannot be able to observe the image of the object immediately. Instead, the image restores only the lens aperture viewing angle through which the image-plane hologram was recorded. The reason is that at reconstruction we also reconstruct the quadratic phase factor which is associated with the imaging conditions. A real image of the object can be viewed along the optical axis of the image hologram recording scheme by reversing the reference beam through the hologram which needs an additional objective lens. It can be approved, when reconstructing the image-plane hologram, both the real as well as virtual images of the object occur at the same place, where the original real image of the object created by recording lens was situated. For interferometry use the most important property of such a hologram is the confinement of observation angles at the double exposure hologram recording by recording lens aperture.

Despite the relatively small effort in the field, the use of image-plane holography for holographic interferometry purposes was a promising trend namely in experimental mechanics. The tendency to separate the in-plane displacement components can be documented also by development of so-called holographic moire-interferometry, and namely variety of schemes of speckle interferometry but also combined methods based on image-plane holography which were carried out the following years.

## 2.1 Holographic interferometry on transparent objects and objects with specularly reflected surfaces

In classical interferometry two smooth wavefronts interact with each other because of differences in their path lengths. With regard that the appropriate temporal as well as spatial coherencies are needed to obtain a static interference pattern, the interfering wavefronts have to be reflected from glossy surfaces. As a result, classical interferometry is limited to measurements of only specularly reflected or nondiffusing transparent flat surfaces where the angles of illumination

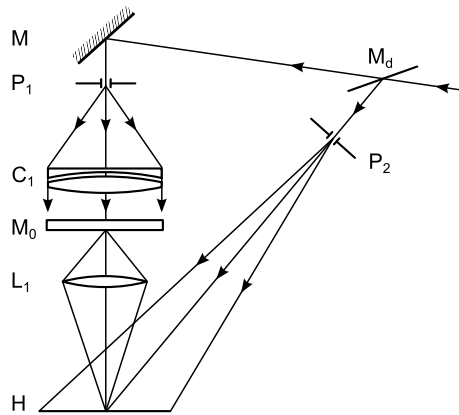


Fig. 2.2. Optical scheme of holographic interferometer for transparent object deformation measurement.  $M_d$  – semitransparent mirror, beamsplitter,  $M$  – mirror,  $P_1$  – collimator pinhole,  $C_1$  – collimating lens,  $M_0$  – transparent object,  $L_1$  – well corrected imaging lens,  $P_2$  – reference beam pinhole spatial filter,  $H$  – holographic plate.

and observation are limited by mirror-like reflection. Thus, there is no possibility to obtain information e.g. on in-plane displacements.

In the field of experimental mechanics, where the study of mechanical stress state is of primary importance, model experiments are frequently utilised. For a long time a typical example was an application of interferometry to study the deformation of loaded planar models in the state of plane stress or strain conditions. Using the transparent models (made of e.g. plexiglass or polymeric resins), the transversal deformation has been interferometrically measured. From the theory of elasticity, the resulting interference fringes can be simply interpreted. In many applications it is not necessary to watch the information on in-plane surface displacement components. When a non-diffusing object with mirror-like surface or transparency is illuminated from behind by a coherent wavefront and the hologram is then made by interference with reference beam, the reconstructed image will contain no speckle structure. Therefore, an optical scheme of image-plane holography can be adjusted, where the holographic interferometer acquires several specific features. In order to study in detail the state of stress in planar models made of polymeric transparent materials, we have developed the optical setup as it is drawn in scheme of Fig. 2.2. The coherent beam of laser light is divided by a semitransparent mirror  $M_d$  into two parts. For optimal adjusting, the continually variable mirror beamsplitter has been used. The laser sources used were mostly He-Ne CW lasers with output power 40 mW to 60 mW with coherent length of 20 cm to 80 cm. In the schematics  $P_1$  and  $P_2$  are the spatial filters of pinholes. Spatial filters are the point-like sources of both the information and the reference waves. The plane wave of a larger diameter created by a collimator  $C_1$  is passing through the studied model.  $L_1$  denotes the imaging set which is projecting the model image into the plane of holographic plate  $H$ . To record the holographic scenes with transversal dimensions of several centimeters, the well corrected objective lenses were used with focal distance 100 mm to 200 mm and the aperture number of 1/2.8. The setup shown does not use any ground glass in the information

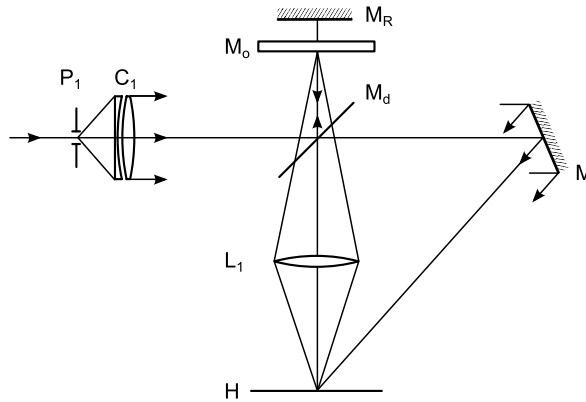


Fig. 2.3. Double-passed holographic interferometer for transparent object deformation measurement providing twofold sensitivity.  $P$  – point-like light source pinhole,  $C$  – collimating objective lens,  $M_d$  – semi-transparent mirror,  $M$  – information wave mirror,  $M_R$  – reference wave mirror,  $M_0$  – transparent object,  $L_1$  – well corrected imaging objective lens,  $H$  – holographic plate.

wave, thus, no speckle effect is visible in the hologram. Another alternative of the groundglass free scheme is drawn in Fig. 2.3. In this case, the information beam is created after the reflection from semitransparent mirror  $M_d$  and its subsequent passing through the transparent model. After passing through, the beam is reflected again from the flat mirror  $M_R$ , thus, the double passing of the wave through model is realized. Compared with the previous scheme, the setup provides favourable twofold sensitivity of the model thickness measurement.

The optical ray tracing in both the schemes requires the diameter of the imaging lens to be slightly larger than the measured area of the model. Moreover, care must be taken when the observed planar model gradients of thickness variations are too strong and the rays passing through the transparency are deviated beyond the imaging lens boundaries. In mechanics, the points with stress singularities (e.g. crack tip or load points) are often the case. Lack of speckle structure in this type of holograms offers for such a strong stress gradients another benefit in the possible big enlargement of the recorded object images-interferograms. These interferograms thus, can be postprocessed and studied in detail point by point. The maximum magnification is limited only by the resolving power of the optical system of the holographic recording.

Holograms generated in the image plane of the imaging system rank in a specific class of the holographic records with a number of positive properties when using it as an interferometrical tool. The lack of speckle structure can be revealed in microscope where only a system of dense fine fringes is visible. Note that to view the grating, a microscopic objective with a relatively strong aperture number has to be used, to catch the angle larger than the angle between the information beam and the reference beam.

During hologram reconstruction we have interference fringes localized in the plane of hologram which are in fact the same as moire fringes originated by overlapping both the fine microscopic interference gratings belonging to two holograms of the double exposure. When the hologram is reconstructed, the positions of gratings intersections do not diffract the light effec-

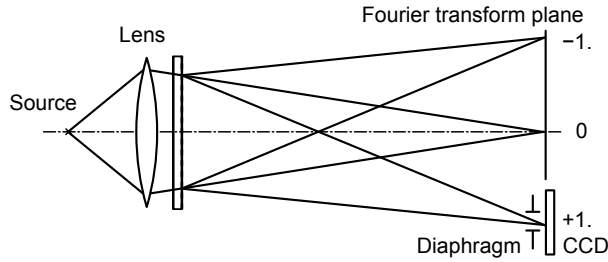


Fig. 2.4. Schematic of image-plane hologram reconstruction using point-like light source.

tively, hence they correspond to interference minima of the fringe pattern. The coincidence of the plane of interference fringes localization with the hologram plane allows us to use for reconstruction the source with weak coherency, actually even the white light extended sources based on incandescent lamps can be used. This is one of the unique features of all the image-plane holograms.

However, the reconstruction procedure especially when not large but the point-like light source is used, has to be modified in order to compensate the quadratic phase factor existing in the plane of hologram. Illuminating of the hologram by a replica of the reference beam will reconstruct only the lens through which we may observe the object. The reason is that we reconstruct also the quadratic phase factor associated with the imaging condition. The use of imaging lens to project the object image into optically conjugated image plane transforms the parallel wave into convergent spherical wavefront and the image formation is described by a complex amplitude where the phase factor of the spherical wavefront is present. At reconstruction, when the developed hologram is illuminated by a complex conjugate wavefront of the reference wave, we can observe a real image of the object full-area of which is illuminated. In practice, the most convenient way is to set a scheme as in Fig. 2.4.

Double exposure holograms obtained by optical setup in Fig. 2.2 or Fig. 2.3 give the interference pattern with infinite interference fringes which are analogous to fringes produced by classic interferometry principles. In principle, also finite fringe pattern can be obtained if one of the holographic interferometer mirrors is slightly tilted between exposures.

Nevertheless, the fundamental benefit of the holographic record is its differential nature, where the two true shapes of the object wavefronts are each other compared. Seeing that the fringes at double exposure are created as an optical paths difference between the real not an ideally planparallel transparent or a flat surface unloaded model shape with the shape loaded and deformed, the fundamental problem of classic interferometry in experimental mechanics is completely avoided.

Interference fringes on the planar models are created as an optical path difference between the state of model thickness before and after the loading deformation. Intensity distribution of two interfering waves is described by the well-known expression

$$I(x, y) = 2a^2 \left[ 1 + \cos \frac{2\pi}{\lambda} (l_2(x, y) - l_1(x, y)) \right], \quad (2.1)$$

where  $a$  is the amplitude of both the interfering waves  $l_1(x, y)$ ,  $l_2(x, y)$  and  $\lambda$  is the light wavelength. The path difference in the transparent model with initial thickness  $h$  and the refractive index  $n_0$  can be expressed

$$l_2(x, y) - l_1(x, y) = h\Delta n - (n_0 - 1)\Delta h, \quad (2.2)$$

where we have omitted the term  $dn_0 dh$  as a negligible value, and the refractive index of the ambient air is equal 1. The basic relationship to interpret the interference pattern follows from the elasticity equation for transverse deformation at the state of plane stress

$$\Delta h = -\frac{\nu h}{E}(\sigma_1 + \sigma_2), \quad (2.3)$$

where  $\sigma_1 + \sigma_2$  is the sum of principal stresses and  $E$  and  $\nu$  are the material parameters – Young's modulus and Poisson's ratio, respectively. If we assume optically isotropic transparent material with negligible birefringence properties (e.g. plexiglass), the proportionality follows from Maxwell-Neumann law between the sum of principal stresses and the change of refractive index induced by loading

$$\Delta n = C_0(\sigma_1 + \sigma_2), \quad (2.4)$$

where  $C_0$  is the optical constant of optically isotropic material. After substituting into Eq. (2.1) and taking into account the interference extreme condition

$$l_2(x, y) - l_1(x, y) = N\lambda, \quad (2.5)$$

we obtain the expression for the sum of principal stresses in the form

$$\sigma_1 + \sigma_2 = \frac{\lambda}{C_0 + (\nu/E)(n_0 - 1)} \cdot \frac{N}{h}, \quad (2.6)$$

where  $N$  is the interference order. As seen from this expression for interference fringes interpretation, the quantitative values of principal stresses depend on fundamental material as well as optical constants. That is, for every interference fringe order which is in the case of planar model under plane stress condition of Eq. (2.3) so-called isopachic fringe, the stress value can be assigned by using the fringe value  $c_h$  and the thickness of the planar specimen  $h$

$$\sigma_1 + \sigma_2 = c_h \frac{N}{h}. \quad (2.7)$$

The interference sensitivity constant – fringe value is composed of two main parts, material and optical. For that reason the best way how to determine this coefficient for assigning stresses to the measured deformation is the calibration experiment on the specimen with known stress distribution. The static value of the fringe value for material of polymethylmetacrylat (PMMA) Acrylon has been measured by well defined loading of plexiglass beam with dimensions  $300 \times 45 \times 6 \text{ mm}^3$  in pure bending. From density of interference fringes of isopachics on the plexiglass (PMMA) beam the fringe value  $c_h = 8.7 \times 10^3 \text{ Nm}^{-1}$  at the wavelength  $\lambda = 633 \text{ nm}$  was determined.

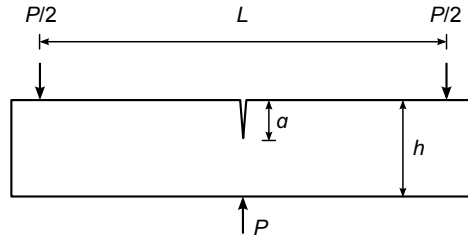


Fig. 2.5. The specimen of PMMA beam with simulated crack.

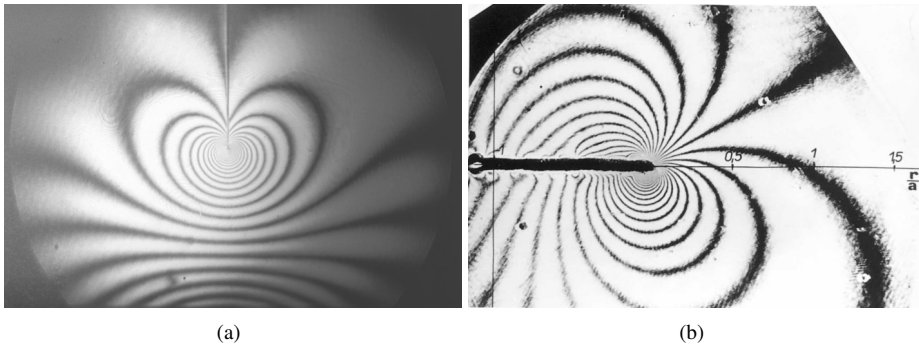


Fig. 2.6. Interference fringes of equal thickness change around the loaded crack, (a) crack perpendicular to the beam edge loaded by bending, (b) crack inclined to the load direction in the beam constantly loaded in tension.

The essential attribute of the holographic interferometry success is the comparative working principle which takes off the necessity of using precise optics and planarity or flatness of the measured models. In the last thirty or forty years in the field of mechanics, an intensive attention has been devoted to study the circumstances of the mechanical failures caused by the presence of cracks. We have proposed and carried out a number of applications to study such singular stress concentrators where cracked specimens made of plexiglass transparent material have been mechanically loaded and the stress distribution was evaluated. Experimentally the interferometric patterns of isopachics (see Eq. (2.7)) have been recorded in the setup schematically outlined in Fig. 2.2. For better imagination, one of the models with simulated crack is depicted in Fig. 2.5, also models of plates in tension have been measured. The specimen thickness varied for different specimens between 5 mm to 10 mm, for measurement in immersion liquid the thickness of 16 mm was used. The thickness of the loaded beams was chosen from the requirement of fulfilled plane stress conditions at once with enough interferometrical sensitivity of fringes formation. An example of the typical interference patterns around the crack tip under bending loading of the beam are in Fig. 2.6 where the loading of perpendicular and also inclined crack is visible.

As it was explained above, see Eq. (2.1) to Eq. (2.6), the comparison of two wavefronts

passing through the unloaded model and through the model after transversal deformation, a light field distribution with the intensity  $I$  is obtained by simple alteration of these expressions

$$I \sim \cos^2 \left[ \frac{\pi}{\lambda} \left( C_0 + \frac{\nu}{E} (n_0 - 1) \right) hS \right], \quad (2.8)$$

where by  $S$  the sum of principal stresses was denoted. Knowing the functional dependence of individual components in analytical expression or from numerical modeling of the mechanical problem, the invariant of principal stresses can be simply experimentally evaluated. Particularly, in fracture mechanics the analytical solution of the stress state in a vicinity of crack was expressed by [3] in form of infinite series. For tensile mode of crack loading it holds

$$\begin{aligned} \sigma_x &= \sigma_{xs} + O(r), \\ \sigma_y &= \sigma_{ys} + O(r), \end{aligned} \quad (2.9)$$

where  $\sigma_{xs}, \sigma_{ys}$  are the singular terms reciprocally related to square root of radial distance from the crack tip [4] and  $O(r)$  denotes polynomial series of the order  $r$ . Assuming that the fringe pattern formation is governed by the asymptotic stress field near the crack tip, the geometry of the fringe pattern can be expressed according to Eq. (2.7) by the summation of principal stresses

$$S = c_h \frac{N}{h} = \frac{2}{\sqrt{2\pi r}} K_I \cos \frac{\theta}{2} + O(r), \quad (2.10)$$

where  $\theta$  is the polar angle of the point with respect to crack paths line,  $r$  is the polar distance from the crack tip and  $K_I$  is the stress intensity factor of the first mode of crack loading. When the crack walls are loaded also in shearing mode

$$S = \frac{2}{\sqrt{2\pi r}} \left( K_I \cos \frac{\theta}{2} - K_{II} \sin \frac{\theta}{2} \right) + O(r), \quad (2.11)$$

where  $K_{II}$  is the stress intensity factor of the second mode of crack loading. The stress intensity factors are a function of the applied load, the geometry of the specimen, and the length of the crack. For quantitative evaluation they have to be determined by numerical simulation.

As it is clearly seen in the examples of the fringe pattern, in the area of crack tip, the fringes are too dense and in these figures even unresolvable. Nevertheless, if a wide open objective lens with better numerical aperture is used to photograph the reconstructed image, we can enlarge the crack tip vicinity in detail. Experimental technique used allows to observe the thickness changes up to the distance of some tenths of mm from the crack tip. In Fig. 2.7 even shape of small plastic zone is visible.

## 2.2 Pulsed laser holographic interferometry

Investigation of dynamic processes in mechanics is one of the most complicated tasks of experimental mechanics. Holographic interferometry, using pulse laser as a coherent source, can be regarded as an effective tool to study a variety of dynamic phenomena. The primary requirement for a pulse holography is the laser source with increased both spatial and temporal coherencies and with the pulse time dependence in the range of at least nanoseconds. In the experiments we used the laser with ruby crystal and passive Q-switch. The energy of one flash was about 0.1 J without modulation or 0.025 J with application of Q-switch. In this series of experiments,

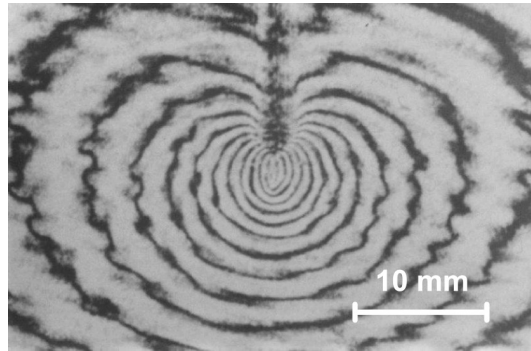


Fig. 2.7. Enlarged detail of the crack tip with plastic zone. Apple-like shape of the fringes is clearly deformed.

the problem of stress distribution at fracture of the fast propagating crack was studied. Theoretical solutions cannot completely explain some of the effects, such as non-elastic deformation, accumulation of micro-defects, discontinuity of the cracking process etc. The local flaws in the fracture process zone as well as the properties of material play a significant role, thus, the results of the interferometry with high spatial resolving power measuring close vicinity of the running crack tip could be a useful addition. As previously on planar transparent models, to observe isopachics interference fringes, the experiments were carried out by the optical arrangement of an interferometer, where the diffusor screen is not included, and the recorded interference pattern can be considerably magnified. The double-exposure holograms were taken by a pulsed ruby laser with the output power of  $\sim 50$  mJ at wavelength  $\lambda = 694.3$  nm. The lack of ground screen enables to arrange correlative matching parts of the viewfield area of both the reference and information beams in order to be overlapping on the holographic plate. Any possible imperfections in spatial coherency of the laser beam can thus be eliminated. To adjust such an optical setup, one flat mirror and converging lens were introduced in the reference beam which upturned the beam. As a result, the diffraction sensitivity of holographic records was excellent even without using any bleaching process. In addition to application of color filter KC-19 as a passive Q-switch, the ruby laser was put to use in automodulation mode. As known [5, 6] at the threshold generation even Q-switch-free laser resonator generates only one or a few successive pulses. The typical width of these peaks was about 100 ns with  $8 \mu\text{s}$  to  $15 \mu\text{s}$  time intervals between possible ensuing pulses. These laser pulses show a good coherency. On the other hand, automodulation mode arises as a result of thermal deformations of the ruby crystal, thus, the main drawback of this mode of operation is its considerable instability.

The catastrophic propagation of cracks is observed on the three-point bending specimens. These slender beams with the thickness of 4 mm were cut from the sheets of plexiglass (PMMA). Crack movement starts from an initially short blunt notch by the acting loading force generated after releasing a preliminary compressed strong coil spring. Mechanical releasing of the spring initiates not only the external load, but also triggers the countdown in the synchronisation block of the laser. Time delay circuit also reads a scheduled time interval in the range of  $20 \mu\text{s}$  to

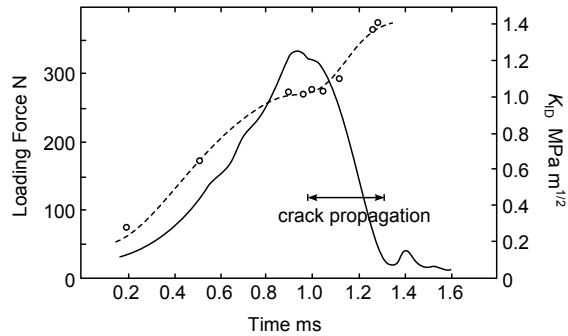


Fig. 2.8. The determined values of dynamic stress intensity factors  $K_{ID}$  (dashed line) determined from isopachics data and the time development of the loading force  $P$  (solid line).

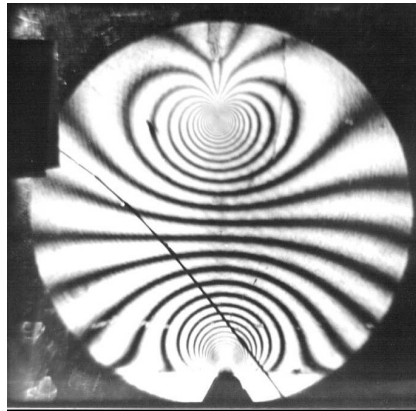


Fig. 2.9. Instantaneous dynamic deformation in a beam made of PMMA at the moment of cracking.

1200  $\mu\text{s}$  during the crack propagation. Before that, the first exposure of the hologram is carried out at unloaded specimen. The sequence diagram is as follows: After triggering, the external load increases as shown in Fig. 2.8, where the time history of the load for the whole beam cracking process is drawn. It can be seen that the loading force grows monotonically and passes a critical region when the crack starts to propagate. The loading time to initiation of the fracture takes about 1 ms, that is the quasi-static conditions before rising of the crack are guaranteed and the influence of the stress waves reflected from boundaries of the specimen is negligible. After a time interval, the crack reaches a position at which the second laser pulse is flashed. At this second exposure, interference fringes of an instantaneous deformation around the crack are recorded. Fig. 2.9 shows the fringes in the region of propagating crack where also the instantaneous deformation around point like load is visible. Crack tip speed at the moment of the second exposure is determined by reading on an oscilloscope screen of time intervals between breaking of conductive graphite lines drawn on the beam surface.

In Fig. 2.8 the development of the stress intensity factor value determined individually for several cracks with different propagation velocities is also plotted. The values of stress intensity factors are determined by analysing of isopachics fringes according to the above described method based on sum of principal stress determination for plane stress condition. The catastrophic crack growth is a fast dynamic process where the velocity of stress waves in solid material could be important. To evaluate the dynamic stress state, two main factors have to be pointed out. If the crack tip propagates very fast, the velocity of stress wave cannot be regarded as infinite and we have to study the equations for elastic body with terms which define the dynamic inertial influence. The value of the first invariant, under the assumption of constant crack tip velocity, is found by [7] and [8] from the relationship

$$\sigma_x + \sigma_y = (s_2^2 - s_1^2) [\phi_1(z_1) + \phi_1^*(z_1)] , \quad (2.12)$$

where  $\phi_1(z_1)$  is the complex potential function, and

$$s_j = \left[ 1 - (\dot{a}/c_j)^2 \right]^{-1/2} , \quad j = 1, 2 , \quad (2.13)$$

where  $c_2, c_1$  are the velocities of shearing and longitudinal stress waves,  $\dot{a}$  is the crack tip velocity. Assuming the complex stress function  $\phi_1(z_1)$  in the form of series we get expression for stress intensity factor in dynamic propagation conditions as it was defined by [7]

$$K_{ID} = \sqrt{2\pi} \frac{4s_1s_2 - (1 + s_2^2)^2}{1 + s_2^2} A_1 . \quad (2.14)$$

After a short analysis of this expression, when real values of maximum crack tip velocities are regarded i.e. the value of  $\dot{a}/c_R$  does not exceed 0.2 to 0.3, then a very small dynamic correction factor of a few percent can be found. As a rule, such a small dynamic correction is of the order of experimental uncertainty and of measurement errors. The strong viscoelastic properties of polymers including such as PMMA, are much more important factor. Also PMMA presents strong strain rate dependence. An assessment of the influence of viscoelasticity on the observed strain field is experimentally complicated particularly due to change of the fringe value  $c_h$  described by Eq. (2.6) and (2.7). For dynamic conditions this fringe value must be corrected.

The concept of linear viscoelasticity is based on the approximate relationship between the time dependences of the stress and the strain values. For a stress gradient of amplitude  $\sigma_0$  which oscillates sinusoidally with a constant frequency  $\omega$ ,

$$\sigma(t) = \sigma_0 \exp(i\omega t) , \quad (2.15)$$

the material response can be written in the form

$$\varepsilon(t) = \varepsilon_0 \exp[i(\omega t - \varphi)] , \quad (2.16)$$

where  $\varphi$  is the phase angle of time delay of  $\varepsilon(t)$  after  $\sigma(t)$ . The effective complex modulus of the material is defined as

$$E = E_1 + iE_2 = \frac{\sigma_0}{\varepsilon_0} \exp(i\varphi) . \quad (2.17)$$

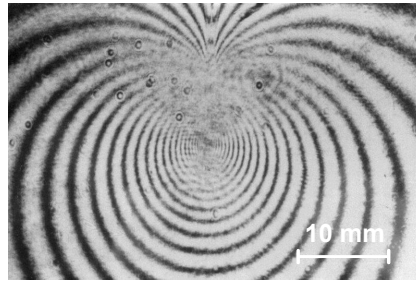


Fig. 2.10. Instantaneous dynamic deformation in the near vicinity of crack tip running with velocity  $400 \text{ m s}^{-1}$  at the moment of cracking.

As a result, the constant phase shift over the whole field causes that the strain field is followed by the same spatial stress distribution, consequently, the fast propagating crack tip is situated in a medium which seems to be increasingly stiff. This effect is clearly identified by a simple analysis of the shape and spatial distribution of transversal deformation around the near vicinity of a running crack tip as seen in one of the recorded examples of the beam cracking (Fig. 2.10). This is the case of crack tip velocity of about  $400 \text{ ms}^{-1}$ . As it is demonstrated when we are moving along the crack path, the layout of individual fringe curves shows the shift of the curves one after the other in the crack propagation direction. The curves, and therefore the deformation, further away from the point of crack tip get behind those of close to the crack tip. Moreover, as there is an opportunity to enlarge the hologram to the considerable extent, a scene at the nearest crack tip vicinity can be closely viewed. The immediate region is noticeable, although fringes are slightly blurred due to finite exposure time 60 ns to 80 ns of the laser flash pulse.

The quantitative stress-strain relation is described by the complex modulus of material for the given frequency of the oscillation or loading pulse. Then the fringe value  $c_h$  of Eq. (2.7) can be corrected knowing the quantitative changes of this modulus. The deviations of the parameters  $\lambda$ ,  $n_0$  and  $C_0$  as well as Poisson's ratio in the situation of fast varying loading are negligible as it is known from many experimental measurements. Hence, the most important parameter becomes the modulus  $E$ . Since the dynamic value of Young's modulus depends on the loading frequency, it is necessary to find relationship between the crack tip velocity and the time history of deformation near the crack path. An assessment has been performed on the assumption that for a material near the moving crack path the time dependence of deformation appears as a stress pulse [9]. Provided that the crack speed is nearly constant, the deformation around the fast running crack tip may be used to determine the time history of the material loading pulse. The typical frequency of this pulse is obtained by a spectral analysis. Fig. 2.11 presents the shape of stress pulse for the example of fracture at the velocity of crack tip propagation of about  $400 \text{ ms}^{-1}$ . The spectral content of the pulse is concentrated around the maximum of about 41 kHz. The quantitative value of the modulus of elasticity in the region of such frequencies exceeds 6.18 MPa [10], in comparison with its static value of 3.12 GPa. The dynamic fringe value for isopachics evaluation exceeds its static counterpart by 43%. Using the corrected fringe values true values of dynamic stress intensity factors were determined for different crack tip velocities. The results are drawn in Fig. 2.8.

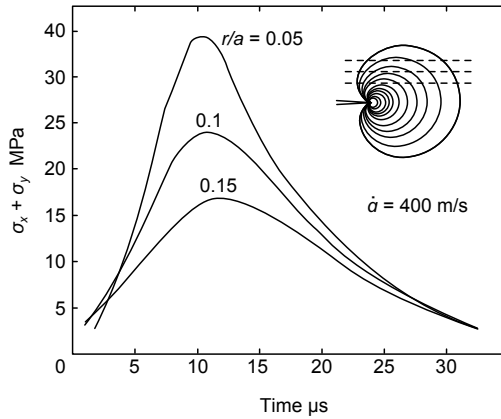


Fig. 2.11. Stress pulse near the crack path produced by a passing by crack tip.

### 2.3 Holographic shearing interferometry

Shearing interferometer has been utilized for years in the optical industry as one of the testing tools. Its usefulness was approved particularly in testing of aberrations of spherical as well as aspherical optics elements. Besides this, the principle of interferency of mutually shifted identical wavefronts belongs to optical methods which are being used for measuring deformation of the surfaces with mirror like reflection of light. This approach has shown to be useful also for the investigations in experimental mechanics. Namely the possibility to measure directly the slope contours formed due to mechanical or thermal load of the initially flat surface is important because of the direct relationship of the surface slopes and the moments, according to the theory of thin plates (see Fig 2.12). But, the interference patterns obtained by shearing interferometry have been exploited in investigation of cracks or various mechanical defects, as well. From the point of view of the wavefront shear realization there are many ways how the shearing interferometer

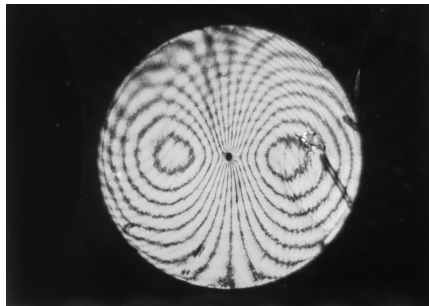


Fig. 2.12. Slope contours of the centrally loaded plate obtained by double-exposure holographic shearing interferometry.

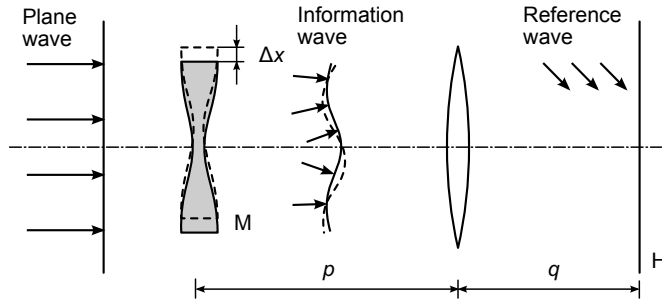


Fig. 2.13. Optical scheme of holographic shearing interferometry. The shift of object position between two exposures is  $\Delta x$  [11].

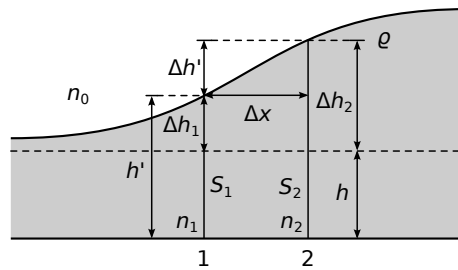


Fig. 2.14. Scheme of light passing through a transparent object. Interferency in shearing interferometry is composed of three effects: change of object thickness  $\Delta h$  with position, change of refractive index  $\Delta n$  induced by stress intensity  $S$ , deformation of the object planarity.

can be designed. In our laboratory, unlike using of various beamsplitting elements, a holographic variant of the shearing interferometry has been proposed. Two independent exposures are spaced in time and the wavefront shift is entered by mechanical displacement of model or alternatively by optical shifting of wavefront, see Fig 2.13. The recorded double exposure hologram provides the overlapping wavefronts interferency at the reconstruction. The main drawback of the classic interferometry namely the necessity of the very precise elements in optical setup with wide open viewing fields and the ideal planparallelity of the models can thus be avoided.

The basic idea of the differential (shearing) interferometry is comparison of phase between two neighbouring points of transparent planar model or the points on specularly reflected surface. The shift of the model between both of the exposures is realized by mechanical removal  $\Delta x$  from position 1 to position 2. In Fig. 2.14 the light rays passing through the transparent object are schematically drawn. The object is assumed to be uniformly illuminated by a plane wave. Let an amplitude behind the transparency at a reference plane  $\rho$  is as known

$$a_1(x, y) = a_1 \exp [ikl(x, y)] \quad (2.18)$$

in position 1, and

$$a_2(x, y) = a_2 \exp[ikl(x + \Delta x, y)] \quad (2.19)$$

in position 2. In these expressions  $l(x, y)$  and  $l(x + \Delta x, y)$  are the optical paths in points 1 and 2, respectively, and  $\Delta x$  is the displacement between both of the rays. In the case of aligning both the rays by shifting of wavefronts the interference is created and thus the intensity distribution is following

$$I(x, y) = 2a^2 \left[ 1 + \cos k(l(x + \Delta x, y) - l(x, y)) \right], \quad (2.20)$$

where  $a_1 = a_2 = a$ . For interference maxima applies

$$\frac{2\pi}{\lambda} [f(x + \Delta x, y) - f(x, y)] = 2\pi N, \quad (2.21)$$

where  $N = 0, \pm 1, \pm 2 \dots$  is the fringe order. The Eq. (2.21) is a common expression for interference fringes interpretation in shearing interferometry.

Next, let us next consider the optical path difference for planar transparent model in a plane stress state. For phase in positions 1 and 2 is

$$l(x, y) = (n + \Delta n_1)(h + \Delta h_1) + n_0 \Delta h' \quad (2.22)$$

or

$$l(x + \Delta x, y) = (n + \Delta n_2)(h + \Delta h_2), \quad (2.23)$$

respectively. In the expressions  $h$  is the initial model thickness,  $\Delta h_1$  is the change of this thickness originated by load in position 1 and likewise  $\Delta h_2$  in position 2,  $n$  is the refractive index of the unloaded transparent material,  $\Delta n_1, \Delta n_2$  are the changes due to loading. Assuming as previously, the validity of Maxwell-Neumann law for optically isotropic material, the refractive indices changes  $\Delta n_1$  and  $\Delta n_2$  induced by load are related as Eq. 2.4. Then for differences in both the points 1 and 2 there is the same linear relationship

$$\Delta n_2 - \Delta n_1 = C_0(S_2 - S_1) = C_0 \Delta S, \quad (2.24)$$

where  $S_1, S_2$  are the sums of principal stresses at corresponding points and  $\Delta S$  is their difference. In plane stress the change of planar model thickness is described by Eq. 1.51, then also

$$\Delta h' = \Delta h_2 - \Delta h_1 = -\frac{\nu h}{E} \Delta S. \quad (2.25)$$

By subtraction the Eq. (2.22) and Eq. (2.23) we have

$$l(x + \Delta x, y) - l(x, y) = h(\Delta n_2 - \Delta n_1) + (n - 1)\Delta h', \quad (2.26)$$

where the small values of  $\Delta n_1 \Delta h_1, \Delta n_2 \Delta h_2$  have been dropped and the refractive index  $n_0$  has been assumed to be 1 as it is refractive index of ambient air. Substituting Eq. (2.24) and Eq. (2.25) into Eq. (2.26) and taking into account condition of interference maxima Eq. (2.21), the basic expression for fringes interpretation is obtained after simple rearrangement of the difference of principal stresses sums in two neighbouring points

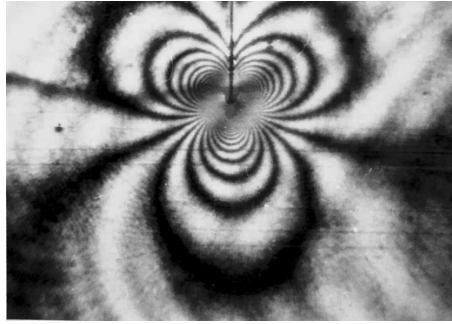


Fig. 2.15. Butterfly-like fringes present first derivatives of sum of principal stresses around loaded crack tip in PMMA beam.

$$\Delta S = c_h \frac{N}{h}; \quad c_h = \frac{\lambda}{C_0 - (\nu/E)(n-1)}, \quad (2.27)$$

where  $c_h$  is the fringe value, the same as in Eq. (2.7) for isopachics fringes. It can be determined experimentally similarly applying calibration on the bending beam.

When the value of the wavefront shear is chosen sufficiently small then the approximation of infinitesimally small difference can be applied

$$\frac{\partial S}{\partial x} = \frac{\Delta S}{\Delta x} \quad (2.28)$$

or after the substitution into Eq. (2.27) we get

$$\frac{\partial S}{\partial x} = \frac{c_h N}{\Delta x h}. \quad (2.29)$$

By analogy for the shift of the wavefronts in the direction of coordinate axis  $y$

$$\frac{\partial S}{\partial y} = \frac{c_h N}{\Delta y h}. \quad (2.30)$$

These simple formulae show the immediate coupling to the fringes of isopachics, in the planar mechanical elements, the fringes can be interpreted as contours of derivatives (slopes) of the sums of principal stresses. In Fig 2.15 there is an example of observed contours of derivatives around the loaded crack tip in PMMA beam. Their interesting property is the opportunity to adequately control the measurement sensitivity by a proper adjusting of the relative shift of both the wavefronts. In mechanics it is often encountered because of the wide range of magnitudes of deformation that may occur in experiments. As we have seen from Eq. (2.29) and Eq. (2.30) for fringes emerging the next rule is evident – the larger the shift the higher the sensitivity. However, it is necessary to note that the range of degree of control is fairly limited. It becomes relevant particularly when we are dealing with not very precipitous thickness variations or slopes, when the density of fringe pattern is small and the larger difference of wavefronts positions has to be predetermined. On the other hand, it leads to greater uncertainty, and then we have poorly defined positions of points in object coordinate system.

Another limitation of the shearing interferometer is its working principle where the double wavefront is compared by its own. The records of both the first and the second exposures bear information only on true thickness of object which as a rule in mechanical experiments is not perfectly planparallel and some kind of deformation exists. In mechanics problems for the most part, the slopes contours of deformation formed by load are dominant and some distortions due to nonparallel model are visible at once. Particularly, when dealing with singularity problems, this effect can be intentioned as a second-rare. Generally speaking, the method involves very simple holographic setup, when compared to other interferometric techniques, it is relatively insensitive to vibrations. Insignificant sensitivity of the shearing principle to rigid body motions, especially in experiments where the mechanical loads are applied, cannot be ignored, too.

The case when the information wavefront is reflected off the mirror-like surface the path difference is described simply as

$$l(x + \Delta x, y) - l(x, y) = 2(\Delta h_2 - \Delta h_1), \quad (2.31)$$

where the factor of two in front of the bracket means double passing of the light rays to the surface and back. Plane stress condition of loading leads to the next expressions for emergent interference fringes

$$\begin{aligned} \frac{\partial S}{\partial x} &= -\frac{\lambda E}{\nu \Delta x} \frac{N}{h}, \\ \frac{\partial S}{\partial y} &= -\frac{\lambda E}{\nu \Delta y} \frac{N}{h}. \end{aligned} \quad (2.32)$$

## 2.4 Holographic interferometry and photoelasticimetry

The material contribution to the fringe value can be determined also by an arrangement of the experiment not for passing the light through the transparent model but with reflection on one side wall of the beam. This is the case, where no contribution of optical fringe value  $C_0$  is observed and the fringe value  $c_h$  can then be obtained by simple calculation from the known material parameters  $E$  and  $\nu$  of the PMMA Acrylon

$$c_h = \frac{\lambda}{(\nu/E)(n_0 - 1)}, \quad (2.33)$$

where for Acrylon  $E = 3.12 \text{ GPa}$ ,  $\nu = 0.286$  [10] refractive index at the conditions of room temperature is  $n_0 = 1.497$ . Unfortunately, the fringe value calculated by such a way is not always in coincidence with the “material” fringe value obtained experimentally which is more reliable. This fact is often ignored and the influence of  $C_0$  on the interference optical path is considered as unimportant.

The measurement as we have proposed for optical constant  $c_0$  determination seems to be much more realistic. The transparent model is immersed in a liquid in a special cuvette (Fig. 2.16). The defined load deforms the beam and the inside deformation of the transparent material induces a small but in interferometry significant change of refractive index according to linear relationship of Eq. (2.4). Considering negligible difference between the refractive index of immersion liquid (e.g. glycerol) and the transparent model material, in the optical scheme with both sides of

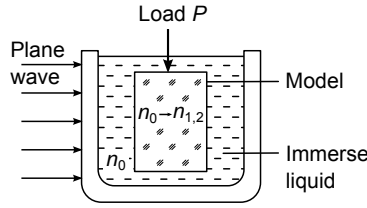


Fig. 2.16. Passing of the information wave through the transparency in immersion liquid.

beam in immersion liquid, the transversal change of the model thickness has no effect on the total path difference. For that reason, the interference fringes are created only due to stress induced changes of refractive index. As an example, the calibrating experiment of the Acrylon material gave the fringe value  $c_h = \lambda/C_0 = 22.4 \times 10^3 \text{ N m}^{-1}$  at wavelength of  $\lambda = 633 \text{ nm}$ , which can be assumed as a constant for transparent material.

The concept of measurement of the transparent planar model placed in the immersion liquid can be successfully put to use also in the case when we are dealing with comparatively thick model, when the state of stress is better described by elasticity equations as a plane strain. Generally speaking, plain strain conditions better represent also the state of stress near the free edges at the contour of the planar models.

In the 19<sup>th</sup> century Maxwell discovered that for a linearly elastic material, the changes in the indices of refraction are linearly proportional to the principal stresses and refractive index ellipsoid is considered coaxial to the stress or strain ellipsoid. For the general three dimensional case, the refractive index changes can be written as

$$\begin{aligned} n_1 &= n_0 + C_1\sigma_1 + C_2(\sigma_2 + \sigma_3), \\ n_2 &= n_0 + C_1\sigma_2 + C_2(\sigma_3 + \sigma_1), \\ n_3 &= n_0 + C_1\sigma_3 + C_2(\sigma_1 + \sigma_2), \end{aligned} \quad (2.34)$$

where the  $C$  terms represent the stress optic coefficients and the  $\sigma$  terms represent the principal stresses, along the respective axes. The term  $n_0$  is the index of refraction of the unstressed material. As seen, there is variation of refractive index as linear functions of the stress along directions of principal stresses and the sums of stresses in the perpendicular directions. In particular, for plane stress conditions  $\sigma_3 = 0$  and the system of Eq. (2.34) is simplified

$$\begin{aligned} \Delta n_1 &= C_1 \left( \sigma_1 + \frac{C_2}{C_1} \sigma_2 \right), \\ \Delta n_2 &= C_1 \left( \sigma_2 + \frac{C_2}{C_1} \sigma_1 \right), \end{aligned} \quad (2.35)$$

where  $\Delta n_1$  and  $\Delta n_2$  are the changes of refractive index in the directions of the refractive ellipsoid axes. Taking into account optically isotropic material the ellipsoid is transformed into sphere and the stress optic coefficients  $C_1 = C_2 = C_0$ , which leads to the Eq. (2.4),

$$\Delta n = \frac{1}{2}(C_1 + C_2)(\sigma_1 + \sigma_2). \quad (2.36)$$

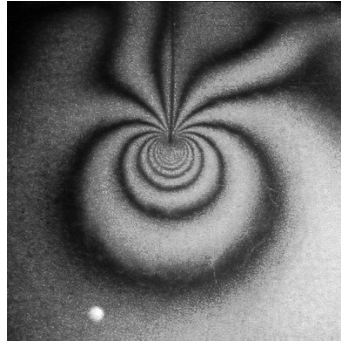


Fig. 2.17. Isopachics on PMMA beam in immersion liquid.

In the case of plane strain conditions no transversal deformation of the planar model is present i.e.  $\varepsilon_z = 0$  and consequently, for principal stress component  $\sigma_3$  transversal to the plane of planar model we have

$$\sigma_3 = \nu(\sigma_1 + \sigma_2). \quad (2.37)$$

After substitution of Eq. (2.37) into the relations of Eq. (2.34) and following adaptation in the case of isotropic material ( $C_1 = C_2 = C_0$ ) we can write the expressions for the value of sum of principal stresses

$$\Delta n = C_0(1 + \nu)(\sigma_1 + \sigma_2). \quad (2.38)$$

Fig. 2.17 illustrates the isopachic fringes around the crack tip recorded by double-exposure hologram. The phase change of the interference effect has originated from change of refractive index of the PMMA transparent material.

All the experimental approaches mentioned above are based on the basic elasticity equations for plane stress/strain in planar models. As a matter of fact the interferometry on transparent planar models can provide information only about the invariant of sum of principal stresses as it is described by Eq. (2.36) or by Eq. (2.38). However, in mechanics also the distribution of the individual principal stress components often has to be important.

Photoelasticity based on temporary artificial birefringence appearing in optically isotropic body forced by an external loading, belongs to the widely used methods in experimental stress and deformation analysis. The first authors dealing with holographic photoelasticity interpreted the interference pattern as a superposition of independent sets of isochromatics – lines of equal differences – and isopachics – lines of equal principal tensions sums [12, 13]. It was turned out, though, that such a simplistic understanding is not correct and the structure of interference pattern is much more complex [14, 15]. Further development of the method was focused on isopachics and isochromatics differentiation aiming to obtain both of them simultaneously but independently. Several techniques were proposed by introducing additional optical elements such as rotator [16], depolarisation of information wavefront [17], etc. However, technical difficulties in practical realisation hamper their wider use to solve specific tasks.

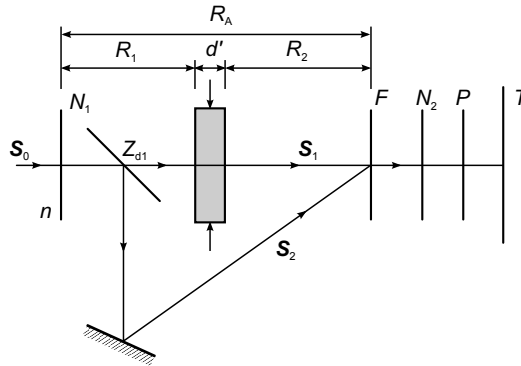


Fig. 2.18. Scheme of holographic polariscope.

### 2.4.1 Polarisation holography

In polarisation holography the Jones formalism is a useful tool to describe the state of light polarisation. The Jones vector

$$\mathbf{S} = \begin{pmatrix} S_x \\ S_y \end{pmatrix}, \quad (2.39)$$

where  $S_x$  and  $S_y$  are the components of the vector of light in the directions of axes  $x$  and  $y$ , is a compact notation of complex amplitude of monochromatic planar light wave. Influence of optical element on impinging polarized wave  $\mathbf{S}$  is characterized by the Jones matrix

$$\mathbf{J} = \begin{pmatrix} j_{11} & j_{12} \\ j_{21} & j_{22} \end{pmatrix}. \quad (2.40)$$

The vector  $\mathbf{S}'$  of the resulting light is the product of the Jones matrix and vector of initial field

$$\mathbf{S}' = \mathbf{J} \cdot \mathbf{S}. \quad (2.41)$$

The light wave intensity is expressed as

$$I = \mathbf{S}^+ \cdot \mathbf{S} = S_x^* S_x + S_y^* S_y, \quad (2.42)$$

where  $\mathbf{S}^+$  means conjugate transpose, and a star denotes complex conjugate.

Let us consider the holography interference polariscope scheme as in Fig. 2.18.  $N_1$  is an element providing appropriate polarization state of the reference wave as well as the wave illuminating object  $M$ . Usually it is linear or circular polarizer, its properties can be written using the Jones matrix  $\mathbf{J}_{N_1}$ . Suppose to have linearly polarized monochromatic wave  $\mathbf{S}_0$  with wavelength  $\lambda$  and zero initial phase in front of  $N_1$ . The Jones vector of the wave is

$$\mathbf{S}_0 = 2a \begin{pmatrix} 1 \\ 0 \end{pmatrix}, \quad (2.43)$$

where  $2a$  is the scalar amplitude of the wave. Let  $N_1$  be quarter-wave plate with azimuth  $45^\circ$ , then

$$\mathbf{J}_{N_1} = \frac{1}{\sqrt{2}} \begin{pmatrix} 1 & i \\ i & 1 \end{pmatrix}. \quad (2.44)$$

Light wave after passing  $N_1$

$$\mathbf{S}_{N_1} = \mathbf{J}_{N_1} \cdot \mathbf{S}_0 = \frac{2a}{\sqrt{2}} \begin{pmatrix} 1 \\ i \end{pmatrix} \quad (2.45)$$

is split on amplitude splitter  $Z_{d1}$  into two spatially separated circularly polarized waves with equal scalar amplitude:

1. Reference wave  $\mathbf{S}_2$  propagating to the plane of record  $F$

$$\mathbf{S}_2 = B_2 \begin{pmatrix} 1 \\ i \end{pmatrix}, \quad B_2 = \frac{a}{\sqrt{2}} \exp(ikn_0R_B), \quad (2.46)$$

where  $n_0$  is the index of refraction of surrounding environment,  $n_0R_B$  is the optical path,  $k = 2\pi/\lambda$  is the wavenumber;

2. The wave illuminating an object

$$\mathbf{S}'_M = \frac{a}{\sqrt{2}} \exp(ikn_0R_1) \begin{pmatrix} 1 \\ i \end{pmatrix}. \quad (2.47)$$

Optical properties of the object  $M$  in planar stress state can be characterized by the Jones matrix

$$\mathbf{J}_M = \exp(i\bar{\delta}) \begin{pmatrix} J_{11} & J_{12} \\ J_{21} & J_{22} \end{pmatrix}, \quad (2.48)$$

$$J_{11} = i \cos 2\varphi \sin \delta + \cos \delta,$$

$$J_{12} = J_{21} = i \sin 2\varphi \sin \delta,$$

$$J_{22} = -i \cos 2\varphi \sin \delta + \cos \delta,$$

where

$$\delta = k \frac{n_1 - n_2}{2} h', \quad \bar{\delta} = k \frac{n_1 + n_2}{2} h' \quad (2.49)$$

$n_1$  and  $n_2$  are the principal indices of refraction of anisotropical object with the thickness  $h'$ ,  $\varphi$  is the direction of the principal index  $n_1$ . Based on Maxwell-Neumann's law for the planar stress state

$$n_1 - n = C_1\sigma_1 + C_2\sigma_2, \quad n_2 - n = C_1\sigma_2 - C_2\sigma_1, \quad (2.50)$$

we have

$$\delta = k \frac{C(\sigma_1 - \sigma_2)}{2} h', \quad \bar{\delta} = k \left[ \frac{D(\sigma_1 + \sigma_2)}{2} h' + nh' \right], \quad (2.51)$$

$C_1, C_2, C = C_1 - C_2, D = C_1 + C_2$  are the optical constants,  $n$  is the index of refraction of the not driven (optically isotropic) object,  $\sigma_1, \sigma_2$  are principal stresses,  $\phi$  is the isoclines parameter.

The wave in the record plane  $F$ :

$$\begin{aligned} \mathbf{S}_1 &= B_1 \begin{pmatrix} J_1^F \\ J_2^F \end{pmatrix}, \quad B_1 = \frac{a}{\sqrt{2}} \exp[ikn_0(R_A - h')] \exp(i\delta), \\ J_1^F &= J_{11} + iJ_{12} = i \exp(i2\varphi) \sin \delta + \cos \delta, \\ J_2^F &= j_{21} + iJ_{22} = \exp(i2\varphi) \sin \delta + i \cos \delta. \end{aligned} \quad (2.52)$$

### Holographic record of isochromatics

In the considered layout, the superposition of the circularly polarized reference wave  $\mathbf{S}_2$  and elliptically polarized information wave  $\mathbf{S}_2$  is registered in on the recording medium:

$$\mathbf{S} = \mathbf{S}_1 + \mathbf{S}_2 = \begin{pmatrix} B_1 J_1^F + B_2 \\ B_1 J_2^F + iB_2 \end{pmatrix}. \quad (2.53)$$

Using reconstruction wave  $\mathbf{S}_3$

$$\mathbf{S}_3 = B_3 \begin{pmatrix} 1 \\ i \end{pmatrix}, \quad B_3 = \frac{\bar{a}}{\sqrt{2}} \exp(ikn_0 R_B), \quad (2.54)$$

with the scalar amplitude  $\bar{a}$ , the wave  $\mathbf{S}_v$  is restored according to the basic equations of holographic imaging

$$\mathbf{S}_v = \frac{a^2 \bar{a}}{\sqrt{2}} \exp[ikn_0(R_A - h')] \exp(i\delta) \cos \delta \begin{pmatrix} 1 \\ i \end{pmatrix}, \quad (2.55)$$

which creates virtual image with the intensity

$$I_v = a^4 \bar{a}^2 \cos^2 \delta \quad (2.56)$$

carrying information about the relative birefringence distribution or the function of differences of principal stresses in the object respectively. The intensity minimas ( $\cos^2 \delta = 0$ ), i.e. isoclines of the function

$$\sigma_1 - \sigma_2 = \frac{\lambda}{Ch'} m, \quad m = \frac{1}{2}, \frac{3}{2}, \frac{5}{2}, \dots \quad (2.57)$$

create half-order isochromatics, the layout corresponds to the scheme of the classical circular polariscope with bright view-field.

### Double exposure record

In unloaded body of thickness  $h$ ,  $n_1 = n_2 = n$  and the light field in the plane  $F$  is created by waves

$$\mathbf{S}_1^0 = B_1^0 \begin{pmatrix} 1 \\ i \end{pmatrix}, \quad B_1^0 = \frac{a_0}{\sqrt{2}} \exp(ik[n_0 R_A + (n - n_0)h]), \quad (2.58)$$

$$\mathbf{S}_2^0 = B_2^0 \begin{pmatrix} 1 \\ i \end{pmatrix}, \quad B_2^0 = \frac{a_0}{\sqrt{2}} \exp(ikn_0 R_B). \quad (2.59)$$

Light field  $\mathbf{S}^0 = \mathbf{S}_1^0 + \mathbf{S}_2^0$  is recorded and  $\mathbf{S}_v^0$  is then restored in reconstruction process:

$$\mathbf{S}_v^0 = \frac{a_0^2 \bar{a}}{\sqrt{2}} \exp(ik[n_0 R_A + (n - n_0)h]) \begin{pmatrix} 1 \\ i \end{pmatrix} \quad (2.60)$$

with the virtual image intensity  $I_v^0 = a_0^4 \bar{a}^2$  without any information about the object.

Then the information wave  $\mathbf{S}_1$ , Eq. (2.52), from the object with loading superponed on the reference  $\mathbf{S}_2$ , Eq. (2.46), is recorded using the unchanged optical setup. The reconstructed wave  $\mathbf{S} = \mathbf{S}_v^0 + \mathbf{S}_v$  of such double exposed record has the intensity

$$I = a_0^4 \bar{a}^2 (1 + \eta^2 \cos^2 \delta + 2\eta \cos \bar{\delta} \cos \delta), \quad (2.61)$$

where the following substitution are introduced

$$\begin{aligned} \eta &= (a/a_0)^2, \\ \bar{\delta} &= k[n_0 d' + (n - n_0)h] - \delta; \end{aligned} \quad (2.62)$$

expression for  $\bar{\delta}$  can be modified with respect to Eq. (2.49) and Hooke's law for transverse deformation of planar objects to the form

$$\bar{\delta} = kh \left[ \frac{\nu}{E} \frac{D}{2} (\sigma_1 + \sigma_2)^2 - \left( \frac{D}{2} - \frac{\nu}{E} (n - n_0) \right) (\sigma_1 + \sigma_2) \right], \quad (2.63)$$

wherein the first term is usually neglected [13] and  $\bar{\delta}$  is considered as a sum of the principal stresses

$$\bar{\delta} = \frac{\pi h}{\lambda} \left[ \frac{2\nu}{E} (n - n_0) - D \right] (\sigma_1 + \sigma_2). \quad (2.64)$$

The minima of  $\cos \bar{\delta}$  for  $\bar{\delta} = s\pi$  determines isofringes of the orders of  $s$

$$\begin{aligned} \sigma_1 + \sigma_2 &= C_s s, \\ C_s &= \frac{\lambda}{h} \left[ \frac{2\nu}{E} (n - n_0) - D \right]^{-1}, \\ s &= \pm \frac{1}{2}, \pm \frac{3}{2}, \pm \frac{5}{2}, \dots \end{aligned} \quad (2.65)$$

### Real time analysis

Suppose the information wave recorded at the first exposure came from the unloaded object. The polarization state of the reconstructed wave  $\mathbf{S}_v^0$ , Eq. (2.60), is determined by polarization of the reconstructing wave  $\mathbf{S}_3$ . The wavefront  $\mathbf{S}_1$  from the object under load is incident on this hologram placed in its original position. Given that only parallel components of light vectors can interfere, the intensity of the final field  $\mathbf{S}_v^0 + \mathbf{S}_1$  is

$$I = a_0^4 \bar{a}^2 (1 + \xi^2 + 2\xi \cos \bar{\delta} \cos \delta), \quad \xi = \frac{a}{a_0^2 \bar{a}}. \quad (2.66)$$

Complement of the observation optical scheme by analyzer is proving to be an advantageous modification of holographic interferometric polariscope in real-time mode. In Fig. 2.18,

$N_2$  denotes a quarter-wave plate characterized by Jones matrix  $\mathbf{J}_{N_2} = \mathbf{J}_{N_1}$ .  $P$  is a polarizer transmitting the wave with oscillation parallel to  $\mathbf{S}_0$ . Then, light field behind the analyzer is

$$\mathbf{S} = \frac{1}{\sqrt{2}} \begin{pmatrix} 0 & 0 \\ i & 1 \end{pmatrix} (\mathbf{S}_v^0 + \mathbf{S}_1) \quad (2.67)$$

and the intensity

$$I = a_0^4 \bar{a}^2 (1 + \xi^2 \cos^2 \delta + 2\xi \cos \bar{\delta} \cos \delta). \quad (2.68)$$

#### 2.4.2 Interpretation of interference pattern

The basic layout of the holographic interference polariscope allows to obtain two types of interferograms. Eq. (2.61) or Eq. (2.68) and Eq. (2.66), respectively, are characterized by discontinuous nature of the superimposed networks of interference fringes. Eq. (2.66) (originally derived for the Mach-Zehnder classic interferometer [18]) in contrast to equations Eq. (2.61) and Eq. (2.68) does not contain the member  $\cos^2 \delta$ , whose influence is significant:

1. Interference fringes according to Eq. (2.61) and Eq. (2.68) interpreted as isochromates of half-number orders are always continuous lines, while interpreted as isopachics are discontinuous.
2. Using Eq. (2.66) isochromates are continuous and isopachics are discontinuous, for the ratio of spatial frequencies  $p > 1$ , on the other hand isochromates are discontinuous and isopachics are continuous for  $p < 1$ .

The interference pattern is rather a complicated function of spatial frequencies, cross-angle of superposed networks and amplitudes of light waves used in the recording and observation [14]. The useful technique in its interpretation shows to be the method of light field singularities enabling more precisely localisation of areas, on which light field intensity reaches zero values, i.e.  $I = 0$ . The condition is fulfilled, if

$$\sin \bar{\delta} = 0 \quad \text{and} \quad \alpha \cos \delta + \cos \bar{\delta} = 0 \quad (2.69)$$

( $\alpha \equiv \eta$  and  $\alpha \equiv \xi$ ), i.e. if

$$\cos \bar{\delta} = 1 \quad \text{and} \quad \cos \delta = -1/\alpha \quad (2.70)$$

or

$$\cos \bar{\delta} = -1 \quad \text{and} \quad \cos \delta = 1/\alpha. \quad (2.71)$$

The zero-intensity points lie on the isopachics of full line orders  $\bar{\delta} = s'\pi$ ,  $s' = 0, \pm 1, \pm 2, \dots$ , while

1. for the interference pattern of type Eq. (2.66) they are present only when  $\alpha = 1$  and can be found alternately at the intersections of full order isochromtas and isopachics.
2. for the pattern of type Eq. (2.61), Eq. (2.68) the singular points appear when
  - (a) for  $\alpha = 1$  in the places as in the case 1

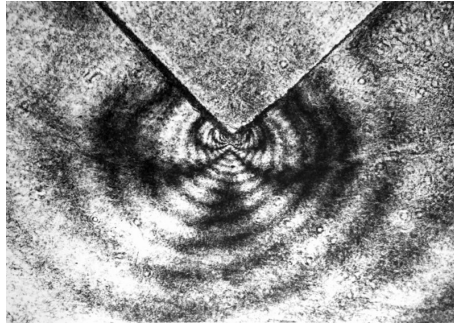


Fig. 2.19. Interference fringes of both isochromatics and isopachics obtained by double-exposure holography on a planar transparent photoelastic object [19].

- (b) for  $\alpha > 1$  doubled points  $I = 0$  in the places  $\cos \delta = \pm 1/\alpha$ , which are shifting for the rising  $\alpha$  along isopachic symmetrically towards the visible half-order isochromates.

Complex nature of intensity distribution in the interference pattern is illustrated in Fig. 2.19 for simulated model of orthogonal networks of isochromats and isopachics superposition. Also the isofringes  $I = \text{konst.}$  for different values of  $\alpha$  are plotted in the figure.

## 2.5 Visualisation of ultrasonic bending wave propagation

The ultrasonic testing of the concrete abounds in the problems and there are evidently possibilities, how the current diagnostic procedures can be improved. Complicated circumstances, which are as a rule present in the case of heterogeneous and porous materials like concrete follow from the fact, that attenuation properties restrain using of higher frequencies – usually the frequencies 150–200 kHz are considered as a limitation. Corresponding values of the ultrasonic wavelengths propagating in concrete are going on in the range  $\sim 2\text{--}20$  cm i.e. these lengths are comparable with geometrical dimensions of the specimens tested. It gives rise to problems with the sensing of waves arriving from the reflected free boundaries of the specimen and with the following separation of longitudinal and shearing wavefronts. On the other hand, the considerable dependency of the attenuation bears information about the main mechanical parameters of the concrete and its deterioration, and thus makes its evaluation possible. As it is turned out, the key factor at the precise sensing of both the wave velocity and the attenuation is the ability of transducers for right acquisition of the time dependency of mechanical vibration on the concrete surface induced by the ultrasonic wave. Piezoelectric accelerometers or simple US probes conveniently used for such a purpose take information by contact means and its transient characteristic depends on the tight fixation of the transducer on the surface.

Holographic interferometry using pulsed laser has long been applied for the visualisation of structural vibrations. The pulse width or exposure time of the appropriate lasers is usually some tens of nanoseconds, thus even the dynamic deformation of the surface stress wave propagation can be recorded by hologram without any problems with blurring. Holloway [20] and Aprahamian et al. [21] demonstrate the use of the method for observation of a mechanical excitement

propagation in plates.

Using opportunities of the pulsed ruby laser the flexural ultrasonic waves propagation has been studied in the concrete plates specimens of the widths 33 mm, 55 mm and 120 mm. The diameter of the freely supported plates 650 mm, as well as the duration of the exciting impact were chosen from the condition to avoid the interference of the waves reflected from the free boundaries of plates at the moment of measurement. The diameter of the freely supported plates, as well duration of the exciting impact were chosen 650 mm and 20–30  $\mu\text{s}$ , respectively. By such a means the propagating circular bending waves create a few periods of waves on the concrete surface before their reflection from the free boundary.

The impact of projectile from the air gun the mechanical impulse excited the vibrations in ultrasonic region of frequencies. The impact speed of the lead projectile was measured photoelectrically. The dispersion of individual fires was  $\pm 5 \text{ m s}^{-1}$  at the impact speed  $150 \text{ m s}^{-1}$ . The time traces of the impact force were recorded by two sensing devices. One of them was standard piezoelectric accelerometer fixed precisely in the place of projectile impact on the opposite side of the plate. By double integrating of the electric signal from the accelerometer the time history of its displacement was deduced and consequently, the dynamic moving of concrete surface at the fixation point was evaluated.

In order to measure the dynamic impact force directly, miniature dynamometer was developed. It is based on optical diffraction principle [22], where the light of laser beam is focused onto the narrow slit in the centre of elliptically shaped steel ring (the outer diameter  $\varnothing = 10 \text{ mm}$ ). The light after passing through the slit is diffracted and collected onto the effective area of photodiode. Deformation of the steel ring owing to acting force changes the width of the slit and subsequently the amount of the light passed.

The requirement to develop the dynamic force transducer with higher value of its natural frequency is followed by the necessity of appropriate calibration in absolute values of the force. The most simple way how to do the calibration seems to be static calibration force vs. output electric signal. However, in such a case the transducer cannot be used reliably for measurement of force impulses with frequencies comparable with that of resonant (natural) frequency of transducer due to the dynamic nonlinear effects at this region. Despite its miniature dimensions the natural frequency of the sensor was about 100 kHz, that is why we have developed the dynamic method of calibration based on Newton's second law. Since force duration is an impulse, we write the known relationship

$$mv = - \int_0^T P dt, \quad (2.72)$$

where  $m$  and  $v$  are the mass and the impact velocity of the projectile, respectively, and  $P$  is acting dynamic force during the time  $T$ . As it follows from Eq. (2.72) to determine the absolute values of time varying dynamic force also its time history is needed. This was recorded by oscilloscope and proved to be nearly half-sine shaped (see Fig. 2.20).

Half-sine force peak as it is assumed by the Hertz's theory of impact was affirmed, in spite of the fact, that the projectile made of lead was deformed at the impact plastically

$$P(t) = \begin{cases} P_{\max} \sin(\pi t/T), & 0 \leq t \leq T, \\ 0, & T \leq t. \end{cases} \quad (2.73)$$

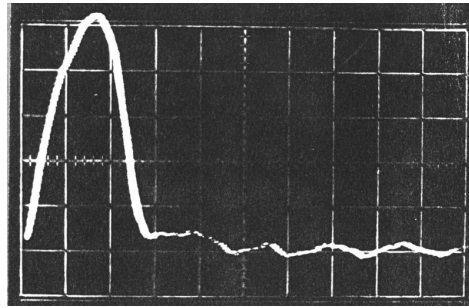


Fig. 2.20. Oscilloscopic trace of the dynamic force generated by projectile impact on the plate surface. Time base  $10 \mu\text{s}/\text{div}$ , dynamic force scale  $293 \text{ N}/\text{div}$ .

The maximum magnitude level of the force  $P_{\text{max}}$  for the half-sine shape mentioned, can be calculated by expression

$$P_{\text{max}} = \frac{\pi m v}{2T}. \quad (2.74)$$

Such a dynamic calibration of the transducer is sufficiently precise, however, due to the thermal effect the part of kinetic energy can influence the results. To remove this factor, this thermal amount of energy was experimentally determined by the measurement of energy transferred to heavy weight pendulum oscillations.

The frequency content of the energy applied to the structure is a function of the stiffness of the contacting surfaces, the mass of the impacted projectile and the velocity of its impact. The stiffness of the contacting surfaces and, to some measure, the shape of the projectile affects the time history of the force pulse, which in turn determines the frequency content of exciting vibrations. As it is not feasible to change the stiffness of the specimen, the frequency content may be controlled by varying the impact velocity and/or by a material of projectile. The actual frequency content of the exciting pulses was assessed by Fourier spectral analysis of the time traces recorded. The time width of such mechanical shocks was about  $20\text{--}25 \mu\text{s}$  (see Fig. 2.20). This leads to the exciting of the ultrasonic frequencies up to  $100 \text{ kHz}$ , where the spectrum comes near to zero. A disadvantage to note here is that the force spectrum of an impact excitation cannot be band-limited at lower frequencies, which are highly expressive. Nevertheless, the broad-band spectrum includes all the frequency components (up to  $100 \text{ kHz}$ ), so that the spectral dependencies, such as wavelengths and dispersions, can be acquired.

Double exposure holograms were recorded by means of two monopulses of ruby laser at the wavelength of  $694 \text{ nm}$ . At the first exposure the hologram of concrete plate surface before deformation was recorded and then the second exposure after the time interval  $5 \mu\text{s}$  to  $120 \mu\text{s}$  after beginning of the impact the second hologram was recorded. The different double-exposure holograms were recorded for variety of time moments after starting of impact. Interferometrical pattern recorded on holograms represents different position of the running wavefront from the impact point. Geometry of optical scheme was arranged with incident angle of illuminating light nearly perpendicular to the object surface observed and the object was also observed

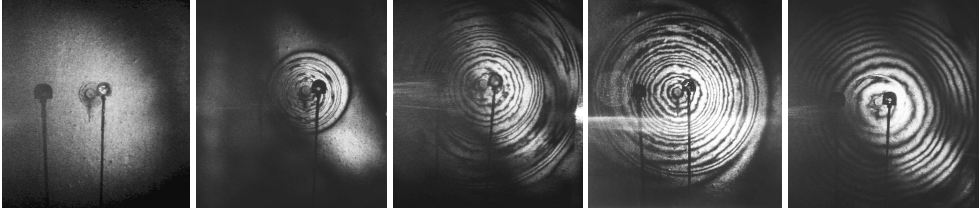


Fig. 2.21. Sequence of holographic interferograms of the surface dynamic deformation on the concrete surface – 5  $\mu$ s after load beginning, 25  $\mu$ s, 50  $\mu$ s, 65  $\mu$ s and 125  $\mu$ s.

through hologram nearly perpendicularly to the plate surface. Then, the interference fringes can be interpreted as curves of equal amplitudes of plate deflections

$$w = \frac{N\lambda}{2 \cos \varphi}, \quad (2.75)$$

where  $N$  is interference order,  $\lambda$  is wavelength and  $\varphi$  is angle of incidence or observation. At this layout the fringe value used for the evaluation of interferograms was  $3.87 \times 10^{-4}$  mm.

In order to synchronize the time of second exposure exactly at the moment of instantaneous wavefront position arbitrarily chosen, the simple electro-mechanical sensor was developed. Two pieces of aluminium foil were placed one to another with a narrow interspace and they were connected in electronic circuit. At the moment of the foils penetrating by flying projectile the short connection created basic triggering impulse. The synchronizing of the laser flash is complicated by the fact, the moment of arriving of the input signal to the laser controller unit to pump the laser ruby crystal and to break the passive Q-switch. Therefore, the precise positioning (in our case about 100 mm) of the sensor in front of the concrete surface was carried out tentatively. By small shifting of the braking sensor position this distance was corrected and the moment of instantaneous dynamic deformation of recording at the running wavefront was chosen for each of the case. The time interval between the starting of impact loading and the moment of the second laser light pulse was measured comparing the time position of signal transmitting from piezoelectric transducer fixed in the centre of the back side of concrete plate and from the photodiode signal of laser light flash.

Holographic interferometry can give the large field view on the instantaneous dynamic deformation of the surface. However, the detailed knowledge of the time dependency of this deformation is of fundamental importance. On that account, we have used also the piezoelectric transducer to confront its data with that obtained holographically.

To illustrate the possibilities of holographic interferometry, the time sequence of the holographic records of flexural wave propagation on the concrete surface is shown in Fig. 2.21. These were taken at different time moments after starting of loading. Note that the time history of dynamic deformation was folded from different events of the loading series.

In order to compare the real situation with that of theoretically predicted we have calculated the instantaneous surface deformation state for several time moments. These calculations were based on the analytical expressions obtained in [23]. The expressions take into account linear

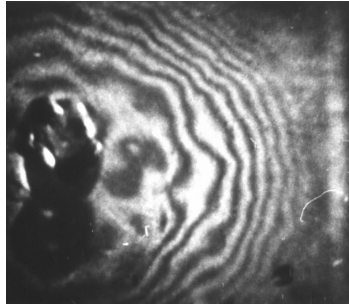


Fig. 2.22. Distortions of ultrasonic wavefront propagating on a plate surface.

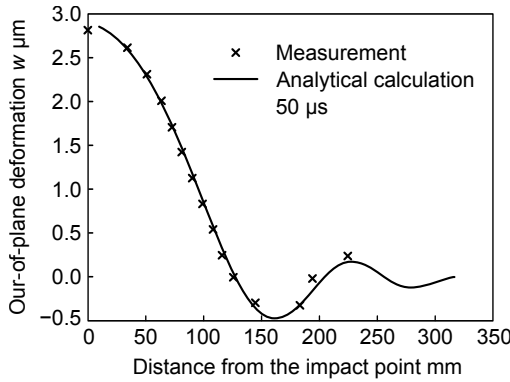


Fig. 2.23. Comparison of analytically vs. experimentally obtained instantaneous deformation of the concrete surface around the point of impact.

behaviour of the concrete as a homogeneous material and also approximation of dynamic loading pulse is in agreement with the Hertzian theory.

One of the chosen time points of instantaneous dynamic deformation is plotted in Fig 2.22.

The solid curve is the analytical prediction of surface deflections and crosses indicates the deflection values read as interference orders from holographic interferogram. As seen, there is a good coincidence of calculated surface shapes with that observed by holography. Concerning the quantitative values of deflections, we have to note, that the dynamic values of Young’s modulus used in calculations were determined from ultrasonic measurements of concrete material, and also the real values of the loading force at the impact were obtained from the data from diffraction dynamometer.

Besides the deformation calculations using the simplified analytical expressions the numerical computation on the basis of Kirchhoff’s theory of plates were carried out, too. One result of such a calculation of the dynamic instantaneous surface shape is presented in graph of Fig. 2.23. Here the circular plate with thickness of 55 mm was computed at the time moment of 30  $\mu\text{s}$  after

the initiation of impulse loading. From the graph there is a clearly visible dispersion phenomenon due to relatively small thickness of the plate in comparison with stress wave wavelengths induced by mechanical impact. Theoretically, the infinite frequencies have to propagate with the infinite velocities of these frequencies. However in real situation, the highest frequencies (in the case more than 100 kHz) are quickly attenuated, that is why these frequencies are not visible. Nevertheless, the edge of ultrasonic wavefront from holographic records is clearly contoured. Well observable are also distortions of propagating wavefront caused by subsurface inhomogeneities of the heterogeneous concrete material (see Fig. 2.22).

## 2.6 Interferometrical evaluation of the temperature distribution inside transparency

Dealing with the clearly transparent objects through which the light is passing, the classical laser based wide field interferometry can often be effective. Besides the standard testing of optical components, namely the transparent elements are proper examples where these approaches claim attention. In transparency, not only the shape or deformation changes are often relevant, but also the refractive index variations or refractive index whole field distribution are interesting. As known, the refractive index of liquids, gases but also transparent solids show the temperature dependency to such an extent that the temperature changes in units of degrees, or even part of a degree can be successfully detectable interferometrically through path difference detection. Temperature derivative of the index of refraction is a characteristic value of the material, hence, after the appropriate calibration, an interferometrical mapping can provide also temperature field distribution inside the object even on quantitative basis. Besides this, the refractive index dependency is conveniently used for detection of pressure induced variations of the refractive index field. Mostly, such a measurement does not need a large field of observation, then the interferometrical scheme can be assembled by small sized optical elements, which can be precised enough and they are not too expensive. Despite the specific problem of the transparent object shape inaccuracy, when rather a dense pattern of interference fringes is observed in initial state, can be overcome as well. Then the temperature field in solid transparency is evaluated by mutual comparison of the interference patterns before and after the heating of the model.

Such an experimental interferometrical measurement has been performed to evaluate temperature distribution inside the second harmonic generation (SHG) KTP crystal. As it was approved previously, the temperature change induced by multimode exciting beam of  $\lambda = 1064 \text{ nm}$  is nonmeasurable when no second harmonic generation occurs. To overcome the current problem as well as lack of pumping, Raman shifted 1178 nm Yt: fiber laser and to have the possibility to elaborate the detection and evaluation procedure, heating of the SHG crystal by CW argon laser was used. The argon laser used emits basic spectral lines at  $\lambda = 514 \text{ nm}$  and  $488 \text{ nm}$  with the output power up to 6 W. The absorption coefficients of KTP crystal material at this spectral range is approximately one order higher compared to the absorption at  $\lambda = 1064 \text{ nm}$ . Moreover, the CW argon laser emits nearly  $\text{TEM}_{00}$  mode, thus the simulated *exciting* beam can be concentrated inside crystal into the focus with the waist of 20–40  $\mu\text{m}$  in diameter. Then, the conditions of crystal illumination and consequently the heat generation are presumably not so far from those at second harmonic generation.

The crucial problem of the temperature distribution assessment is the limited sensitivity of interferometric method. The primary value to be measured is the index of refraction but its temperature induced changes are very small, currently at parts of degree change. Another limitation

is the fact, that the whole area of the SHG crystal has to be mapped. That is why photoelectric sensing based on high resolved photodiode cannot be used and also observation by CCD has an insufficient light intensity resolution. Furthermore, when detecting the path differences much smaller than the wavelength of light, also the overall concept of interferometer setup has to be regarded. At such sensitive measurements the fluctuating ambient environmental conditions are an additional factor.

All of these factors lead to the proposal to install Fabry-Perot interferometry based optical scheme where the differential comparison of both the front and backside of the crystal are realized. In such a setup only the variations of refractive index inside crystal are detected, other circumambient influences are compensated and do not affect the resulting fringe pattern.

When a coherent beam of light is incident perpendicularly or nearly perpendicularly upon the SHG crystal sidewalls, the resulting pattern of interference between both the reflected wavefronts is created. The total field  $E$  at a point on observation screen (or CCD chip) is the sum of the two waves superimposed on each other and results in the following

$$E = E_1 + E_2 = a \left[ e^{-ikr} + e^{-ik(r+h)} \right] e^{i\omega t}. \quad (2.76)$$

In the above equation  $A$  is the nominal amplitude of the laser light,  $k$  is the wave number,  $r$  and  $(r + h)$  are the optical paths after reflection off the sidewalls,  $\omega$  is the angular frequency and  $t$  is the time. Notice that multiplying  $h$  by the wave number  $k$ , is a representative of the fringe pattern phase shift

$$\varphi = \frac{2\pi}{\lambda} h. \quad (2.77)$$

Rearranging Eq. (2.76) in terms of the phase shift results in

$$E = ae^{-i(kr-\omega t)}(1 + e^{-i\varphi}). \quad (2.78)$$

The term in parenthesis can be rewritten as  $2 \cos(\varphi/2)e^{-i\varphi/2}$  and multiplying the equation by its complex conjugate yields the intensity distribution as a function of the fringe pattern phase

$$I = |E|^2 = 4a^2 \cos^2(\varphi/2)$$

or

$$I = 2a^2(1 + \cos \varphi). \quad (2.79)$$

When the very small index of refraction variations has to be evaluated, the necessity of precise measurement of subfringe shifting of the interference pattern is vital part of evaluation. Up to day, such a data evaluation has been performed usually on subjective basis and then the error reached 1/10 to 1/20 of the width of fringe contour. In principle, it is possible to detect intensity changes with much higher sensitivity by a photodiode based photoelectric sensing. Unfortunately, such measurement is the only point-like method and mapping of whole the area of crystal will need some kind of scanning. We have tested also such an approach as described later in this section.

In the case of demand for the whole field of observation, image processing must be applied in order to compare both the interference patterns, before and after heating of the crystal by *exciting* Ar laser.

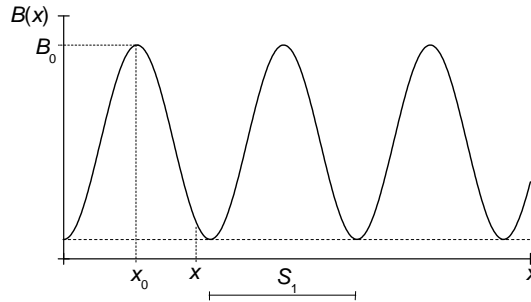


Fig. 2.24. Double-beam intensity profile of the interference fringes.

By a simple mathematical derivation based on the previous expressions, the function of intensity distribution in the field of view on plane of interference fringes localization can be written (see also Fig. 2.24)

$$I(x) = 2I_0 \left( 1 + \gamma \cos \left[ \frac{2\pi}{d_1} (x - x_0) \right] \right), \quad (2.80)$$

where  $x_0$  is the coordinate of the reference interference fringe,  $I_0$  is the intensity of one of interfering wavefronts,  $d_1$  is the width of the interference fringe, and  $\gamma$  is the constant representing fringe contrast. Eq. (2.80) describes the system of parallel interference fringes in the direction perpendicular to the fringes and can be used also to express the fringe pattern after its shifting due to the temperature index of refraction change

$$I(x') = 2I_0 \left( 1 + \gamma \cos \left[ \frac{2\pi}{d_1} (x + x' - x_0) \right] \right), \quad (2.81)$$

where  $x'$  is the shift of interference fringe.

As seen, comparison of both the equations Eq. (2.80) and Eq. (2.81) gives us the possibility to determine the path difference induced by temperature increase through the evaluation of separated fringe maxima or minima shift  $x'$ . As the change of path difference between two neighbouring fringes is equal to wavelength of light used, the non-dimensional fringe pattern shift relative to its initial position gives the searched change in path difference

$$\Delta l = \frac{x'}{d_1} \lambda. \quad (2.82)$$

Consequently, the non-dimensional fringe shift can be measured by evaluating the initial location of a fringe minimum or maximum and tracking how it moves relatively to its primary position and dividing it by the period of one fringe cycle.

Taking into account the double passing of the SHG crystal thickness

$$\Delta l = 2h_0(n - n_0) + (h - h_0)n_0, \quad (2.83)$$

where  $n_0$  is the initial index of refraction inside the crystal in the direction of light propagation,  $h_0$  is the thickness of SHG crystal,  $n$  is the index of refraction inside the crystal after its heating, and  $h$  is the thickness of the crystal after heating.

With regard to the real values of index of refraction vs. temperature and on the other hand the coefficient of thermal expansion of SHG crystal material, the second term of Eq. (2.83) can be omitted, its quantitative value is as much as one order smaller than the path difference caused by index of refraction change. Finally, using the known parameter of temperature derivative  $\partial n/\partial T$ , where  $T$  is temperature, the required value of the inside temperature increase can be determined.

In real conditions of the SHG crystal measurement both the expressions Eq. (2.80) and Eq. (2.81) have to be modified. As a rule, the prism of the crystal is ground with non-precise planparallelity of its surfaces, thus the interference fringes of initial patterns are deformed. Provided that the fringe of equi-phase points (e.g. fringe of minima or maxima) can be described by a simple function

$$y = y(x), \quad (2.84)$$

the equation of the pattern intensity distribution is as follows

$$I(x, y) = 2I_0 \left[ 1 + \gamma \cos \frac{2\pi}{d_2} \left( (x - x_0) \sin \alpha + y \sin \alpha \right) \right], \quad (2.85)$$

where  $\alpha$  is the angle between the tangent to fringe curve and  $x$  axis and  $d_2$  is the width of interference fringe in the direction perpendicular to the fringe curve at the point under consideration. Using the Eq. (2.82) also at such a pattern the path difference temperature change can be determined.

All the above mentioned expressions were derived assuming the double-beam interference conditions. However, the SHG crystal is a nearly plane-parallel plate and in fact Fabry-Perot multi-beam interference is registered in the scheme with both the front and the backside reflections. When a monochromatic light is directed normally to the transparent plate having refractive index  $n_0$  and the thickness  $h_0$ , the reflectance is given by well known Fresnel expression

$$R_F = \frac{R_1 + R_2 - 2\sqrt{R_1 R_2} \cos \varphi}{1 + R_1 R_2 - 2\sqrt{R_1 R_2} \cos \varphi}, \quad (2.86)$$

where  $R_1$  and  $R_2$  are the reflection coefficients for the front surface and the back one, and

$$\varphi = \frac{4\pi}{\lambda} n_0 h_0 \quad (2.87)$$

is the optical path difference of both the interfering beams. For such a multi-beam interference the intensity distribution of the fringe pattern is as follows

$$I(x) = I_0(x) \frac{F \sin^2 \varphi/2}{1 + F \sin^2 \varphi/2}, \quad (2.88)$$

where

$$F = \frac{4R}{(1 - R)^2}; \quad \varphi = \frac{2\pi}{\lambda} l_1 \cos \theta \quad (2.89)$$

and  $R = R_1 = R_2$  is the coefficient of reflection of the SHG crystal surfaces,  $\theta$  is the angle between direction of wavefront propagation and the normal to the surface, and

$$l_1 = 2n_0 h_0 \quad (2.90)$$

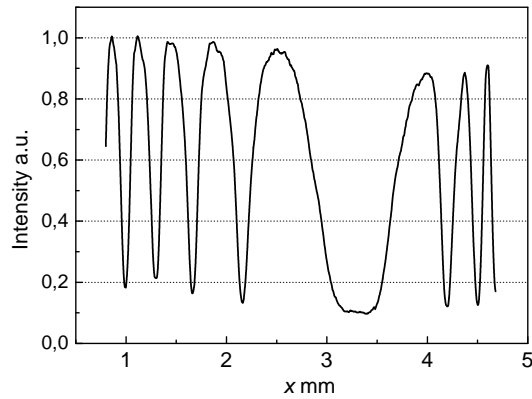


Fig. 2.25. Shape of the multi-beam interference fringes.

is the optical path.

The illustrative example of the obtained fringe pattern distribution is shown in Fig. 2.25 where the deviation of wavefront curve is visible from the pure harmonic development of Eq. (2.80). Nevertheless, the surfaces reflectance of the measured object of crystal is in the range of some percent ( $R \approx 0.05$ ), then for the small value of  $F$  the shift of the fringe pattern is nearly the same as described by Eq. (2.82).

As it follows from the results obtained (see the section below), the evaluation procedure described can be successfully applied to map the temperature distribution throughout the whole area of the SHG crystal. In practical realization the limit of ultimate sensitivity for temperature change evaluation can be given using realistic assessment for  $x'/S_1$  from  $1/20$  to  $1/40$ , or  $1/20\lambda$  to  $1/40\lambda$  (see Eq. (2.82)). With the actual temperature derivative  $\partial n/\partial T$  parameter of the KTP crystal it leads to the experimental uncertainty of temperature defining of  $\pm 0.1$  to  $\pm 1.0$  K.

In order to overcome this ultimate value, the point like measurement has to be used with the detecting of fringe pattern intensity variations by photodiode detector. Again, based on Eq. (2.79) for small intensity changes  $\Delta I \ll \lambda$  we obtain by differentiation following expression

$$\Delta I(x) = a^2 \frac{2\pi\Delta l}{\lambda} \sin \varphi. \quad (2.91)$$

From that equation the change in paths differences is written

$$\Delta l(x) = \frac{\Delta I(x)\lambda}{2\pi a^2 \sin(2\pi l/\lambda)}. \quad (2.92)$$

The expression of Eq. (2.91) indicates the best sensitivity of intensity sensing at the positions, where

$$\varphi_m = \frac{\pi}{m + 1/2}, \quad (2.93)$$

that is in the central positions between neighbouring interference maxima and minima. Therefore, the active area or slit diaphragm of the detector has to be placed at this position.

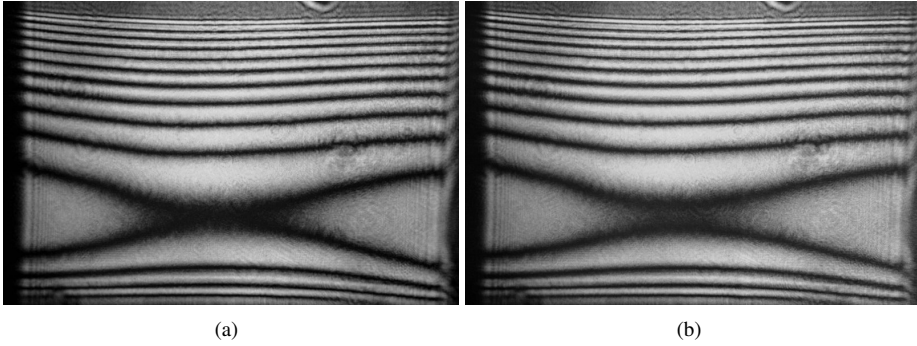


Fig. 2.26. Interference fringes of equal thickness of the KTP crystal (a) before laser heating, (b) after laser heating.

In the case of multi-beam interference starting from the Eq. (2.88) the expression for intensity variations due to small path difference changes can be derived

$$\Delta I(x) = \frac{\pi \Delta l}{\lambda} \frac{F \sin \varphi/2}{(1 + F \sin^2 \varphi/2)^2} \quad (2.94)$$

and then for change in optical paths differences

$$\Delta l(x) = \frac{\Delta I(x) \lambda (1 + F \sin^2 \varphi/2)^2}{\pi F \sin \varphi/2}. \quad (2.95)$$

Fabry-Perot interferometrical setup with the observation of interference pattern by digital camera was arranged. The sensitivity of interference pattern reading was sufficient to detect the heating of the SHG crystal induced by focused Ar laser beam at the power of 2 W and 5 W. As an illustration in Fig. 2.26 there are the interference patterns of the crystal around the focus of the Ar *exciting* beam. The figures present the initial temperature state and the heated state. The crystal is situated on the brass base with good heat removal. In Figures the brass base is in the bottom part, vertical dimension means 5 mm of the crystal width. Fig. 2.27 shows the comparison of light intensity distribution for two states of the crystal temperature – the initial and the steady state after its stabilising. The transient process of heating lasts about 60 seconds. Duration of the reversible process of the crystal cooling was approximately the same.

Next Fig. 2.28 presents the experimentally determined temperature distribution inside measured KTP crystal and its comparison with the results of numerical simulation. As it can be simply deduced, the nature of curves is the same although the quantitative values of temperature can be strongly influenced by a not very precise knowledge of the parameters  $\partial n/\partial T$  as well as by basic thermomechanical constants for numerical input data.

The interference patterns observed were also analyzed by photodiode detector. The active area of the photodiode was screened by slit diaphragm whereby the slit opening was properly oriented and positioned at the best point between neighbouring fringes. The crystal area was then mapped point by point in ten chosen positions.

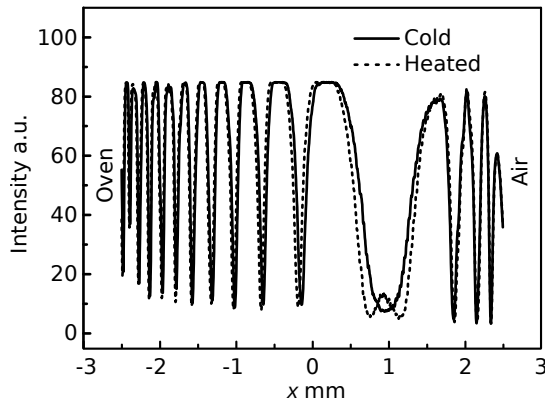


Fig. 2.27. Shifting of the light intensity interference pattern after heating the crystal.

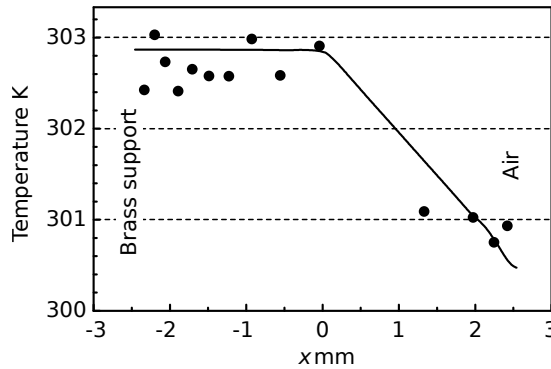


Fig. 2.28. Comparison of the experimentally obtained temperatures with the numerical simulation.

## 2.7 Membrane thickness mapping by Fizeau interferometry

The measurement of membrane thickness variation is one of the important points of its mechanical characterization. Since the membrane can be regarded as an element similar to that of thin planparallel plate, the Fizeau interferometric scheme makes an advantage of a rather simple experimental realization. As known, in the near IR region silicon material is transparent, but at the thickness of no more than several micrometers, the silicon transparency even for visible region is enough to pass the light twice through the thickness. The coherent light reflected from both the front and the back membrane surfaces interferes and creates the interference fringes. The light intensity in the interference field of two beams is expressed by the known equation

$$I = I_1 + I_2 + 2\sqrt{I_1 I_2} \cos\left(\frac{4\pi}{\lambda}nh - \pi\right), \quad (2.96)$$

where  $I_1$ ,  $I_2$  are the intensities of the beams reflected from the front and the back sides, respectively,  $\lambda$  is the light wavelength,  $n$  is the index of refraction of the membrane material and  $h$  is

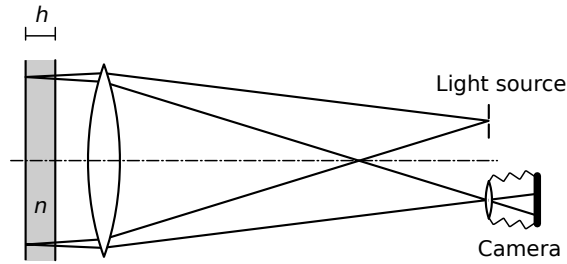


Fig. 2.29. Fizeau interferometrical scheme for membrane equal thickness mapping [24].

the membrane thickness.

The coefficients of light reflection at silicon-air interfaces are favourable due to high value of silicon index of refraction, and for the red light they are almost optimal to secure approximately equal amounts of light reflected backward from both the membrane sides. In the case of weak absorption contrast of the interference fringes is defined by the following expression

$$\eta = \frac{2(1 - R)e^{-\alpha h}}{1 + [(1 - R)e^{-\alpha h}]^2}, \quad (2.97)$$

where  $R$  is the reflectivity of the membrane surfaces at perpendicular illumination

$$R = \left( \frac{n - 1}{n + 1} \right)^2 \quad (2.98)$$

and  $\alpha = 4\pi\kappa/\lambda$  is absorption coefficient,  $\kappa$  is the imaginary part of index of refraction.

Inserting into Eq. (2.98) the actual value of the index of refraction ( $n = 3.89$ ) for silicon material at  $\lambda = 632.8$  nm (He-Ne laser) an excellent contrast of interference pattern is obtained without any absorption:  $\eta = 91\%$ . The light absorption in silicon slightly reduces this value to  $\eta > 83\%$  (see Eq. 2.97) but still the contrast remains very good. When green laser ( $\lambda = 532$  nm) was used, the contrast showed significant decrease to the value of  $\eta = 56\%$  caused mainly by stronger absorption.

Besides the good stability, the Fizeau interferometrical scheme realization provides also distinct fringe value – the constant  $c_h$  which characterises the thickness change between two neighbouring fringes.

$$\Delta h = N \frac{\lambda}{2n} = N c_h. \quad (2.99)$$

Regarding the high value of silicon index of refraction and also the double passing of the light through the membrane, the measuring sensitivity – the fringe value is as high as  $c_h = 81$  nm. Moreover, the sensitivity can be increased substantially by numerical image processing using functional interpolation between neighbouring fringes. If necessary, by such a way the thickness changes are detected with the resolving power of a few nanometers.

To observe the interference fringes, a simple optical scheme was arranged (see Fig. 2.29). In the experimental setup, He-Ne (632.8 nm/40 mW) laser was used and the interference patterns

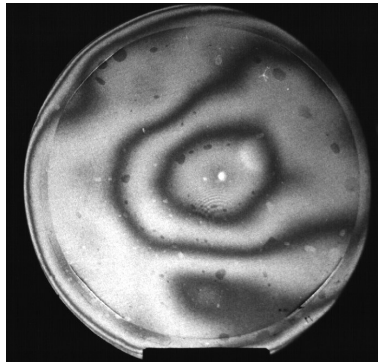


Fig. 2.30. Interference fringes of the membrane thickness variations.

were recorded alternatively by photographic or CCD camera. In the setup, a large 6-inch diameter objective with focal distance  $f = 1\,000$  mm was used. By such a means, the whole area of the membranes up to 150 mm in diameter was observed.

As an illustrative example, the map of thickness variations is shown in Fig. 2.30. Good contrast and lateral resolution of the pattern enables us to see also the details at the membrane boundaries after optical magnification. As the interference fringes are visible also on a part of carrier SOI wafer silicon ring, potential defects of the membrane boundary can be inspected.

### 3 Speckle interferometry

#### 3.1 Optical system of holographic/speckle interferometer

Simplified scheme of basic optical setup of the holographic interferometer is shown in Fig. 3.1. Spherical lens with focal distance  $f$  projects the image of the object surface to an image plane  $z = z_2$ , where a hologram is created by interference with off-axis reference wave. A diffusely scattered surface of the object is deformed by loading or moving in the interval between the first and the second exposures of double-exposure hologram.

The double-exposure image-plane hologram is registered as a result of interference of the reference wave  $a(x_0, y_0)$  with the waves in the image plane corresponding to the both states of the observed object. The surface of object is illuminated by a plane wave with complex amplitude

$$a_I(x, z) = a_I \exp[i(k(x \cos \alpha_x + z \cos \alpha_z) + \varphi)], \tag{3.1}$$

where  $a_I$  is the amplitude of light field,  $\varphi$  is the phase of the wave at the origin of coordinate system and  $\cos \alpha_x, \cos \alpha_z$  are the direction cosines of the wave along the light propagation,  $k = 2\pi/\lambda$  (where  $\lambda$  is the wavelength) is the wave number. Complex amplitude immediately after the reflection off the object is as follows

$$a_0(x_0, y_0) = r(x_0, y_0) \exp[ik(x_0 \cos \alpha_x + z_0 \cos \alpha_z)], \tag{3.2}$$

where  $r(x_0, y_0)$  is the amplitude reflectance of the object surface and the initial phase  $\phi$  at the point  $P$  equals zero.

As we consider the linear optical system, field amplitude in the image plane  $z = z_2$  can be expressed by superposition integral

$$a_2(x_2, y_2) = \iint_{-\infty}^{\infty} a_0(x_0, y_0) h(x_0, y_0, x_2, y_2) dx_0 dy_0, \tag{3.3}$$

where  $h(x_0, y_0, x_2, y_2)$  is the impulse response of the system, i.e. amplitude formed in the plane  $z = z_2$  by a point-like source located at the point  $P(x_0, y_0)$ .

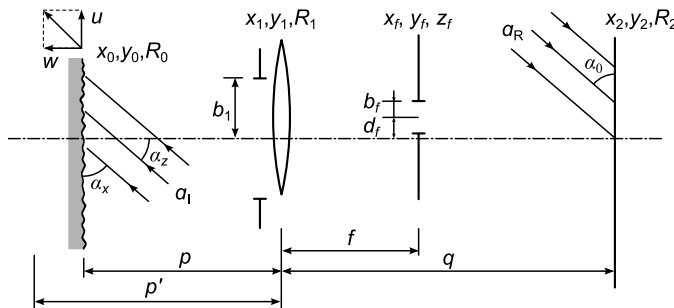


Fig. 3.1. Simplified scheme of basic optical set up of the holographic interferometer.

To acquire the point response of the system, in the object plane we have chosen a point-like source described as  $\delta$ -function with coordinates  $(x_0, y_0, -w)$ . Then, after passing the wavefront through the diaphragm with aperture function  $P_1(x_1, y_1)$  and the lens we obtain the well known impulse response in the image plane

$$a_2(x_2, y_2, x_0, y_0) = \frac{e^{ikq}}{i\lambda q} \iint_{-\infty}^{\infty} a_1^+(x_1, y_1) \times \exp \left[ ik \frac{(x_2 - x_1)^2 + (y_2 - y_1)^2}{2q} \right] dx_1 dy_1, \quad (3.4)$$

where now we have not considered the diaphragm in focal plane. After proper substitutions we have

$$a_2(x_2, y_2, x_0, y_0) = \frac{e^{ik(p'+q)}}{\lambda^2 p' q} \exp \left[ ik \left( \frac{x_0^2 + y_0^2}{2p'} + \frac{x_2^2 + y_2^2}{2q} \right) \right] \iint_{-\infty}^{\infty} P_1(x_1, y_1) \times \exp \left[ \frac{ik}{2} \left( \frac{1}{p'} + \frac{1}{q} - \frac{1}{f} \right) (x_1^2 + y_1^2) \right] \times \exp \left[ -2\pi i \left( \frac{x_0}{p'} + \frac{x_2}{q} \right) x_1 - 2\pi i \left( \frac{y_0}{p'} + \frac{y_2}{q} \right) y_1 \right] dx_1 dy_1. \quad (3.5)$$

Considering the very small values of the out-of-plane displacements, which is always the case, at the first approximation when  $w \ll p$  we can use approximation

$$\frac{1}{p'} = \frac{1}{p+w} \approx \frac{1}{p} - \frac{w}{p^2}, \quad (3.6)$$

With the following substitutions

$$\xi_2 = \frac{1}{\lambda q} \left[ x_2 + Mx_0 \left( 1 - \frac{w}{p} \right) \right]; \quad \eta_2 = \frac{1}{\lambda q} \left[ y_2 + My_0 \left( 1 - \frac{w}{p} \right) \right], \quad (3.7)$$

the expression Eq. (3.5) becomes

$$a_2(x_2, y_2, x_0, y_0) = \exp \left[ ik \left( w + p + q + \frac{x_0^2 + y_0^2}{2(p+w)} + \frac{x_2^2 + y_2^2}{2q} \right) \right] \times \iint_{-\infty}^{\infty} P_1(x_1, y_1) \exp \left[ \frac{ik}{2} \left( -\frac{w}{p^2} + \frac{1}{p} + \frac{1}{q} - \frac{1}{f} \right) (x_1^2 + y_1^2) \right] \times e^{-i2\pi(\xi_1 x_1 + \eta_1 y_1)} dx_1 dy_1, \quad (3.8)$$

$$a_2(x_2, y_2, x_0, y_0) = \frac{J_1(2\pi \varrho_2 b_1)}{\varrho_2} \exp \left[ ik \left( w + p + q + \frac{x_0^2 + y_0^2}{2(p+w)} + \frac{x_2^2 + y_2^2}{2q} \right) \right], \quad (3.9)$$

where  $J_1(2\pi \varrho_2 b_1)$  is the Bessel function of the first kind and first order and  $\varrho_2$  is the polar radius in coordinate system  $\xi_2, \eta_2$ . The Bessel function forms spherically symmetrical area with the

centre in  $(x_2, y_2)$  at  $\xi_2 = \eta_2 = 0$

$$x_2 = -Mx_0 \left(1 - \frac{w}{p}\right); \quad y_2 = -My_0 \left(1 - \frac{w}{p}\right). \quad (3.10)$$

In addition to the amplitude, the holographic record registers also information about phase distribution of the light field. Therefore, the phase terms in the expressions cannot be ignored as it is usually done. It can be seen from the expression Eq (3.10) that the phase distribution of the field is also a function of coordinates of the surface point, which is the second phase factor in Eq (3.9). This effect complicates the evaluation of obtained double-exposure interferograms. Taking into account that the quadratic term represents the parabolic approximation of the spherical surface with the radius  $p'$  centered at the center of the lens, small objects do not have to consider it. It implies that uncertainty in the phase differences can be neglected when the object is several times smaller than the lens, as it is in the order of tenths of a percent. For objects with dimensions comparable with that of lens diameter it can be avoided by the introduction of the binary spatial filter-diaphragm with a small hole in the focal plane which suppresses the phase factor. In addition the filter, as we show further, allows to change the cross-correlation conditions between records at the first and the second exposures.

Let the diaphragm with the diameter of circular opening  $b_f$  be shifted off the optical axis to a distance  $d_f$  (Fig. 3.1). Then the complex amplitude at the image plane is as follows

$$a'_f(x_f, y_f) = \frac{e^{ik(1-f)}}{i\lambda(q-f)} \iint_{-\infty}^{\infty} P_f(x_f, y_f) a_f^-(x_f, y_f) \times \exp \left[ ik \frac{(x_2 - x_f)^2 + (y_2 - y_f)^2}{2(q-f)} \right] dx_f dy_f, \quad (3.11)$$

where  $P_f(x_f, y_f)$  is aperture function of the binary filter. After substituting the complex amplitude immediately after the lens and the amplitude in front of the filter into Eq. (3.11) and next rearranging of the terms we get

$$\begin{aligned} a'_2(x_2, y_2, x_0, y_0) &= \exp \left[ ik \left( p' + q + \frac{x_2^2 + y_2^2}{2(q-f)} \right) \right] \iint_{-\infty}^{\infty} P_f(x_f, y_f) \\ &\times \exp \left[ ik \left( \frac{x_f^2 + y_f^2}{2f} + \frac{x_0^2 + y_0^2}{2p'} \right) \right] \iint_{-\infty}^{\infty} P_1(x_1, y_1) \exp \left( ik \frac{x_1^2 + y_1^2}{2f} \right) \\ &\times \exp \left[ -2\pi i \left( \frac{x_f}{\lambda f} + \frac{x_0}{\lambda p'} \right) x_1 - 2\pi i \left( \frac{y_f}{\lambda f} + \frac{y_0}{\lambda p'} \right) y_1 \right] dx_1 dy_1 \\ &\times \exp \left[ ik \left( \frac{x_f^2 + y_f^2}{2(q-f)} - \frac{x_2 x_f + y_2 y_f}{q-f} \right) \right] dx_f dy_f, \end{aligned} \quad (3.12)$$

where we have omitted constant factors. Considering that  $r_1 \gg r_f$ , the aperture function  $P_1(x_1, y_1)$  can be set equal to one through the whole plane  $(x_1, y_1)$ , and the impulse response of the system is determined in a considerable degree by the aperture  $P_f(x_f, y_f)$ . Then the inner integral represents a Fourier transform of  $\exp [i\pi(x_2^2 + y_2^2)/\lambda p']$ , and its solution in domain of spatial frequencies  $\xi_f, \eta_f$  is [26]

$$Y_f = i\lambda p' e^{-i\pi\lambda p'(\xi_f^2 + \eta_f^2)}, \quad (3.13)$$

where

$$\xi_f = \frac{1}{\lambda} \left( \frac{x_f}{f} + \frac{x_0}{p'} \right); \quad \eta_f = \frac{1}{\lambda} \left( \frac{y_f}{f} + \frac{y_0}{p'} \right). \quad (3.14)$$

After the substitution into Eq. (3.12) and following adjustment, the quadratic term  $\exp [i\pi(x_0^2 + y_0^2)/\lambda p']$  vanishes and for  $a'_2(x_2, y_2, x_0, y_0)$  we get

$$\begin{aligned} a'_2(x_2, y_2, x_0, y_0) &= e^{ik(p'+q)} \exp \left[ 2 \frac{ik}{q-f} (x_2^2 + y_2^2) \right] \\ &\times \iint_{-\infty}^{\infty} P_f(x_f, y_f) \exp \left[ \frac{ik}{2f} \left( 1 - \frac{p}{q} - \frac{p}{f} \right) (x_2^2 + y_2^2) \right] \\ &\times \exp \left[ -\frac{2\pi i}{\lambda} \left( \frac{x_2}{q-f} + \frac{x_0}{f} \right) x_f - \frac{2\pi i}{\lambda} \left( \frac{y_2}{q-f} + \frac{y_0}{f} \right) y_f \right] dx_f dy_f. \end{aligned} \quad (3.15)$$

By applying the approximation of Eq. (3.6), the integral in Eq. (3.15) is treated again using Fourier transform in domain of spatial frequencies  $\xi'_2, \eta'_2$ :

$$\xi'_2 = \frac{1}{\lambda} \left( \frac{x_2}{q-f} + \frac{x_0}{f} \right); \quad \eta'_2 = \frac{1}{\lambda} \left( \frac{y_2}{q-f} + \frac{y_0}{f} \right). \quad (3.16)$$

Due to the circular symmetry of  $P_f(x_f, y_f)$  let us rewrite the integral  $Y'_2$  from Eq (3.15) in polar coordinates

$$\begin{aligned} r_f &= \left[ (x_f - d_f)^2 + y_f^2 \right]^{1/2}, \\ \theta_f &= \tan^{-1} \left( \frac{y_f}{x_f - d_f} \right), \\ \rho'^2 &= (\xi'^2_2 + \eta'^2_2)^{1/2}, \\ \varphi'_2 &= \tan^{-1} \left( \frac{\eta'_2}{\xi'_2} \right). \end{aligned} \quad (3.17)$$

After substitution and simple modification we have

$$Y'_2 = e^{-i2\pi d_f \xi'_2} \int_0^{b_f} r_f dr_f \int_0^{2\pi} \exp [-i2\pi r_f \rho'_2 \cos(\theta_f - \varphi'_2)] d\theta_f, \quad (3.18)$$

the solution of which is analogous to Eq. (3.9) function  $J_1(2\pi \rho'_2 b_f)/\rho'_2$ . The complex amplitude takes the form

$$\begin{aligned} a'(x_2, y_2, x_0, y_0) &= e^{ik(p'+q)} \exp \left[ 2 \frac{ik}{q-f} (x_2^2 + y_2^2) \right] \\ &\times \exp \left[ -ikd_f \left( \frac{x_2}{q-f} + \frac{x_0}{f} \right) \right] \frac{J_1(2\pi \rho'_2 b_f)}{\rho'_2}. \end{aligned} \quad (3.19)$$

However, the aperture presence in the focal plane of the lens in the reconstruction scheme means certain practical disadvantages. Small opening considerably extends exposure times and,

especially, this configuration does not allow to record simultaneously displacement components in the directions of the coordinate axes  $x_0, y_0$ . Therefore, the process of spatial frequencies filtering was postponed to the reconstruction phase. Thus, double-exposure holograms are recorded without any aperture in the focal plane. This approach offers also other benefits.

For linearly recorded double-exposure amplitude hologram, the relationship between amplitude transmissivity  $\mathcal{T}$  and exposure is expressed as follows

$$\mathcal{T} = \mathcal{T}_0 + \beta t \left\{ 2a_{\text{R}}^2 + (a_{12}^2 + a_{22}^2) + [a_{21}(x_2, y_2) + a_{22}(x_2, y_2)] a_{\text{z}}^*(x, y) + [a_{21}^*(x_2, y_2) + a_{22}^*(x_2, y_2)] a_{\text{R}}(x, y) \right\}, \quad (3.20)$$

where  $a_{21}(x_2, y_2), a_{22}(x_2, y_2)$  are complex amplitudes of the object waves in the first and the second exposure respectively, and  $a_{\text{R}}(x, y)$  is the amplitude of the reference wave. The values  $T$  and  $\beta$  are characteristic constants of the photo-material and  $t$  is exposure time. In the reconstruction scheme, the reconstruction wave is chosen to be complex conjugate of the recording wave. Illuminating hologram by such wave, complex amplitude of the  $-1^{\text{st}}$  diffraction order in reconstructed wavefront immediately behind the hologram will be the second term of Eq. (3.20) in brackets

$$\beta t a_{\text{R}}^2 [a_{21}^*(x_2, y_2) + a_{22}^*(x_2, y_2)]. \quad (3.21)$$

It is desirable to carry out the reconstruction process in the same optical system as for the hologram recording. Photographically processed hologram should be situated nearly in the same position (oriented with emulsion to the lens) in the photo-plate holder. Afterwards it is illuminated by a plane wave spreading in the reverse direction as the reference wave during recording. Thus, the complex amplitude of the reconstruction wave would be  $a_{\text{R}}^*(x, y)$ . The use of planar wavefronts in the recording and reconstruction process simply removes problems that would arise by distortion of wavefronts passing through the thick glass photo-plates as well as aberrations resulting from the fact that the photo-emulsion always creates both the amplitude and the phase record. By such a way we ensure that the waves generated in  $-1^{\text{st}}$  order of diffraction propagate in the reverse direction to the record of object waves, according to Eq. (3.21). The resulting real image of the interferogram is observed in the object plane of the lens e.g. on a ground screen. Next it can be approved that in this plane equal undistorted phase differences are created like in the hypothetical case of the simultaneous presence of a diffuse surface in both undeformed and deformed states. Also, it is easy to show that the impulse response of the system is independent of the orientation of the ray tracing, consequently, in focal plane of the reconstruction lens, the system is characterized by the expression analogous to Eq. (3.19). The reconstructed complex amplitude in the  $z = z_0$  plane is described by the superposition integral

$$a_0(x_0, y_0) = \iint_{-\infty}^{\infty} a_2^*(x_2, y_2) e^{ik(p+q)} \exp \left[ 2 \frac{ik}{q-f} (x_2^2 + y_2^2) \right] \times \exp \left[ -ikd_f \left( \frac{x_2}{q-f} + \frac{x_0}{f} \right) \right] \frac{J_1(2\pi \rho'_2 b_f)}{\rho'_2} dx_2 dy_2. \quad (3.22)$$

Further, we express the amplitude  $a_2^*(x_2, y_2)$  using the integral from Eq. (3.3) and impulse response of the system. Assuming that the impulse response of the system with a diaphragm

aperture is determined mainly by the aperture function  $P_f(x_f, y_f)$ , leads to  $P_1(x_1, y_1) = 1$  on the whole interval. Consequently from Eq. (3.8) and Eq. (3.3) we get

$$a_2(x_2, y_2) = \iint_{-\infty}^{\infty} a_0(x_0, y_0) e^{ik(w+p+q)} e^{ik(x_0^2+y_0^2)/2p'} e^{ik(x_2^2+y_2^2)/2q} \times \frac{1}{M} \delta\left(\frac{x_2}{M} + x_0, \frac{y_2}{M} + y_0\right) dx_0 dy_0. \quad (3.23)$$

The two quadratic phase terms can be approximated according to Goodman [25]

$$e^{ik(x_0^2+y_0^2)/2p} \cong \exp\left[\frac{ik}{2p}\left(\frac{x_2^2+y_2^2}{M^2}\right)\right]. \quad (3.24)$$

The approximation is based upon the knowledge, that distribution of the light field in the area of the point of the image is affected only by vicinity of the optically conjugated surface area of the object. Eq. (3.24) is valid according to the lens equation for the geometric image of a single point, i. e. the center of diffraction pattern. Then, the integral in Eq. (3.23) might be simplified by factorization of the phase elements, and given the properties of  $\delta$ -function following expression for the amplitude  $a_2(x_2, y_2)$  is found

$$a_2(x_2, y_2) = e^{ik(w+p+q)} \exp\left[\frac{ik}{2q}\left(1 + \frac{p'}{q}\right)(x_2^2 + y_2^2)\right] \frac{1}{M} a_0\left(-\frac{x_2}{M}, -\frac{y_2}{M}\right). \quad (3.25)$$

Substituting the complex conjugate of  $a_2(x_2, y_2)$  into Eq. (3.22) it can be written

$$a_0(x_0, y_0) = \iint_{-\infty}^{\infty} e^{-ikw} \exp\left[\frac{ik}{2}\left(\frac{1}{q-f} - \frac{p'}{q^2} - \frac{1}{q}\right)(x_2^2 + y_2^2)\right] \times \exp\left[-\frac{i2\pi}{\lambda} d_f \left(\frac{x_f}{q-f} + \frac{x_0}{f}\right)\right] \frac{J_1(2\pi \varrho'_2 b_f)}{\varrho'_2} \times \frac{1}{M} a_0^*\left(-\frac{x_2}{M}, -\frac{y_2}{M}\right) dx_2 dy_2. \quad (3.26)$$

The exponent of the second phase element in the integral is nearly zero, therefore this term could be neglected. We rewrite the third term to the following form

$$\exp\left[-ik \frac{d_f}{f} \left(\frac{x_2}{M} + x_0\right)\right] \approx \exp\left[-ik \left(\frac{x_2}{M} + x_0\right) \cos \beta_x\right]. \quad (3.27)$$

It expresses the same phase distribution as a planar wave propagating at the angle  $\beta_x$  to the plane of the object surface, while its phase at the considered point  $x_0, y_0$  in the object plane of the lens is zero. Substituting the complex amplitude  $a_0(x_0, y_0)$  according to Eq. (3.2) into Eq. (3.22), and expressing planar wavefront (3.27), we get a general expression for a phase shift of a surface point on the body, which was repositioned in the interval between two exposures by the vector with coordinates  $u, w$ .

$$\exp[-ik(x_0 \cos \alpha_x + z_0 \cos \alpha_z)] = \exp[-ik(x_0 \cos \beta_x + z_0 \cos \beta_z)]. \quad (3.28)$$

Hence, the resulting condition for emerging of the interference fringes is

$$u(\cos \alpha_x + \cos \beta_x) + w(\cos \alpha_z + \cos \beta_z) = N\lambda, \quad (3.29)$$

where  $N$  is the fringe order. This expression, or alternatively for the component  $v$  analogous to  $u$ , allows us to evaluate quantitatively the interference fringe with respect to the orthogonal components of the surface displacements.

As it can be seen from the expression Eq. (3.27) for the phase element, moving the aperture of the spatial filter positioned in the focal plane may be regarded as changing of the observation direction, and it can be chosen at reconstruction. When the aperture is positioned to the optical axis of system, Eq. (3.29) of interference pattern interpretation is simplified

$$u \cos \alpha_x + w(\cos \alpha_z + 1) = N\lambda. \quad (3.30)$$

Provided that the object at the recording is illuminated by planar wave propagation along the optical axis of the system, the next relationship will be valid for the interference fringes

$$w = \frac{N\lambda}{2}. \quad (3.31)$$

The resulting interferogram represents an interferogram of the out-of-plane component  $w$  separated from the in-plane components  $u$  and  $v$ .

Besides the possibility of choosing the observation direction, spatial frequencies filtering in the reconstruction phase provides also other advantages. For example, when recording double-exposure holograms whole surface of the lens aperture is used and exposure time may not be so long. Diffuse object surface reflects only a few percent of the incident light, thus increasing of the effective opening diameter, seeing that the exposure time falls quadratically, can be noticeable.

Other interesting features of holography include the possibility of recording and reconstruction of non-distorted image of an object through optically distorting medium. When reconstructing holographic interferograms in the same optical system with imaging lens, the various aberrations of the lens are compensated by itself. Reconstructed image on the ground screen placed in the object plane of the lens is therefore an exact copy of the object surface with fringes. These interference fringes will be localized in the plane of the ground screen.

Nevertheless, the most important property of such double-exposure hologram is an opportunity to evaluate the in-plane components of surface displacements. The separation of these components can be performed in a manner known from speckle interferometry. First of all the pointwise filtering with unexpanded laser beam can be carried out to search for Young's fringes as it is convenient in standard double-exposure specklegram. Regardless of "parasitic"  $\pm 1^{\text{st}}$  diffraction orders due to diffraction on the carrier frequency of holographic record the laser beam forms a central diffraction halo with fringes of well-defined fringe spacing and orientation. By point by point scanning of the record, complete information on the map of in-plane displacements can be obtained.

Nevertheless, whole field of in-plane displacements can be retrieved also by whole-field filtering method. If the recorded double-exposure hologram Eq. (3.20) is illuminated by a convergent wavefront, three diffracted beams appear behind it. Two of them on the outer space carry information on the displacement component  $w$  and for now are off interest. The central wave – the

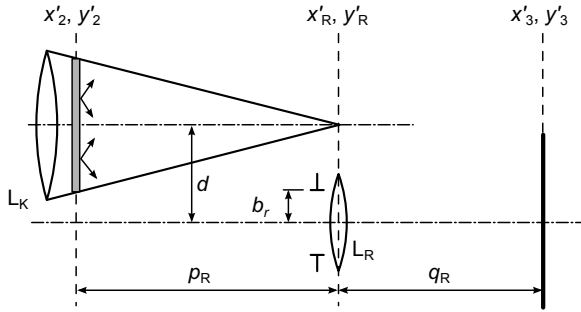


Fig. 3.2. Optical scheme of in-plane components reconstruction.

zeroth order of diffraction – is described as the second term of the brace in Eq. (3.20). Complex amplitude just behind the hologram will then be

$$(a_{21}^2 + a_{22}^2) \exp\left(-\frac{ik}{2p_R} \left[(x'_2 - d)^2 + y_2'^2\right]\right), \quad (3.32)$$

where the constants  $\mathcal{T}_0, \beta, t$  are omitted. Designation of distances and coordinates is shown in Fig. 3.2 assuming the origins of coordinate systems lay on optical axis of the lens  $L_R$ . Complex amplitude in the plane of lens  $L_R$  from the left is

$$a_{\bar{R}}^-(x_R, y_R) = \exp\left(ik \frac{x_R^2 + y_R^2}{2p_R}\right) \iint_{-\infty}^{\infty} (a_{21}^2 + a_{22}^2) e^{-ik[(x'_2 - d)^2 + y_2'^2]/2p_R} \\ \times e^{ik(x_2'^2 + y_2'^2)/2p_R} e^{-ik(x_2'x_R + y_2'y_R)/p_R} dx_2' dy_2'. \quad (3.33)$$

It is immediately seen that in the plane, where the reconstruction wave converges, Fourier's image of the hologram transparent is formed. There is, therefore, an option of spatial frequencies filtering. Placing the lens  $L_R$  with aperture  $P_R(x_R, y_R)$  into the diffraction halo, image of the object with interference fringes proportional to the planar components of displacement will be projected on the ground screen.

Let the relation (3.33) be rewritten into the form

$$a_{\bar{R}}^-(x_R, y_R) = e^{ik(x_R^2 + y_R^2)/2p_R} \iint_{-\infty}^{\infty} (a_{21}^2 + a_{22}^2) e^{-ikdx_2'/p_R} \\ \times e^{-ik(x_2'x_R + y_2'y_R)/p_R} dx_2' dy_2'. \quad (3.34)$$

Light amplitude in the image plane of the lens  $L_R$  can be found by applying diffraction integral

$$a_3'(x_3', y_3') = e^{ik(x_3'^2 + y_3'^2)/2q_R} \iint_{-\infty}^{\infty} a_{\bar{R}}^+(x_R, y_R) e^{ik(x_R^2 + y_R^2)/2q_R} \\ \times e^{-ik(x_3'x_R + y_3'y_R)/q} dx_R dy_R, \quad (3.35)$$

where  $a_R^+(x_R, y_R)$  is amplitude behind the lens  $L_R$

$$a_R^+(x_R, y_R) = a_R^-(x_R, y_R) P_R(x_R, y_R) e^{ik(x_R^2 + y_R^2)/2f_R}. \quad (3.36)$$

Substituting the combination of Eq. (3.34) and Eq. (3.36) into Eq. (3.35) we get

$$\begin{aligned} a'_3(x'_3, y'_3) = & e^{ik(x'_3, y'_3)/2q_R} \iiint_{-\infty}^{\infty} (a_{21}^2 + a_{22}^2) e^{-ikdx'_2/p_R} P_R(x_R, y_R) \\ & \times \exp \left\{ -ik \left[ x_R \left( \frac{x'_2}{p_R} + \frac{x'_3}{q_R} \right) + y_2 \left( \frac{y'_2}{p_R} + \frac{y'_3}{q_R} \right) \right] \right\} \\ & \times dx_R dy_R dx'_2 dy'_2, \end{aligned} \quad (3.37)$$

where the lens equation for  $L_R$  was used. Solving the double-integral is as follows

$$\begin{aligned} a'_3(x'_3, y'_3) = & e^{ik(x'_3, y'_3)/2q_R} \iint_{-\infty}^{\infty} (a_{21}^2 + a_{22}^2) e^{-ikdx'_2/p_R} \\ & \times \frac{J_1(2\pi \rho'_3 b_R)}{\rho'_3} dx'_2 dy'_2, \end{aligned} \quad (3.38)$$

in which  $\rho'_3$  denotes polar radius in the following spatial frequencies

$$\xi'_3 = \frac{1}{\lambda} \left( \frac{x'_2}{p_R} + \frac{x'_3}{q_R} \right); \quad \eta'_3 = \frac{1}{\lambda} \left( \frac{y'_2}{p_R} + \frac{y'_3}{q_R} \right). \quad (3.39)$$

Since registration of hologram is done by the intensity detection (photography), the quadratic phase term in front of the integral need not be taken into account. Interference fringes appear as a result of the phase stroke in the spatial frequencies domain, which is described by the linear term inside the integral. This term can be excluded in front of integral using Goodman's approximation (3.24). Thus at the reconstruction, the amplitude records of the first and the second exposures, respectively, are shifted in their phases so they will interfere. Intensity distribution in the image plane  $x'_3, y'_3$  should be

$$I(x'_3, y'_3) = [a_{21}^*(x'_3, y'_3) + a_{22}^*(x'_3, y'_3)] [a_{21}(x'_3, y'_3) + a_{22}(x'_3, y'_3)] \quad (3.40)$$

or

$$I(x'_3, y'_3) = 2a^2 \left[ e^{ik(\varphi_1 - \varphi_2)} + e^{-ik(\varphi_1 - \varphi_2)} \right] \quad (3.41)$$

while the waves are meant in a general form

$$\begin{aligned} a_{21}(x'_3, y'_3) &= ae^{ik\varphi_1}, \\ a_{22}(x'_3, y'_3) &= ae^{ik\varphi_2}. \end{aligned} \quad (3.42)$$

After rewriting Eq. (3.41) to trigonometric form we obtain

$$I(x'_3, y'_3) = 2a^2 [1 + \cos k(\varphi_1 - \varphi_2)]. \quad (3.43)$$

For the interference fringes

$$\varphi_1 - \varphi_2 = N\lambda, \quad (3.44)$$

where  $N$  is the fringe order.

Applying the lens equation and Eq. (3.10) we get

$$\frac{x'_3 d}{q_R} = -\frac{x'_2 d}{p_R} = \frac{M(1-w/p)x_0 d}{p_R}. \quad (3.45)$$

Then,

$$u + \frac{x_{02}}{p} w = N_x \frac{\lambda p_R}{M d}. \quad (3.46)$$

Displacements in  $y$  direction can be determined in the same manner as in direction  $x$ . The only difference is that the aperture of the lens  $L_R$  is placed near the diffraction halo edge in the  $y$  axis

$$v + \frac{y_{02}}{p} w = N_y \frac{\lambda p_R}{M d}; \quad (3.47)$$

Eq. (3.46) and Eq. (3.47) are the basic formulas for the interpretation of interference fringes of in-plane components. The second term on the left side involves the quantity  $w$  and can be calculated on the basis of the component evaluation according to Eq. (3.31). The influence of this term is usually very small and it diminishes in the vicinity of the optical axis. Therefore, for a smaller object and larger diameter lens, we can achieve the interference pattern which represents fringes of constant values of in-plane  $u$  or  $v$  displacement components quite well.

An interesting and favorable feature of expressions in Eq. (3.46) and Eq. (3.47), from the experimental point of view, is their dependence on the parameters  $M, d, p_R$ . It allows to change the interference sensitivity to a certain extent. In reconstruction the sensitivity constant

$$c_d = \frac{\lambda p_R}{M d} \quad (3.48)$$

may be improved/reduced by increasing the distance  $d$ . The range of measured displacements is limited from below by sensitivity of the interferometer to the smallest displacement which can be measured (as the first order interference fringe). The best value of  $p_R/d$  ratio is determined by the dimensions of diffraction halo, when the lens aperture in reconstruction is placed near the halo. Next we have proven that the dimension of diffraction halo is unambiguously determined by the recording lens numerical aperture. Let us express the amplitude  $a'_R(x'_R, y'_R)$  in the focal plane of the convergent wave by means of coordinates with origin on the optical axis of the lens  $L_K$  (Fig. 3.2). It can be done by Fourier transformation of amplitude transmissivity function of an image-plane hologram. Since the phase terms do not influence the intensity distribution in the diffraction halo, they will be omitted. In the diffraction integral we substitute the amplitude transmissivity function according to Eq. (3.9)

$$a'_R(x'_R, y'_R) = \iint_{-\infty}^{\infty} \frac{J_1^2(2\pi Q_2 b_1)}{Q_2^2} \exp \left[ -\frac{ik}{p_R} (x_2 x'_R + y_2 y'_R) \right] dx_2 dy_2. \quad (3.49)$$

Substituting the coordinates  $x_2, y_2$  by means of Eq. (3.7) (when out-of-plane component  $w$  is neglected) the integral takes the form

$$a'_R(x'_R, y'_R) = \iint_{-\infty}^{\infty} \frac{J_1^2(2\pi \varrho_2 b_1)}{\varrho_2^2} \exp \left[ -i2\pi \frac{q}{p_R} (\xi_2 x'_R + \eta_2 y'_R) \right] d\xi_2 d\eta_2, \quad (3.50)$$

whose solution is the following function [26]

$$a'_R(x'_R, y'_R) = \begin{cases} 2 \cos^{-1} \frac{r'_R}{2b_1} - \frac{r'_R}{b_1} \left[ 1 - \left( \frac{r'_R}{2b_1} \right)^2 \right]^{1/2}, & \text{for } r'_R < 2b_1, \\ 0, & \text{for } r'_R > 2b_1, \end{cases} \quad (3.51)$$

where

$$r'_R = \frac{q}{p_R} (x_R'^2 + y_R'^2)^{1/2}. \quad (3.52)$$

After the replacement of  $q = f(M + 1)$ , in the illuminated area the following relationship applies

$$\frac{f(M + 1)}{2b_1} \leq \frac{p_R}{(x_R'^2 + y_R'^2)^{1/2}}, \quad (3.53)$$

from which a clear dependence of the best ratio  $p_R/d$  on the lens numerical aperture  $f/2b_1$  follows. The sensitivity constant  $c_d$  will be expressed according to the recent relation as

$$c_d \leq \frac{\lambda f}{2b_1} \left( 1 + \frac{1}{M} \right). \quad (3.54)$$

It is known that well corrected lenses have a ratio of diameter to the focal length of no more than  $\sim 1/1.4$ . This value is the main limiting factor for the sensitivity of the interferometer layouts. Besides using smaller wavelengths the only possibility of increasing the sensitivity is to magnify the image recorded on hologram as seen from Eq. (3.38). For example, changing the image magnification from 1/1 to 2/1 increases the sensitivity of the interferometer 1.33 times. Theoretically, twofold increase in sensitivity with regard to the magnification 1/1 can be achieved (at infinite image magnification). Dependences of reciprocal values of the constant  $c_d$  and image magnification on the hologram are plotted in Fig. 3.3 for different lens numerical apertures.

In all the derived relations for the interpretation of interferograms of displacement components we have assumed the expressions to be valid also for diffuse scattered coherent light. This means that in the double exposure records the correlation of the recorded holograms must not be infringed. In practice, the vicinity of points on diffusing surface are moved piecewise as a whole, because the gradients of displacement in the neighborhood are not too large, so the surface microstructure is changing slightly. For the formation of interferogram is, however, necessary that the considered quantities of displacements did not exceed the size of coherence area on the reconstructed image. The area of coherence in diffuse coherence radiation is equal to mean size of laser speckles, which is determined by the impulse response of the system, see Eq. (3.9),

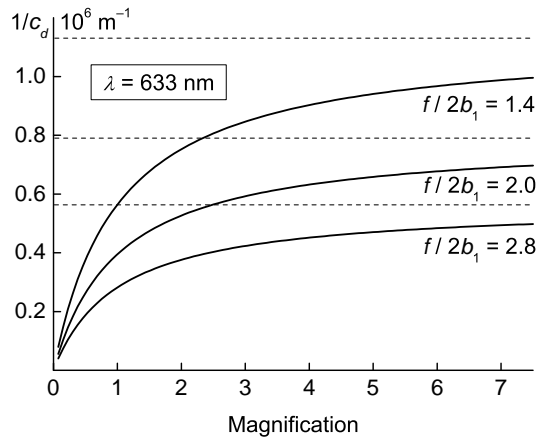


Fig. 3.3. Dependences of the constant  $c_d$  and image magnification on the hologram [27].

Eq. (3.19) or Eq. (3.38), respectively. The relationships reflect reality more or less correctly, in practice, however, they may sufficiently express the statistical average values.

Correlation properties of light speckles recorded during both the first and the second exposures, which are observed simultaneously at reconstruction, determine directly the contrast of the interference image. Hence, the value of displacements of the surface points should not exceed the characteristic dimensions of the laser speckles, otherwise the contrast of interference fringes is reduced to zero and the interferogram disappears. However, the interferogram could also be obtained from such records, provided that the degree of cross-correlation of the records for both exposures was improved in the process of reconstruction. It is possible to increase the coherence area during the component  $w$  reconstruction by reducing the aperture of the spatial filter as well as by the appropriate choice of the diameter of diaphragm aperture of the lens  $L_R$  thereby to improve contrast of the fringes. Continuously varying aperture in reconstruction allows to select visually the optimal contrast and speckle structure of the image.

When observed interference patterns of in-plane displacements, the low contrast of fringes is visible at a glance even when using small aperture  $P_R$  of the filtering diaphragm. The main reason is in the lacking of any carrier frequency and the image of an object with interferogram is reconstructed via light diffraction on the hologram laser speckles in the zero order of diffraction. The quality of these fringes could be substantially improved using double-aperture (or alternatively four-aperture) diaphragm of the imaging lens. This will create a double-aperture interferometer type, which provides more contrast interferograms of in-plane components. By such means the double-aperture type interferometer is built, which provides more readable interferogram of in-plane components [28, 27]. The basic principle of creating an interference pattern in this interferometer is very close to the standard speckle scheme with spatial frequencies filtering, as described by relations Eq. (3.38), Eq. (3.46), Eq. (3.47).

Optical layout of the double-aperture type interferometer is shown in Fig. 3.4. The aperture diaphragm  $C$  with two or four circular openings is placed in front of the lens  $L$  with focal length  $f$ . Using four aperture openings allows simultaneous recording of both in-plane components  $u$

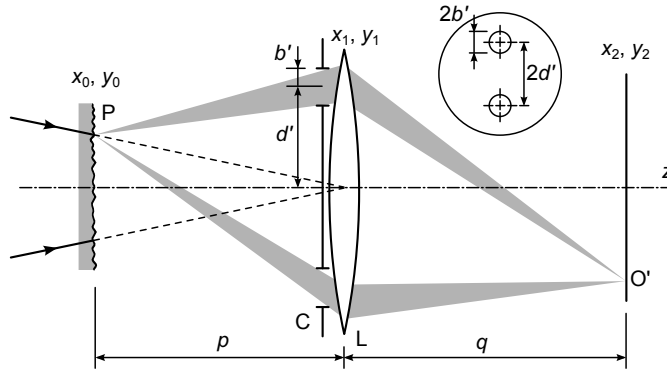


Fig. 3.4. Double-aperture type interferometer for in-plane components of displacements measurement.

and  $v$ . The distance of two holes is  $2d'$ , their diameter is  $2b'$ . Coherent wave that illuminates the object is either reflected from the opaque diffusing surface, or passes through the transparent model  $M_0$  and subsequently is diffused by its ground-screen-like face. The transparent scheme with one diffused object was used to record the isothetics. Isothetics are the fringes of the same values of in-plane displacements. The basic idea of the interferometer comes from the wavefront division emanating from the points on diffusing surface into two parts. If the lens aperture is screened only by one opening, the image of diffuse surface on the holographic plate created in coherent light consists of a variety of irregular interference maxima and minima – laser speckles. When light passes through both the openings of a double-aperture diaphragm, the wavefronts from the first and the second apertures are impinging on a holographic plate at certain angle, so they interfere. The resulting image of laser speckles is modulated by periodic grating. Illuminating such record, image of the diffuse surface can be reconstructed.

Based on diffraction theory we derive the creation of holographic recording and the formation of the interferogram in displacement fringes measurement. Impulse response of the system is expressed in Eq. (3.8) with the following conditions: the double-aperture function equals to unity in circles of radius  $b'$  distanced from the optical axis by  $\pm d'$ . Complex amplitude of the diffraction pattern in the plane  $z = z_0$  is

$$a'_2(\xi_2, \eta_2) = \frac{J_1(2\pi\varrho_2 b')}{\varrho_2} e^{i2\pi d' \xi_2}, \quad (3.55)$$

where the constant terms were omitted. The same procedure gives complex amplitude for the second aperture opening and the resulting amplitude of the both circles will be the sum of both

$$a_2(\xi_2, \eta_2) = \frac{J_1(2\pi\varrho_2 b')}{\varrho_2} \left( e^{i2\pi d' \xi_2} + e^{-i2\pi d' \xi_2} \right). \quad (3.56)$$

Intensity distribution of the diffraction pattern is the squared amplitude

$$I(\varrho_2) = \frac{J_1^2(2\pi\varrho_2 b')}{\varrho_2^2} \left( 2 + e^{i4\pi d' \xi_2} + e^{-i4\pi d' \xi_2} \right) \quad (3.57)$$

and finally, in trigonometric form

$$I(\varrho_2) = \frac{J_1^2(2\pi\varrho_2b')}{\varrho_2^2} \cos^2(2\pi d' \xi_2). \quad (3.58)$$

This result can be interpreted as diffraction pattern of one of the circular openings modulated by  $\cos^2(2\pi d' \xi_2)$ . Thus, in the diffraction pattern the distribution of intensity is formed, which corresponds to the linear so-called sinusoidal grating with the fringes perpendicular to the flowline between the aperture holes. The grating frequency  $f_0$  is determined according to Eq. (3.58) by two consecutive zero values

$$f_0 = \frac{2d'}{\lambda q}. \quad (3.59)$$

Double-exposure record on photographic material with linear characteristics can be considered as the transparent with amplitude transmissivity

$$\mathcal{T}'_2(x_2, y_2) = \mathcal{T}'_{21}(x_2, y_2) + \mathcal{T}'_{22}(x_2, y_2), \quad (3.60)$$

where  $\mathcal{T}'_{21}(x_2, y_2) + \mathcal{T}'_{22}(x_2, y_2)$  are the transmissivities of the first and the second exposures. The proper reconstruction scheme of such record is analogous to the conventional filtration in Fourier transform plane (Fig. 3.2). The diffraction field in the hologram plane is

$$a'_{2R}(x_2, y_2) = e^{-i\pi(x_2^2 + y_2^2)/\lambda p_R} \mathcal{T}'_2(x_2, y_2). \quad (3.61)$$

Further we substitute transmissivities  $\mathcal{T}'_{21}(x_2, y_2)$ ,  $\mathcal{T}'_{22}(x_2, y_2)$  by means of Eq. (3.57), where we assumed the coordinates in the first and second exposition to be  $(x_{01}, y_{01}, 0)$  and  $(x_{02}, y_{02}, -w)$ . Let us consider wavefronts observed in  $+1^{\text{st}}$  or  $-1^{\text{st}}$  order of diffraction

$$\begin{aligned} a'_{2R}(x_2, y_2) = & \frac{J_1^2(2\pi\varrho_{21}b')}{\varrho_{21}^2} e^{i4\pi d'(x_2 + Mx_{01})/\lambda q} \\ & + \frac{J_1^2(2\pi\varrho_{22}b')}{\varrho_{22}^2} e^{i4\pi d'[x_2 + Mx_{02}(1-w/p)]/\lambda q}. \end{aligned} \quad (3.62)$$

The phase term has to be taken into account.

As the component of displacement  $u = x_{02} - x_{01}$  is small compared to  $x_{01}, x_{02}$  after some modification of Eq. (3.62) we get

$$a'_{2R}(x_2, y_2) = \frac{J_1^2(2\pi\varrho_2b')}{\varrho_2^2} e^{i4\pi d'(x_2 + Mx_{01})/\lambda q} \left[ 1 + e^{-i4\pi d'(u + x_{02}w/p)/\lambda q} \right]. \quad (3.63)$$

In trigonometric form

$$\begin{aligned} a'_{2R}(x_2, y_2) = & \frac{J_1^2(2\pi\varrho_2b')}{\varrho_2^2} \cos \left[ \frac{4\pi d'}{\lambda q} (x_2 + Mx_{01}) \right] \\ & \times 2 \cos^2 \left[ \frac{2\pi d'}{\lambda p} \left( u + \frac{x_{02}}{p} w \right) \right]. \end{aligned} \quad (3.64)$$

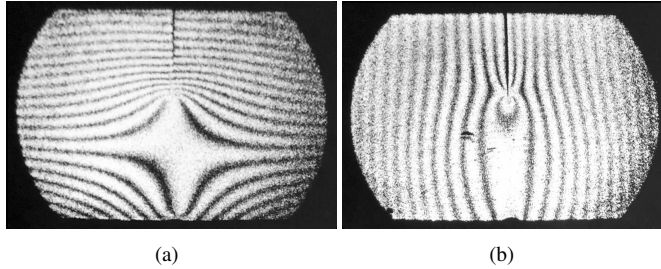


Fig. 3.5. Interference fringes of equal values of in-plane displacement components around the central crack in loaded three-point-bend beam. (a) horizontal or  $x$  component  $u$  of displacement vector, (b) vertical or  $y$  component  $v$  of displacement vector [29].

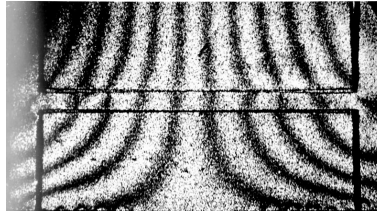


Fig. 3.6. Isothetics of horizontal in-plane component of displacement vector. PMMA model of wall was vertically loaded by constantly distributed load.

In this relation, as seen, the second factor represents sinusoidal carrier frequency and the last factor describes the interference fringes of constant displacements. Considering conditions for maxima as well as minima we obtain

$$u + \frac{x_{02}}{p}w = N \frac{\lambda p}{2d'} . \quad (3.65)$$

The displacements in the direction of  $y$  axis are determined similarly by orienting the connecting line of the holes parallel to the axis  $y$ . Interference fringes of constant components of displacements  $u$ ,  $v$  are presented in Fig. 3.5 and Fig. 3.6.

A more detailed description of the double-aperture type interferometer, its characteristics, advantages and drawbacks are in the work [27].

### 3.1.1 Experimental application of interferometer

The common equations for the interpretation of fringes were verified experimentally and used to evaluate the measurement of fringes of displacement components in the beam model with half-elliptical crack. Besides the confirmation of derived theoretical relations, the experiment had to show in particular the practical applicability of a similar interferometer in Experimental Mechanics.

Optical interferometer setup was built using conventional optical elements: He-Ne laser, collimator lens, imaging lens, beam-splitter mirror and planar mirrors. The laser beam was collimated, part of which passed through the beam-splitter mirror and another part was reflected. The part of beam passing the beam-splitter was further directed to the holographic plate and served as a reference beam. Diffuse object surface was illuminated by collimated beam and was displayed via imaging lens on the holographic plate. A He-Ne laser with relatively low power 10 mW and photo-plate Agfa E75 were used in experiments. The imaging lens had focal length of 200 mm.

One of the basic experimental problems, occurring almost always in double-exposure optical methods, is to ensure immobility of the sample as a whole when straining in the interval between exposures. Uncontrolled movement of the sample as a whole affects the resulting interferograms obtained, which can therefore be considerably distorted. When recording complete information on the deformation and movement of the body, as it is the case with simultaneous record of all three components of the displacement vector, the issue is of secondary importance, since the distortion only slightly complicates the data processing and does not affect the evaluation of element deformation. Incomplete knowledge of information on displacement vector (e.g. speckle methods) can cause significant inaccuracies in the evaluation, as pointed out e.g. in [1, 30].

It is always preferable, also in terms of simplifying the data processing, to make sure that the chosen coordinate system on the object remains stationary during loading. Frequently occurring practical problems are symmetrical samples where the origin of coordinates is to be chosen on the plane of symmetry. To ensure a better carrying out such experiments, we also developed a load frame, in which, in contrast to conventional constructions, both load points are moving. Thus, the center of the symmetrical body stays immobile during deformation. Working principle of the load frame is based on hydraulic cylinders with pistons providing tensile forces on both sides. Load forces are measured by the manometer showing the pressure in the cylinders. Axis of load pistons moves in special friction bearings allowing very accurate guidance with accuracy in order of magnitude of light wavelength.

One of the first applications where we used the interferometer for simultaneous recording of all the components of displacement vector together with the described loading frame was the measurements of displacement vector on the beam model with semi-elliptic notch imitating a narrow crack. An example of experimentally obtained interference patterns of isothetic fringes is shown in Fig. 3.7. Images on the left show the front wall of the beam with a crack, rear wall is on the right. The top two interferograms represent lines of equal values of the component  $w$  perpendicular to the displayed wall; the middle two are the interference fringes of the component  $u$  parallel to the longitudinal axis of the beam and at the bottom there are figures for the component  $v$  perpendicular to this direction.

In conclusion both advantages and disadvantages of the developed holographic-interference principle of simultaneous recording and optical separation of displacement components are briefly summarized. The proposed method makes possible (in the basic variant):

- Interferogram record of all three components of the displacement vector to one hologram in one loading process
- Direct optical recording of the components' interferograms in the reconstruction
- Simplification of the experimental procedure as well as, due to the information recording

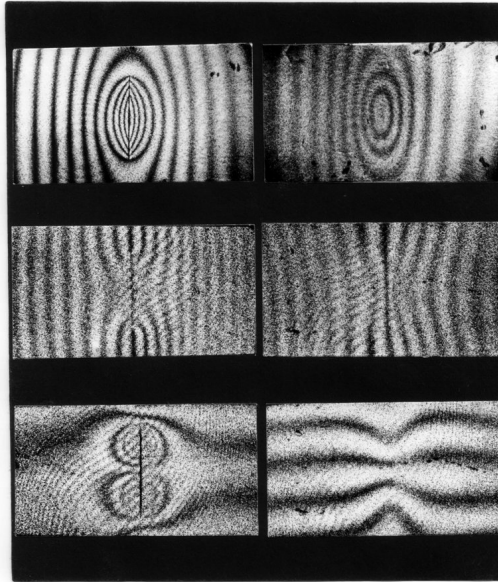


Fig. 3.7. Fringe patterns of equi-lines of out-of-plane displacement component  $w$ , and orthogonal in-plane components  $u, v$ .

in a single load process, considerable reduction of potential measurement errors compared with separate entry for each component, or records and reconstruction under the classical Alexandrov and Bonč-Brujevič scheme

- Visual selection of the fringes contrast in the reconstruction compromising between the fringes contrast and acceptable graininess of the image

Disadvantages of the method include

- Restriction to relatively small objects comparable to the size of the imaging lens
- Lower sensitivity in the planar components which is  $u_{\min} = v_{\min} \approx 2\lambda$  in comparison with the sensitivity of the component  $w_{\min} \approx \lambda/2$

Methods of experimental stress analysis allow us to determine stress components on the surface as well as in the interior of solids by evaluation of surface displacements. It is, however, not possible always to evaluate both the displacement and stress fields by experimental measurement of the object deformation only. As a rule, it becomes necessary to use analytical expressions of constitutive relation or to utilize some kind of numerical methods to supplement experimental results. The combination of finite element method (FEM) or boundary element method (BEM) with an experimental measurement of deformations is a promising solution of the problem. The BEM for the stress analysis is the method suited very well to solve two- and three-dimensional

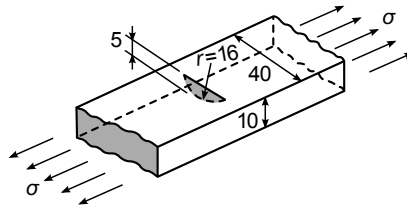


Fig. 3.8. Configuration of the beam specimen with semielliptical part-through surface crack.

problems as it reduces them to boundary solutions, i.e., only elements on the boundaries need to be defined. Depending on the completeness of the experimental data, we first studied the unknown reactions and/or displacements on the boundary of the studied region or we proceeded immediately to the calculation of the stress field at internal points of the region [31, 29].

The hybrid numerical and experimental method for the analysis of three-dimensional problems permits the determination of stress components at interior points non-destructively. The method has another advantage comparing purely numerical approach by allowing a reduction of the initial complicated problem to a problem of simple boundary/surface conditions. Moreover, it takes into account the real boundary conditions, i.e. with the friction between mechanically interacted bodies, temperature loading or other ambient conditions.

To demonstrate the hybrid experimental and numerical approach, we have chosen a three-point loaded beam with an edge crack and also the model of a large slab wall stiffened by a frame. The displacement fields of the region studied are displayed in Fig. 3.5 and Fig. 3.6. Both of these cases represent two-dimensional problem of plane stress. As a next example, suitable to demonstrate the three-dimensional stress state problem by the proposed combination of experimental-numerical method, a beam subjected to uniformly distributed tension was chosen, including part-through crack (see Fig. 3.8). The model made of PMMA was loaded and observed from four faces by holo/speckle interferometer. Recorded three orthogonal displacement vector components are in Fig. 3.7.

The experience gained with applications of the hybrid experimental-numerical method in mechanical stress state problems solution over the years has demonstrated the effectiveness of this approach and simplified the use of labor-consuming evaluation of experimental data [32].

### 3.1.2 Two-channel speckle interferometer

In view of its simplicity, the speckle method is very convenient, but during its exploitation in a mechanical laboratory the insufficient sensitivity to in-plane displacement detection has been ascertained as a strong limiting factor. Even in the electronic speckle shearing interferometry mathematical fitting must be used to interpolate the fringe positions data. In order to improve measuring sensitivity as well as some other qualities, we have proposed [33] new simple optical arrangement of the speckle camera. Unlike the single-aperture photography setup, the double-exposure speckle/holograms are recorded by a two-channel optical scheme (Fig. 3.9). Two images of the observed surface are projected independently onto the photographic plate through the reflection on the two side mirrors. By appropriate focusing, both the wavefront are imping-

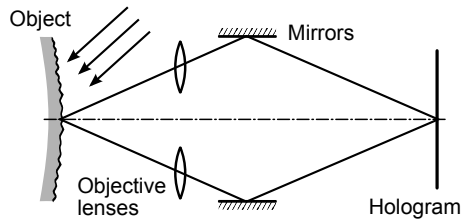


Fig. 3.9. Optical scheme of double-aperture two-channel holo/speckle interferometer [33].

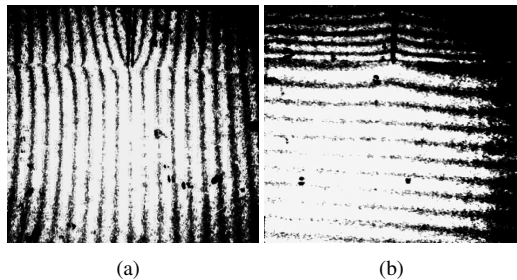


Fig. 3.10. In-plane displacement components (a)  $u$  and (b)  $v$  of a nuclear reactor vessel wall with crack.

ing on the photoplate at mutually opposite angles and create carrier frequency of the speckles, consequently, high contrast interference fringes are generated without need of additional optical filtration.

In the optical setup, the viewing angle can be enlarged 3 to 5 times comparing to standard speckle interferometry scheme with wide-open lens. As the carrier frequency of the speckles is sufficiently higher compared to the double-aperture speckle scheme, two-channel scheme provides greater opportunities how to depress decorrelation effect but also how to realize the phase shift in electronic speckle interferometry variant. Other advantages lie in smaller geometrical distortion of the image, and also in better conditions for measuring of large structures. The developed interferometer was used e.g. in experimental testing of the thermally loaded stresses across the layered structure of nuclear reactor vessel wall with crack. Fig. 3.10 shows the measured displacement field of both the orthogonal in-plane components.

### 3.2 Reconstruction of records in speckle interferometry using polychromatic light

Important place among the methods of so-called *speckle interferometry* belongs to the double-aperture-type interferometer. Its advantage lies mainly in the simplicity of experimental equipment and direct recording of fringes of equal planar components of displacement vector. Moreover the quality of interferograms is much better than the fringes obtained by Fourier filtration of *classical* specklegrams. It is a consequence of the fact that records in double-aperture-type interferometer feature carrier frequency in contrast to the usual specklegram. In fact, this blurs the

difference between double-aperture interferometer and imaging hologram records respectively, and specklegram-hologram has many properties of imaging hologram. In terms of interferometry, the most important is the possibility of white-light reconstruction as well as precise fringes localization on the surface of the measured object.

The essential element of double-aperture-type interferometer is a lens with double-aperture barrier in front of it. Diffraction pattern of the two waves from the apertures is recorded on photo-plate in the image plane of the object. Diffraction pattern of a single point coherent source is given by Fraunhofer diffraction of the appropriate aperture shape function [26, 27]. Then the intensity distribution can be written in the form

$$I(\varrho) = [J_1(2\pi\varrho b)/\varrho]^2 [2 + \exp(i4\pi d\xi) + \exp(-i4\pi d\xi)], \quad (3.66)$$

where

$$\xi = \frac{x_2 + Mx_0}{\lambda_0 q_0}; \quad \eta = \frac{y_2 + My_0}{\lambda_0 q_0}; \quad \varrho = \sqrt{\xi^2 + \eta^2}, \quad (3.67)$$

$\lambda_0$  is wavelength of light on the recording plane and  $M = q_0/p_0$  represents object magnification on the photo-plate.

In the reconstruction scheme of such linearly recorded hologram-specklegram, Fourier's spectrum of the transparent hologram-specklegram appears in the camera lens plane  $(x_3, y_3)$ . The transmittance of the transparent is

$$\mathcal{T}_2(x_2, y_2) = \mathcal{T}_{21}(x_2, y_2) + \mathcal{T}_{22}(x_2, y_2), \quad (3.68)$$

where

$$\mathcal{T}_{21,22} = KtI_{21,22}(\varrho) \quad (3.69)$$

are the records obtained during the first and second expositions, respectively, in the experiment of fringes of equal in-plane displacements observation. The symbol  $K$  denotes proportionality constant of the photomaterial and  $t$  is the exposure time.

The amplitude of the light field in  $(x_3, y_3)$  plane, having neglected the constant coefficients that do not affect its spatial distribution, can be expressed as follows

$$a_3(x_3, y_3) = \iint_{-\infty}^{\infty} \mathcal{T}_2(x_2, y_2) \exp\left[-i\frac{2\pi}{\lambda q}(x_2 x_3 + y_2 y_3)\right] dx_2 dy_2. \quad (3.70)$$

Substituting  $\mathcal{T}_2(x_2, y_2)$  according to Eq. (3.66), (3.68) and changing coordinates  $x_2, y_2$  by means of Eq. (3.67), the amplitude takes new form

$$a_3(x_3, y_3) = \iint_{-\infty}^{\infty} (J_1/\varrho)^2 \exp(-i4\pi d\xi) \exp[-i2\pi(f_x \xi + f_y \eta)] d\xi d\eta, \quad (3.71)$$

where

$$f_x = \frac{\lambda_0 q_0}{\lambda q} x_3; \quad f_y = \frac{\lambda_0 q_0}{\lambda q} y_3, \quad (3.72)$$

while just the second term from the bracket of Eq. (3.66) was taken, which represents the  $+1^{\text{st}}$  diffraction order. Let the Fourier transform of the function  $(J_1/\varrho)^2$  to be denoted as  $\mathcal{F}(J_1/\varrho)^2$ . Then, according to the shift theorem,  $a_3(x_3, y_3)$  represents the same function shifted in the system of coordinates by

$$x_{30} = \frac{\lambda q}{\lambda_0 q_0} 2d. \quad (3.73)$$

The last equation shows that the change in wavelength of light  $\lambda$  in the plane distanced from the transparent by  $q$  expands the spectrum, the position of the diffraction halo varies with the wavelength of reconstructing wave. Consequently, when using reconstructing white-light source, in the  $\pm 1^{\text{st}}$  orders the diffraction halo is decomposed into light spectrum. Nevertheless, as it will be shown below, the actual interference pattern that is created by following transformation in the  $(x_4, y_4)$  plane is not affected by this decomposition.

For simplified notation, assume that the center of the camera lens is located on the optical axis. Distribution of the light field after passing through the lens is

$$a'_3(x_3, y_3) = a_3(x_3, y_3) \exp \left[ -\frac{i\pi}{\lambda f} (x_3^2 + y_3^2) \right]. \quad (3.74)$$

Amplitude of wavefront incident on the film in the camera  $a_4(x_4, y_4)$  can be obtained using Fresnel's diffraction equation

$$\begin{aligned} a_4(x_4, y_4) = & \iint_{-\infty}^{\infty} a'_3(x_3, y_3) \exp \left[ \frac{i\pi}{\lambda q'} (x_3^2 + y_3^2) \right] \\ & \times \exp \left[ -\frac{i2\pi}{\lambda q'} (x_4 x_3 + y_4 y_3) \right] dx_3 dy_3. \end{aligned} \quad (3.75)$$

After substituting from Eq. (3.74) and applying simple operations we get

$$\begin{aligned} a_4(x_4, y_4) = & \iint_{-\infty}^{\infty} a_3(x_3, y_3) \exp \left[ -\frac{i\pi}{\lambda q} (x_3^2 + y_3^2) \right] \\ & \times \exp \left[ -\frac{i2\pi}{\lambda q'} (x_4 x_3 + y_4 y_3) \right] dx_3 dy_3. \end{aligned} \quad (3.76)$$

While  $x_3^2 + y_3^2 \ll q$ , the term  $\exp \left[ -\frac{i\pi}{\lambda q} (x_3^2 + y_3^2) \right]$  can be set as 1 in the first approximation. Whereas, according to Eq. (3.73), function  $a_3(x_3, y_3)$  represents function  $\mathcal{F}(J_1/\varrho)^2$  shifted in the coordinate system, the transformation Eq. (3.76) can be treated again using shift theorem. Then,

$$a_4(x_4, y_4) = (J_1/\varrho)^2 \exp(i4\pi d\xi). \quad (3.77)$$

It is seen that the amplitude distribution in the  $(x_4, y_4)$  plane is independent of  $\mathcal{F}(J_1/\varrho)^2$  shift in the  $(x_3, y_3)$  plane.

For double exposure process of moving point-like source in the object plane we get the resulting interference pattern by summing the amplitudes  $a_4(x_4, y_4)$ . In this case, it is necessary that the displacement does not exceed the radius of correlation, which is roughly the radius  $\varrho$  of the first diffraction minimum in the envelope surface of the modulation grid peaks described by the Eq. (3.66).

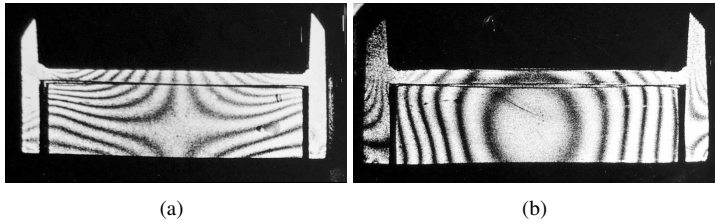


Fig. 3.11. Interference fringes of equal values of in-plane displacement components (a)  $u$  and (b)  $v$  of the wall with window loaded in vertical direction by constantly distributed load.

### 3.2.1 Application conclusions

Fig. 3.11 shows the interferogram of the displacement components on the model of wall. From the reconstructed image in white light it is easy to see that the characteristic speckle interferogram image noise is strongly suppressed. This improves resolving power and accuracy of the individual fringes identification.

Moreover, in order to ensure non-distorted interferogram reconstruction in the case of coherent light a precise location of the camera lens aperture sensing the middle of the  $\pm 1^{\text{st}}$  diffraction order halo is required. Using white-light reconstruction eliminates this problem and the interference fringes are localized on the object surface – its shape does not change with the change of the position of the objective lens. What is more, it is also possible to use non-point source of light (eg. projector). It should be remembered, however, that polychromatic light reconstructs only the records with correlated exposures. This implies the use of double-aperture element with relatively small apertures while recording, which is certainly a disadvantage with regard to the need for longer exposure time.

### 3.3 Speckle interferometry by sandwich principle

Classical double-exposure speckle interferometry is known as relatively simple and effective optical method. It is, however, often influenced by adverse factors. As the first is the fact that in double-exposure on one photo-plate the overall displacements of the observed surface in space are recorded. In technical applications these displacements often exceed the deformation of the object resulting in significant inaccuracies in evaluation. Another limitation of the classic speckle scheme is narrow range of measurable values of displacements and in particular limited ability to record the smallest values. This is, at best, an order of magnitude worse than in the holographic interferometry measurements of out-of-plane displacement. Another fact must be taken into account that in classical speckle interferometric scheme a record objective lens with large aperture is necessary to increase sensitivity of the measurement. Most lenses with such apertures are characterized by large geometric aberrations leading to significant measurement errors [34].

Using so-called sandwich principle [35] can solve problems mentioned above. The method is based on the phenomenon of interference of light diffracted on two identical structures arranged one behind another. Each of the exposures recording object in two states of deformation is done



Fig. 3.12. Interference pattern of two specklegrams positioned one behind another.

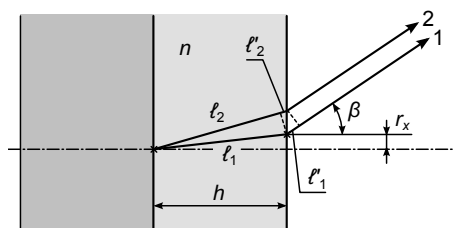


Fig. 3.13. Interference scheme of two point-like light sources placed one behind another.

on a separate photo-plate. In the information evaluation, the processed photo-plates are put onto each other with emulsions in one direction. When illuminating such a composition, corresponding pair of speckles represent a pair of consecutive – in the distance the thickness of photo-plate – point-like light sources. Diffraction on such speckle structure is a circular diffraction halo modulated by fringes in the form of concentric circles (Fig. 3.12). Figure 3.13 shows the interference scheme of two point-like light sources placed one behind another. Intensity distribution can be found when the difference of the optical paths of beams 1 and 2 is expressed

$$\Delta = n(l_1 - l_2), \tag{3.78}$$

assuming that

$$l'_1 = nl'_2, \tag{3.79}$$

where  $n$  is index of refraction of the photo-plate glass; the paths labels are in Fig. 3.13. Now we express  $l_2$  by means of Snell's law for beam 2

$$l_2 = \frac{r_x \sin \beta}{n} + \frac{h}{n} \tan \beta \left( \frac{n}{\sin \beta} - \frac{\sin \beta}{n} \right), \tag{3.80}$$

while

$$l_1 = \sqrt{r_x^2 + h^2}. \tag{3.81}$$

Symbol  $r_x$  denotes distance of the second point from the optical axis,  $h$  is photo-plate thickness and  $\beta$  is the observation angle of the considered point in the interference pattern. Since the distance of the ground-screen is large compared to  $r_x$ , the same angle  $\beta$  is considered for both the rays:  $\cos \beta = 1$ ,  $r_x \ll h$ . Light intensity on a ground-screen point is given by interference of beams 1 and 2 and can be expressed using Fresnel's formula. Provided that the amplitudes of the beams are equal, for the interference pattern applies:

$$I = I_0 \cos^2 \frac{2\pi}{\lambda} \left( \frac{h}{n} \sin^2 \beta - r_x \sin \beta \right), \quad (3.82)$$

where  $I_0$  is a constant and  $\lambda$  is wavelength of light. Hence follows the relation for interference minima or maxima, respectively, from which the quantity of mutual in-plane displacement of the point-like sources is expressed

$$r_x = \frac{h}{n} \sin \beta - \frac{N\lambda}{\sin \beta}, \quad (3.83)$$

where  $N$  is interference order.

In order to increase the accuracy of measurement, several points of interference pattern corresponding to one object point for different  $N$  and  $\beta$  ought to be taken into account. Sufficiently precise result is obtained by averaging of values  $r_x$  given by Eq. (3.83). The disadvantage of the procedure is its elaborateness – large amount of data have to be read out from the interference pattern. Therefore, simplified method for displacements evaluation is measurement of shift of concentric circles centers. The position of the center is

$$r_x = \frac{h}{n} \sin \beta, \quad (3.84)$$

where  $N = 0$  is was in Eq. (3.83). It is convenient to relate this shift to the reference position of the center determined by the object point measurement with zero displacements. Technically, we provided the measurement using diaphragm with large circular opening and ground screen with millimeter 2D scale. The centers of circles shift were determined relatively to the reticle set for the point with zero components of displacement. The accuracy of such measurement is relatively high due to the opaque transition of the circle on the ground screen. The uncertainty of circle center position was estimated to  $\pm 1$  mm, which for the screen – specklegram distance (1500 mm), photo-plate thickness 1.5 mm and the image magnification 1/3 leads to the displacement of object points uncertainty to be  $\pm 3$   $\mu$ m.

It is obvious, that in the described method the measured values of displacements are not bounded from below, even smaller quantities than the average value of diameters of laser speckles can be obtained. This is not possible in the classical scheme of Young's fringes evaluation. Sensitivity of method utilizing sandwich principle is determined only by the possible error of measurement of the fringes geometric position.

Moreover, in the sandwich method, numerical aperture of the objective lens has no effect on the limited sensitivity of measurement. Therefore, the lens can be screened to create significantly more precise image.

### 3.4 Speckle interferometry utilizing digitization of image

Holographic and speckle interferometries allow contactless deformation measuring of microscopic objects with diffusely reflecting surface. This unique capability can be used in many areas, however, it has limits and drawbacks. Considerable sensitivity to disturbances of ambient, such as light conditions and mechanical vibrations as well as complicated evaluation of the information received are the most significant. These factors limit today's holographic and speckle interferometry methods are practically limited to the optical conditions of the laboratory.

Some of these drawbacks can be avoided using a photoelectric light signal sensing – this effort, however, encounters various problems:

- photographic plate records simultaneously the whole field of view; using one discrete photodetector, one loses this advantage of wide field interferometry
- the use of CCD matrix or classic vidicon would solve the problem radically, but achievable resolution of the pixel elements of the matrix remains at least an order of magnitude lower than the value required by the microstructure of the interference pattern forming a hologram.

#### 3.4.1 Electronic speckle interferometry

Addressing the key problem of creating double-exposure interferogram at low resolution of the recording medium was actually already found in 1971. Butters and Leendertz [36] used photodetectors to measure changes in the light intensities of individual spots of the speckle structure. The main principle consists in the fact that the effective areas of the discrete sensors – CCD array elements was comparable to the size of the each spot. Typical statistically averaged dimension of spots, when imaging by lenses, have a size of 5 to 100  $\mu\text{m}$ , and can be controlled by appropriate numerical aperture of the imaging lens. These dimensions are distinguishable by classic vidicon TV camera and with camera based on CCD elements.

Since the holographic interferometry is a comparison of two object states that do not exist at the same time, an electronic recording storage device should be used. Given that there is always speckle structure recorded, the method is often referred to as Electronic Speckle Pattern Interferometry (ESPI).

The problem of the detection of light intensity variations of the individual spots is that it cannot be universally used in a variety of different optical schemes in holographic interferometry. A wide range of different configurations of optical assemblies has arisen as a result of the effort to simplify the evaluation of information on the orthogonal components of the displacement vector on the surface of the object under examination [37]. Besides the classical scheme of Fresnel holograms, often disadvantageous in terms of accuracy and complexity of the evaluation, the known schemes more or less differed from one another by appropriate choice of illumination angles and angles of observations and recorded only displacements in the direction of observation (out-of-plane), or in a direction perpendicular to the direction of observation (in-plane). Measurement of in-plane displacements without use of the reference beam is usually called speckle interferometry. In practice, generally the smallest problems of interferometry are in out-of-plane displacement measurements, in this aspect the holographic interferometry is closest to the classical interferometry, which enables such measurements only. The sensitivity of the measurements

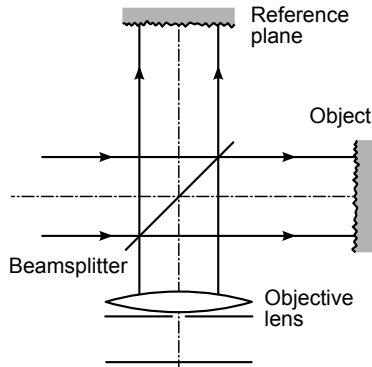


Fig. 3.14. Michelson interferometer, the reference wave is reflected from a reference diffusion surface, therefore its wavefront is very complex.

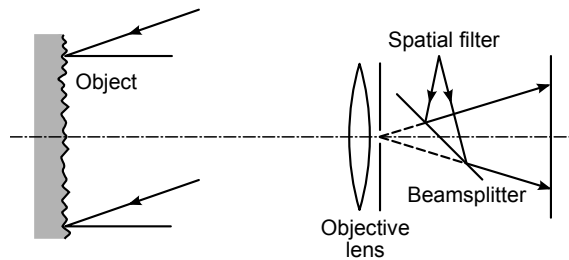


Fig. 3.15. Hologram with spherical reference wavefront.

is  $\lambda/2$  (the discrete step between two successive interference fringes).

When using the photoelectric signal sensing there are two basic principles of interferometers recording out-of-plane displacements. Both are based on the principle of a Michelson interferometer, where two mutually interfering light wavefronts are propagating along one axis. In the former case the information wavefront from the object interferes with the one reflected from a reference diffusion surface forming a very complex wavefront (Fig 3.14). In the latter case, the reference beam is a smooth spherical wavefront (Fig 3.15).

In the former case, the contrast of obtained interference fringes is very low and the range of the measured values of the normal (to the surface) displacement is quite limited by decorrelation of speckle structures in larger displacements. However, this method can be successfully applied, provided that the in-plane displacements of the object deformation are relatively small compared to the out-of-plane displacements component. Then, the mutual decorrelation of the compared records is minimal and resulting contrast of interference fringes is usually sufficient. A typical example of such a situation in mechanics is the bending deformation of thin plates. By using the method of electronic speckle correlation interferometry a number of mode shapes were observed under the dynamic excitation of the plate vibrations. A powerful loudspeaker was driven by

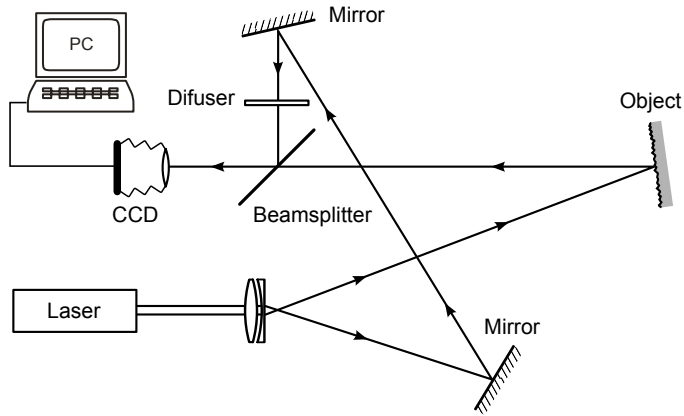


Fig. 3.16. Schematic drawing of the Electronic Speckle Correlation Interferometry intended to observe the mechanical vibrations of bending plate.

tuned harmonic generator in order to excite non-contact bending vibration of the metallic plate.

The idea of so-called time-average method was established shortly after the discovery of holographic interferometry [38]. If the object during the period of exposure vibrates with period of much less than exposure time, the multiple object states are registered on the holo/specklegram. Varying object deformations are recorded as a change in the intensity. The contribution to the total exposure of individual states of the object depends on the speed at which the object passes through these positions. On the time-average hologram interference maxima will match the immobile nodal positions points. The expression for the light intensity recorded in one frame is [39]

$$I_1 = I_0 + I_r + 2\sqrt{I_0 I_r} J_0(P) \cos \varphi, \quad (3.85)$$

where  $P = (4\pi/\lambda)w_0$ ,  $w_0$  is the maximum amplitude of the sinusoidal vibration,  $J_0(P)$  is Bessel's function of zero order.

To enhance the contrast of the resulting interference fringes, the first two terms in Eq. (3.85) should be eliminated. For this purpose, the speckle field of the object at static nonvibrating state was firstly recorded and then record of vibrating object surface at its resonant frequency was carried out. Subtracting of these two frames by image processing procedure, the fringes of nodes and antinodes are visualized with irradiance proportional to  $[1 - J_0(P)]^2$  [40].

The test object – bending plate – was illuminated by an expanded laser beam of red light emitted by 50 mW output power HeNe CW laser (Fig. 3.16). A part of wavefront of the extended illuminated beam was separated by using a mirror and directed through another mirror to a small groundscreen. Passing through the groundscreen, the light creates the speckle field directed by the semitransparent mirror into the objective lens of the CCD camera. The light reflected from the object surface is passing through this beam splitter and is projected onto the CCD matrix, where the interference of both the speckle fields happens. Any movements of object surface along the line of sight will create the changes in optical paths and thus will give rise to the pattern of interferogram. The fringes of the pattern are acquired by time-average exposure and processed

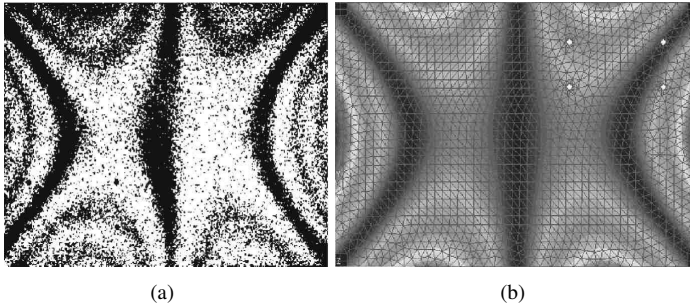


Fig. 3.17. (a) Vibrating mode visualization of the thin metallic plate at resonant frequency 247 Hz, (b) numerical simulation of the same modal shape computed by COSMOS.

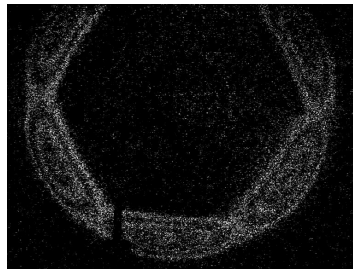


Fig. 3.18. The interference pattern of the tyre sidewall bulging shape vibrating at 3rd order radial mode of vibration – 141 Hz. Rubber tyre MATADOR Model MP 15.

in a PC by electronic substitution of both the original image speckle field and the image speckle field after deformation of object surface, caused by vibration.

The visualisation of modal structure is clear and gives us the imagination about different modal shapes. As an illustrative example, one of the mode shapes is shown in Fig. 3.17(a). At the right hand side in Fig. 3.17(b) there is also numerical simulation of the plate vibration obtained by COSMOS SW tool. The dark points in the interferogram represent nodes, bright points represent areas where amplitude of vibrations reaches approximately the value of  $\lambda$ , when  $\lambda = 632.8 \text{ nm}$  is a wave length of the laser used and  $N$  is an integer.

Another example, where ESPI was used, is the visualization of modal shapes structure of car tyres. From the viewing angle of mechanics the pneumatic tyre today is a highly sophisticated engineering structure, where viscoelastic, anisotropic and nonhomogeneous properties make reliable theoretical analysis extremely difficult. Neither the functional nor performance requirements can be adequately satisfied without a short sufficient understanding and knowledge of the strain and stress states developed within the entire composite structure under varying service conditions. In order to render such a study possible, an experimental approach was implemented.

Using the procedure of time-averaging the distribution of both vibrating surface amplitudes and corresponding knots was visualised (see Fig. 3.18). The entire spectrum of modal frequen-

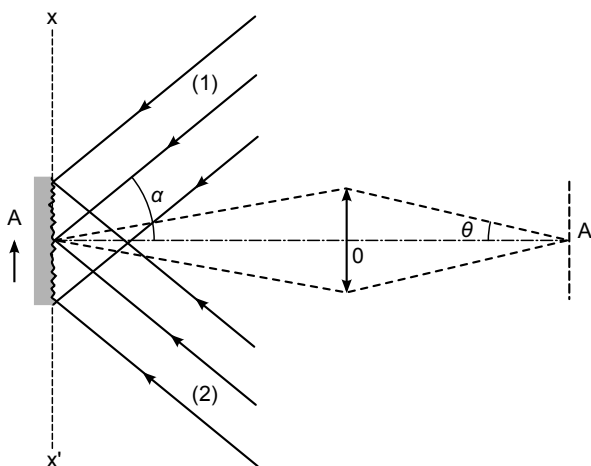


Fig. 3.19. Optical scheme of holographic interferometer providing measurements of in-plane displacements. The speckle field of two symmetric illuminating waves is completely non-sensitive to the object displacements in the optical axis.

cies of both longitudinal and radial modal shapes up to 6.order was obtained by optical electronic speckle correlation technique [41]. The vibration was excited acoustically by powerful loudspeaker at the same ESPI setup as in Fig. 3.16. The positions of nodes and anti-nodes were confronted with that identified by contact mapping of the surface by means of piezoelectric accelerometers.

In the methods where the reference beam wavefront is in the form of complicated speckle field the fringe quality is limited by a size of individual speckle and mainly by lateral movements of the object surface between exposures. The in-plane displacements are responsible to the effect of mutual decorrelation between both of the speckle records and consequently to the deterioration of interference fringes contrast. In this respect it is more advantageous to use the other scheme with a smooth reference wavefront. The optical scheme has to be adjusted in such a way that the virtual image of the point source of the reference wavefront will be matched with the center of the imaging lens aperture through the semitransparent mirror. The obtained holograms as a rule have better contrast (see Fig. 3.15). The technical problem is the increase of lateral resolution of the image (not sensitivity), i.e. finer speckle structure and also providing more distinguishable interference fringes (e.g. the average time method for the measurement of mechanical vibrations). Moreover, from a practical point of view, the mentioned optical assembly is fragile, bulky and sensitive to vibrations.

As seen, it is possible to record out-of-plane displacements using a camera equipment. In experimental practice – especially in the field of experimental mechanics – there is often a demand to monitor the displacements in the plane of surface perpendicularly to the line of sight. Unlike classical interferometry, holographic interferometry allows such measurements. Scheme of the interferometer for in-plane displacements [42] is shown in Fig. 3.19. The object is illuminated by two collimated light beams in a symmetric scheme. Each of the beams forms microscopic

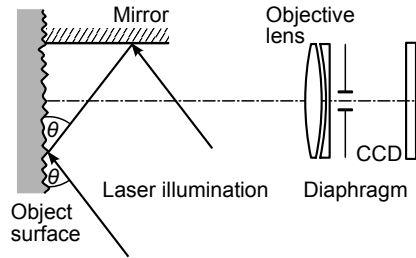


Fig. 3.20. Optical scheme of laser speckle correlation interferometer.

speckle structure in the image plane where the detector is placed. It is easy to imagine that the phase changes, when the object moves along the optical axis, are of opposite sign for both of speckle structures, thus are cancelling each other. Only the diffuse object displacements perpendicular to the optical axis are interferometrically recorded. Such an interferometer can be used in combination with CCD matrix detection. However, since in this case two mutually speckle structures interfere, the contrast of the the obtained interference fringes is very low and the range of measured displacement is also narrow.

The optical scheme of speckle interferometry for in-plane displacement measurement as it is drawn in Fig. 3.19, can be adapted to ensure more simple technical design. We tried to apply an optical method of such electronic speckle correlation interferometry (ESCI) as a tool for visualization of object deformation induced by moisture and temperature changes in porous material. In view of possibilities to map the space and time distribution of unfolded deformation, it is believed the method can be used to study the phenomena of mass and heat transport.

An optoelectronic system of CCD camera with digitizer and PC is used to perform digital image processing and appropriate correlation. The scheme of an interferometer is in Fig. 3.20. Through the reflectance on the side mirror, perpendicularly to the object surface, its diffuse plane is illuminated by two collimated light beams in a symmetric manner. Both the beams create independent speckle patterns that interfere after passing through an objective aperture and generate a resulting grained intensity variations on the CCD matrix area. From the spacing of correlation fringes in-plane strain can be evaluated. The fringe value of the measurement is

$$c_{uv} = \frac{\lambda}{2 \cos \theta}, \quad (3.86)$$

where  $\lambda$  is the wavelength of light.

In the laboratory setup we used 650 nm/12 mW coherent laser diode. The objective lens with focal length of 25 mm was diaphragmed 1/5.6. At such an aperture CCD chip Sony ICX039 with  $1280 \times 1024$  matrix can resolve the individual speckles.

It can be said, the ESCI in such a configuration is robust sufficiently and simply applicable in laboratory conditions. The roughly porous surface of building materials invokes specific limitation with the decorrelation effect between both the exposures. The effect of change in surface microstructure arose from structure changes caused by water filling of surface pores. The phenomenon of the water appearance in the surface is followed by speckle pattern decorrelation and clearly marked on the surface with such a disrupted microstructure nearly water line (see

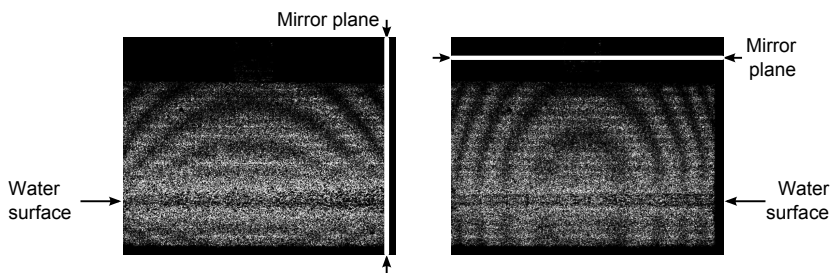


Fig. 3.21. In-plane displacement components  $u$  (left),  $v$  (right) of the bending beam deformation induced by water suction on the bottom beam surface, the fringe value was  $0.73 \mu\text{m}$ .

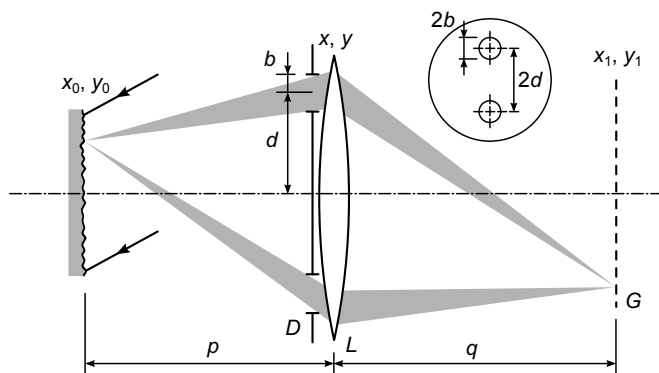


Fig. 3.22. The scheme of double-aperture speckle interferometer. Lens  $L$  is covered by double-aperture diaphragm  $D$ . Linear grating  $G$  is placed in the image plane of  $L$  with grids oriented perpendicularly to the joining line of the aperture circular openings.

Fig. 3.21). Thus, the points where the moisture is penetrated happen to be practically unobservable. The effect is observable in Fig. 3.21(a) where the suction of water was measured on freestanding beam made of porous material of AAC concrete. The contrast of interference fringes continually deteriorates upwards from the contact of the beam with water level. If initially dry material is brought in contact with liquid water, water is sucking into the material. Subject to gradients of relative humidity, an element of wetted porous medium gains fluid mass and deforms due to internal capillary pressure. In Fig. 3.21 there are orthogonal displacement components of the bending beam deformation by capillary pressure. Interesting effect on the water level is visible as a mirroring of the interference pattern.

### 3.4.2 Double-aperture speckle interferometer with electronic record

Optical scheme of the interferometer is drawn in Fig. 3.22. The lens  $L$  is covered by the diaphragm  $D$  with two circular apertures. Their diameter is  $2b$ , the distance of their centers is  $2d$ . Coherent wavefront illuminating object  $O$  is diffusely scattered on its surface. The grating  $G$  is

placed in the imaging plane of the lens  $L$ . Grid lines are oriented in a direction perpendicular to the line joining the centers of the aperture openings  $D$ . Interference pattern is sensed by a CCD camera focused on the grid  $G$ .

The basic principle of the interferometer is based on a division of wavefronts originating from the various points of the diffusion surface. Impulse response of the simple optical system can be determined as Fraunhofer diffraction at the openings of the diaphragm  $D$ . For the complex amplitude in the imaging plane we have [25]

$$a_{10}(\xi, \eta) = \frac{1}{\lambda^2 pq} \iint_{-\infty}^{\infty} P(x, y) \exp[-i2\pi(\xi x - \eta y)] dx dy, \quad (3.87)$$

where  $\lambda$  is the wavelength of light,  $p, q$  are the object and image distances, respectively,  $P(x, y)$  is aperture function, designation of the Cartesian coordinates is clear from Fig. 3.22. In Eq. (3.87)  $\xi, \eta$  are spatial frequencies defined as

$$\xi = \frac{x_1 + Mx_0}{\lambda q}, \quad \eta = \frac{y_1 + My_0}{\lambda q}, \quad (3.88)$$

where  $M = q/p$  is image magnification.

The function of the double circular aperture is equal to unity in the holes of radius  $b$  and zero outside the area of openings. Taking only one circular aperture away from the optical axis by  $d$ , for the complex amplitude of the diffraction pattern in the image plane we get the known expression

$$a_{11} = \frac{1}{\lambda^2 pq} \frac{b}{\varrho} J_1(2\pi \varrho b) \exp(i2\pi d\xi), \quad (3.89)$$

where  $J_1$  is Bessel function of the first type and the first order, and

$$\varrho^2 = \xi^2 + \eta^2. \quad (3.90)$$

The last exponential term in the expression Eq. (3.89) is so-called shifting property of the positioning the diffraction aperture outside the optical axis of the lens. In the same way we express the amplitude distribution for the second opening and the resulting pattern, due to mutual interference, is the sum of two expressions

$$a_{12} = \frac{1}{\lambda^2 pq} \frac{b}{\varrho} J_1(2\pi \varrho b) [\exp(i2\pi d\xi) + \exp(-i2\pi d\xi)]. \quad (3.91)$$

The diffraction grating whose amplitude transmittance can be expressed as

$$t_G = C_0 + C_1 \exp(i4\pi d\xi) + C_1 \exp(-i4\pi d\xi), \quad (3.92)$$

where  $c_0, c_1$  are constants, is placed in this plane. The complex amplitude  $a_{12}$  is transferred to  $a_{13}$  after passing the grating

$$\begin{aligned} a_{13}(\xi, \eta) = a_{12} t_G = & C_0 C \exp(i2\pi d\xi) + C_1 C \exp(i2\pi d\xi), \\ & + C_0 C \exp(-i2\pi d\xi) + C_1 C \exp(-i2\pi d\xi), \\ & + C_0 C \exp(i6\pi d\xi) + C_1 C \exp(-i6\pi d\xi), \end{aligned} \quad (3.93)$$

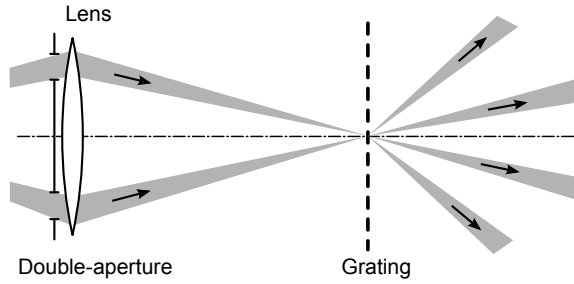


Fig. 3.23. Diffraction of the interference pattern on grating placed in the image plane of the imaging lens with double-aperture diaphragm.

where all the constants of Eq. (3.91) are included in  $C$ . As can be seen, the expression Eq. (3.93) comprises 6 terms, and thus the grid will decompose 6 wavefronts. The wavefront described by the first and the second terms are propagating in the same direction, so it is with the pair of third and fourth term (see Fig 3.23).

The objective lens, which displays an image of the subject on the CCD detector, was focused so that the object plane agreed to the plane of the diffraction grating. Since the different wavefronts propagating behind the grating are angularly splitted, the objective lens captures only the pair corresponding to the first or the second pair of members in the expression (3.93), respectively. Therefore, the following distribution of the intensity appears on the CCD detector

$$a_{13}^* a_{13} = (C_0 C + C_1 C) \exp(i4\pi d\xi). \tag{3.94}$$

The intensities of the records in double exposure measurement are summed

$$I = (C_0 C + C_1 C) \left( \exp \left[ \frac{i4\pi d}{\lambda q} (x_1 + Mx_{01}) \right] + \exp \left[ \frac{i4\pi d}{\lambda q} (x_1 + Mx_{02}) \right] \right), \tag{3.95}$$

where we used the fact that the displacement  $u = x_{01} - x_{02}$  is very small compared to the coordinate of the point in the first  $x_{01}$  and second exposure  $x_{02}$ . After mathematical treatment and rewriting to the trigonometric notation, the expression for the interpretation of interference pattern is obtained

$$I = (C_0 C + C_1 C) 2 \cos \left[ \frac{4\pi d}{\lambda q} (x_1 + Mx_0) \right] \cos^2 \frac{2\pi d}{\lambda q} u. \tag{3.96}$$

The last member of this term expresses searched distribution of the interference fringes, depending on the displacement  $u$ . From the conditions for interference maxima follows

$$u = N \frac{\lambda p}{2d}, \tag{3.97}$$

where  $N$  is order of an interference fringe.

On the basis of that expression, we can assign a value of in-plane displacement in the  $x$  direction to each of interference fringe. Displacements in the  $y$  direction are determined the same way except that the line joining the centers of the diaphragm's openings is oriented in  $y$  axis.

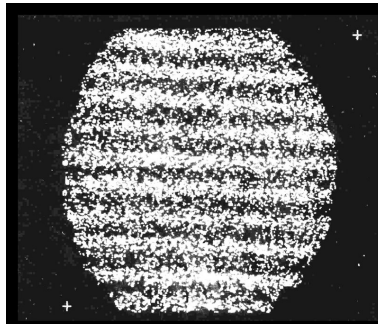


Fig. 3.24. Double-aperture interferogram on the model rotated around the optical axis. Interference fringes are the isolines of constant displacement component perpendicular to the fringes. The weak contrast is caused by the principle of CCD detection.

### 3.4.3 Experimental realization

The optical interferometer assembly with electronic records was created by using conventional optical elements: He-Ne laser, collimator illuminating the object, imaging lens (together with the double-aperture diaphragm represents the principal element of the setup). Focal length of the lens was 140 mm and its best numerical aperture was  $1/2$ . The diameters of the diaphragm openings were 5 mm. For electronic recording and image processing the optoelectronic system TELEMET 2 produced by Tesla Piešťany was used. The CCD camera PTK 0384 was connected to the microcomputer MHB 8080A. The system was equipped with the image record and processing software.

The field of surface displacements was simulated by rotating the whole object around the optical axis. In this case, the isolines of equal displacements in one direction will represent the system of fringes parallel to the connection of centers of the diaphragm openings. The example of interferogram is in Fig. 3.24. The object rotation was measured micromechanically and by using this value the validity of Eq. (3.96) was confirmed.

Contrast of the interferogram in Fig. 3.24 is relatively low. This is the common feature of the methods utilizing electronic image record, which is determined by the recording principle. Therefore, the additional processing needs to use different electronic or digital image filters. System TELEMET was not able to filter noise or enhance contrast, that is the contrast of the final image is weak. However, from the metrological point of view, such a record is definitely usable.

### 3.5 Diffraction of light on the surface microroughness

The roughness of the surface, created by natural or artificial way is an important surface property and has become increasingly important. The surface texture is a key factor affecting the functioning and reliability of a manufactured component. As a rule, the difficulty with traditional methods is that they attempt to detect only surface roughness, by which it is meaning surface height variation, whereas surface texture includes many complex and interrelated surface char-

acteristics.

In recent years, topographical feature and related analysis technology of engineering surfaces have gradually become an important research aspect of machinery and microelectronics engineering. A typical engineering surface consists of a series of spatial frequencies. The high frequency, short wavelength components are linked to roughness, the medium frequency to waviness, and the low to form error (basic profile). It is easy to understand, that different manufacturing process generates different wavelength feature.

The method of objective judgments and evaluation of the most important component of surface structure, roughness, has a long history. At first, a sinusoidal model of unevenness was used, when a chosen quantity was used as an effective (root-mean-square) parameter. Nowadays, the main standard quantities of surface roughness characterization are the arithmetical mean deviation  $R_a$  and the root-mean-square deviation  $R_q$ .

$R_a$  is the mean arithmetical value of absolute deviations of profile within the limits of sampling length:

$$R_a = \frac{1}{l} \int_0^l |y(x)| dx \quad \text{or} \quad R_a \approx \frac{1}{n} \sum_{i=1}^n |y(x_i)|, \quad (3.98)$$

where  $x$  is the abscissa of the profile subtracted on the mean line,  $y(x)$  – the function describing the profile,  $y(x_i)$  – the coordinates of  $n$  points of surface profile within the sampling length,  $i = 1, 2, 3 \dots n$ ,  $l$  – the sampling length,  $n$  – the number of points of surface profile within the sampling length.

At the same time the value  $R_a$  represents the central statistical moment of the 1<sup>st</sup> order,  $\mu_1 = R_a$ . The parameter is geometrically interpreted by the height of the rectangle constructed on the mean line that has the same area as unevenness of profile closed by mean line. The fact that the values of the arithmetic mean deviation of profile  $R_a$  presented in this way does not enable us to determine the shape of surface profile itself; this remains the problem of the whole conception. It concerns namely the height fluctuation of the high-frequency components of the profile structure.

$R_q$  is a quadratic analogy to the parameter  $R_a$  and is defined by prescription:

$$R_q = \sqrt{\frac{1}{l} \int_0^l y^2(x) dx} \quad \text{or} \quad R_q = \sqrt{\frac{1}{n} \sum_{i=1}^n y^2(x_i)}. \quad (3.99)$$

The root mean square deviation of the assessed profile  $R_q$  is at the same time a standard deviation (root-mean-square deviation) of coordinated different points of surface profile. It results from a calculation of the central moment of the 2<sup>nd</sup> order:

$$\mu_2 = \int_{-\infty}^{\infty} (y - m_y)^2 f(y) dy = D_y = \sigma^2; \quad m_y = \int_{-\infty}^{\infty} y f(y) dy, \quad (3.100)$$

where  $m_y$  is the mean value of a stochastic quantity. The usual ratio of the above determined characteristics,  $R_q/R_a$ , falls within the interval from 1.1 to 1.5 and corresponds to changes in the disintegration mechanism resulting from various technologies and it also indicates these changes.

From the viewpoint of topography the same objection as for the above mentioned parameter  $R_a$  is analogically valid for parameter  $R_q$ . The root-mean-square deviation of profile  $R_q$  acquires

significance, however, if the profilometry of the surface is carried out optically. It is assigned by the fact that the majority of optical signals are based on detection of intensity, which is a quadratic value of its amplitude.

Non-standard parameters of surface profile serve to provide a more complex view of topographical structure and thus integrally complement data prescribed by standard. The arithmetic mean wavelength of the profile  $\lambda_a$ , which is a  $2\pi$  multiple of the ratio of the arithmetic mean deviation of the profile  $R_a$  and the mean value of the profile slope:

$$\lambda_a = 2\pi \frac{R_a}{\Delta a}, \quad (3.101)$$

where  $\Delta a$  is the mean angle of the slope of unevenness.

The autocorrelation function  $R_{yy}$  expresses the degree of periodicity, or rather the randomness of the profile, and it is defined by the relationship:

$$R_{yy}(x) = \frac{1}{N-x} \sum_{i=1}^{N-x} (y_i - m_y)x_i(y_i - m_y)(x_i - x). \quad (3.102)$$

The value  $R_{yy}(0)$  represents the dispersion  $R_{yy}(0) = D_y$ . For the evaluation of the proper profile curve of the surface itself, the so-called standard autocorrelation function is used:

$$r_{yy} = \frac{R_{yy}(x)}{D_y}. \quad (3.103)$$

For many years, information about the surface microprofile has been acquired by mechanical contacting of the surface with a sharp tip, whose tip curvature is such, that it can penetrate the detailed profile geometry.

The light scattering is a sensitive function of its roughness. Part of the light is diffusely reflected (scattered) into directions different from the specular reflection direction for an ideally smooth surface. Roughness features, that produce light scattering, are typically separated by distances from hundreds of nanometers to fractions of millimetres. Larger separations of surface features, which are the so called surface waviness, contribute only to the near-angle scattering, and its separation on the background of large angle scattering diagram is troublesome, or even impossible. On the contrary, microroughness generally scatters light into very large angles and decreases the amount of light that is detected by an optical sensor. From this point of view, generally, the surface feature heights can be classified according to their ratio with the light wavelength  $\lambda$  in the visible region. In principle, such measuring instruments are limited to measure heights less than half of light wavelength, that is even nanometer scale heights can be evaluated. Such surfaces are conveniently inspected with well established techniques, based conceptually on the measurement of total integrated scattering or angle-resolved scattering. However, these approaches, based on scalar diffraction theory, do not take into account the lateral texture of the surface and belong to integrated principles of operation, where only integral information about surface heights variations, generally expressed as the root-mean-square roughness, is obtained. In addition, the interpretation of the results measured needs certain assumptions about the nature of the surface profile, for example, besides the condition  $\text{rms} \ll \lambda$ , lateral dimensions of the surface feature must be  $\gg \lambda$  and the surface structure has to be isotropic or unidirectional. Probably the most stringent limitation is the demand for Gaussian statistics of the measured surface structure, hence the "natural" surfaces as a rule fulfill these conditions. As the most of the artificially

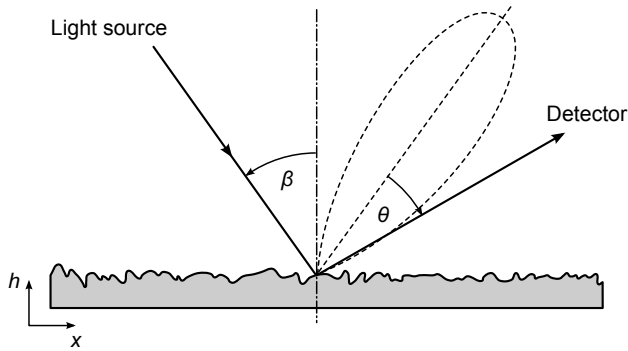


Fig. 3.25. Diffraction of light on the surface roughness.  $\beta$  is the angle of incidence,  $\theta$  is the detection angle. The dashed-line scattering diagram shows the random character of light reflection from rough microstructured surface.

formed surfaces are inherently deterministic, in engineering practice, correction factors must be used to obtain the true values of surface rms.

The light scattering method shall be used in a variant where the more complete information about the reflected light distribution is recorded. A theoretical derivation based on Huygens-Fresnel principle, Fraunhofer approximation, and Wiener-Khinchine theorem shows that the Fourier transform of a scattered field is approximately proportional to the autocorrelation function of the surface profile for optically smooth surfaces. This means that the important parameter, surface correlation length, may be simply evaluated.

When the light wave is incident on a solid surface, it is reflected either specularly or diffusely or both. Reflection is specular when the angle of reflection is equal to the angle of incidence which is attribute of mirror-like smooth surfaces. Reflection is diffuse when the energy of reflected wave is scattered into half space. Generally, the roughness of surfaces covers a wide range of both lateral and heights dimensions from fine grained to rough waved. As roughness increases, the intensity of specular beam decreases while the diffracted radiation increases in intensity and becomes more diffuse. The relationship between the light wavelength and the surface roughness affects the physics of reflection. The classification of surfaces by their prevailing surface spatial wavelengths (which means the characteristic lateral as well as height dimensions) can be done.

We are inspecting the surface with a profile described by the function  $h(x, y) \in \langle h_{\min}, h_{\max} \rangle$ . The mean value of  $h(x, y)$  is  $h_0$  and the statistical quantity  $\sigma$  is the square-root of variance or in other words standard deviation. For the sake of simplicity we will assume only 1D situation. Illuminating the rough surface by a plane wave as it is sketched in Fig. 3.25 the phase of the light wave  $\varphi(x)$  due to roughness profile can be expressed as follows [43]:

$$\varphi(x) = \frac{2\pi}{\lambda}(1 + \cos \beta)h(x), \tag{3.104}$$

where  $\lambda$  is the wavelength of light and  $\beta$  is the angle of incidence where also the assumption about both sufficiently smooth surface and small surface slopes was applied. Let us consider

$a_I$  as the amplitude of planar incidence wave. Provided that the illuminated area is in lateral dimension large enough, the complex amplitude of the light wave immediately after its reflection from the surface can be expressed as a complex function

$$a_R(x) = a_{I}r \exp \left[ i \frac{2\pi}{\lambda} (1 + \cos \beta) h(x) \right], \quad (3.105)$$

where  $r$  is the average reflectivity of the surface. We define microroughness of the surface as a roughness profile with height variations smaller or compared with wavelength of light. In reality the variations do not exceed several  $\mu\text{m}$ . In such a case the phase factor in Eq. (3.105) can be expanded into series

$$\exp \left[ i \frac{2\pi}{\lambda} (1 + \cos \beta) h(x) \right] \approx 1 + i \frac{2\pi}{\lambda} (1 + \cos \beta) h(x). \quad (3.106)$$

As known [43] in the position far enough from the observed surface, the complex light field can be expressed as a Fourier transform of the amplitude  $a_R(x)$

$$A(\xi) = \int_{-\infty}^{\infty} a_{I}r \left[ 1 + i \frac{2\pi}{\lambda} (1 + \cos \beta) h(x) \right] \exp(-i 2\pi x \xi) dx, \quad (3.107)$$

where  $\xi$  is the spatial frequency. Spatial frequency is a magnitude related to the lateral coordinate in the observation plane normal to the direction of mirror-like reflection from the surface

$$\xi = \frac{u}{L\lambda} = \frac{\sin \theta}{\lambda}. \quad (3.108)$$

In this relationship  $L$  is the distance of observation plane and  $\theta$  is the observation angle from the grazing direction.

The integral of Eq. (3.107) can be simply divided into two components, where the former component presents zero diffraction order and characterizes in fact an aperture function of beam illuminated area. In the case of finite sized specimen (or more precisely, finite illuminated area) this component could define diffraction on such sized obstacle. On the contrary, when the lateral dimensions of illuminated area are much larger compared to the light wavelengths or mean feature of the surface roughness it presents only intensity contribution into the grazing angle direction. In the case of circular illuminated area Airy's disc distribution it can be written for the intensity

$$I(\varrho) = C \left( \frac{d}{2} \right)^2 \frac{2J_1(\pi d \varrho)}{d \varrho}, \quad (3.109)$$

where  $\varrho^2 = \xi^2 + \eta^2$  and  $d$  is the diameter of the diffraction aperture and  $J_1$  is Bessel function of the first kind, order one. In practice, as a rule, the inspected surface area is illuminated by TEM<sub>00</sub> laser beam. The energy distribution in this case is characteristic by radially transversal Gaussian distribution

$$I(\varrho) = I_0 \left[ \frac{W_0}{W(z)} \right]^2 \exp \left[ -\frac{2\varrho^2}{W^2(z)} \right], \quad (3.110)$$

where  $I_0$  is the maximum irradiance and  $W(z)$  the radius at the  $I_0/e^2$  point. The beam waist  $W_0$  and far-field half-angle divergence is a constant which defines “diffraction limited” minimum size of beam radius

$$W_0 \approx \frac{8\lambda f}{\pi D}, \quad (3.111)$$

where  $f/D$  is F-number of the focusing lens.

Nevertheless, while the aperture function  $a_I$  may not be taken into account when dealing with the analysis of surface roughness parameters, it defines the statistical average of the size of individual speckle in diffraction halo. Consequently, we are interested in the second part of integral (3.107)

$$A(\xi) = C(1 + \cos \beta) \int_{-\infty}^{\infty} h(x) \exp(-i2\pi x\xi) dx = c(1 + \cos \beta)H(\xi), \quad (3.112)$$

where  $C$  is the arbitrary constant and  $H(\xi)$  is the Fourier transform of the function  $h(x)$ . When dealing with surface roughness, statistical averaging needs the dimensions of the illuminated area to be much larger than the dimensions of the surface grains, that is why we have omitted the first term of Eq. (3.107). Light intensity distribution around the direction of mirror-like reflection, which is diffraction halo on the observation plane, is expressed as a square of complex amplitude absolute value

$$I(\xi) = A^*(\xi)A(\xi) = |C(1 + \cos \beta)H(\xi)|^2. \quad (3.113)$$

Usually,  $|H(\xi)|^2$  is denoted as the power spectral density. Eq. (3.113) indicates that a scattered far field distribution is proportional to the power spectral density function of the light wave immediately in front of surface. According to Wiener-Khintchine theorem, the autocorrelation function  $c_f(p, q)$  of the complex amplitude  $a_R(x)$  is the inverse Fourier transform of the power spectral density function  $|H(\xi)|^2$ . Quantities  $p, q$  are the lag lengths of the autocorrelation function. Thus, the Fourier transform of a scattered far field maps the autocorrelation function of the complex amplitude immediately after reflection on surface. Now we will consider another assumption with regard to statistical properties of the surface profile. Let the function of height variations  $h(x)$  have its autocorrelation function in Gaussian form:

$$\int_{-\infty}^{\infty} h^*(x')h(x' + x) dx' = K \exp(-x^2/l_c^2), \quad (3.114)$$

where  $l_c$  is the correlation length and  $K$  is the real constant. We have searched the Fourier transform of the autocorrelation function

$$\int_{-\infty}^{\infty} K \exp(-x^2/l_c^2) \exp(-2\pi i x\xi) dx = Kl_c \exp(\pi^2 l_c^2 \xi^2) = |H(\xi)|^2. \quad (3.115)$$

Now, by substitution of Eq. (3.115) and Eq. (3.112) into Eq. (3.113), we obtain an analytical expression for scattered light intensity in the direction of observation  $\theta$ :

$$I(\theta) \sim \frac{l_c}{\lambda} (1 + \cos \beta)^2 \exp[-(\pi l_c/\lambda)^2 \sin^2 \theta]. \quad (3.116)$$

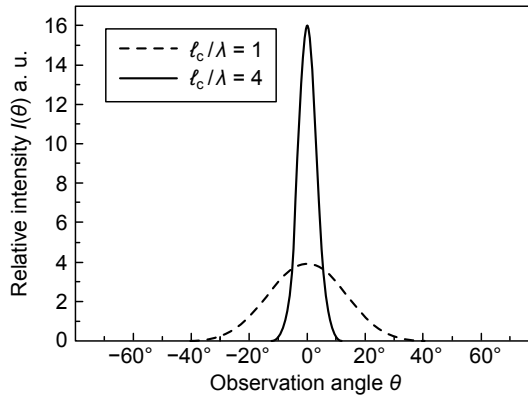


Fig. 3.26. Angle distribution of light intensity by diffraction on rough surface with Gaussian statistics of microroughness with correlation length  $l_c$ . As expected, the larger values of  $l_c$  compared to the wavelength  $\lambda$ , the narrower is the intensity distribution.

Provided that the angle of observation is small i.e.  $\theta \ll 1$  and  $\sin \theta \doteq \theta$  we have the simplified relationship

$$I(\theta) \sim \frac{l_c}{\lambda} (1 + \cos \beta)^2 \exp [-(\pi l_c / \lambda)^2 \theta^2]. \quad (3.117)$$

As seen, an important parameter of this function is the ratio  $l_c/\lambda$ . The graphic representation of the function Eq. (3.117) for two different values of this parameter and  $\beta = 0$  is shown in Fig. 3.26. As it can be seen, for large correlation lengths bell-like curve is quickly narrowed and peak tends to clear mirror-like reflection. This tendency is also illustrated by scattering diagram which is in fact parametrical formulation of the function Eq. (3.117) in polar coordinates and represents geometrical interpretation of graphs in Fig. 3.26. For better view in this Figure the angle of illumination/mirror-like reflection was chosen  $\beta = 45^\circ$ .

The assumption of Gaussian form of autocorrelation function follows from the fact, that autocorrelation function of “proper” random function shows expressive central maximum and in its vicinity the Gaussian function can be used as the first approximation. Then, the correlation length  $l_c$  is defined as a value on  $x$ -axis, where the autocorrelation function has a value of  $1/e$  of its maximum in the central point  $x = 0$

$$c_f = \exp \left( -\frac{R_q^2}{l_c^2} \right). \quad (3.118)$$

Thus, the horizontal property of one-dimensional surface profile may be characterized by surface correlation length which is a characteristic feature size of surface profile for in-plane dimensions.

Assuming the surface height distribution as a Gaussian random process the standard deviation of roughness  $R_q$  as defined by Eq. (3.99) can be determined, too

$$\psi(h) = \frac{1}{R_q \sqrt{2\pi}} \exp \left[ -\frac{(h - h_0)^2}{2R_q^2} \right], \quad (3.119)$$

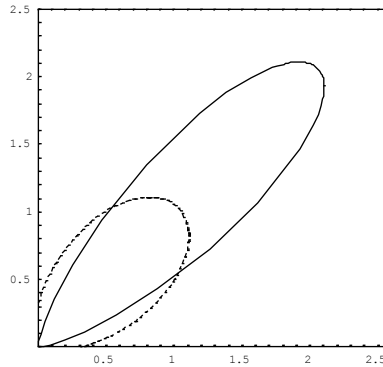


Fig. 3.27. Scattering diagram of the diffracted light from rough surface with Gaussian statistics of microroughness with coherence lengths as in Fig. 3.26.

where  $\psi(h)$  is probability density function. For the sake of simplicity, we consider one of both lateral directions. Using relation for the probability density function

$$\psi(h) = \frac{dx}{dh}, \tag{3.120}$$

the variables of the integral in Eq. (3.112) can be changed

$$a_S = C \int_h \psi(h) \exp\left(-\frac{i4\pi}{\lambda}h\right) dh. \tag{3.121}$$

Now, the amount of the light scattered from the rough surface to the direction of mirror-like reflection can be determined. Then, the values of spatial frequencies approach to zero for both the perpendicular illumination as well as for oblique illumination.

The amplitude of the light reflected from the ideally smooth and flat surface  $h(x, y) = 0$  is a constant

$$a_0 = C \int_h \psi(h)dh = C \tag{3.122}$$

due to unity of the probability integral Eq. (3.120). Then, in the direction of mirror-like reflection, the ratio of the amplitudes of the light scattered on the diffuse surface and on the mirror-smoothed surface is the integral of Eq. (3.121). After the substitution of the probability density function Eq. (3.119) we have

$$R = \frac{I_S}{I_O} = \exp\left(-\frac{4\pi^2}{\lambda^2}R_q^2\right), \tag{3.123}$$

where  $I_S$ , and  $I_O$  are the intensity of integral value of the light scattered on the surface roughness and the light reflected in the centre of diffraction halo. This expression can be used for evaluating the value  $R_q$  by simple measurement of total amount of the light scattered in diffraction diagram and the part from its central region.

It has to be noted that surface profiles having the same variance  $R_q$  may have quite different correlation lengths  $l_c$ . This property of the profile is expressed in the shape of the autocorrelation function by stronger or weaker correlation moments between the profile ordinates.

Eq. (3.123) is the relation between the roughness of the metallic surface and the intensity in the centre of diffraction halo. Since the stress induced roughness is related to the value of effective strains, the ratio  $R$  can be used as a quantitative measure for the assessment of the plastic strains/stresses.

### 3.6 Evaluation of elasto-plastic stresses by surface spectrum analysis

The standard procedure of the measurement of elasto-plastic stresses in metals based on strain gages or moire often has a weak points. This is due to technical difficulties with the large strain measurement, more complicated material response and also anisotropy of plastic behaviour. It is known that increased plastic deformation of metals is followed by corresponding enhancement of the surface roughness. A number of authors have tried to give quantitative interpretation of this effect. Yamaguchi and Mellor [44] and Lee et al. [45] have shown the dependence of the induced surface roughness on the effective strain. Hence, by measurement of surface roughness changes the plastic zone contours could be identified. Moreover, Azuchima and Miyagawa [46] and Dai and Chiang [47] have established proportionality between plastic strains and the width of intensity spectrum of the light scattered from induced surface roughness.

Most of authors refer to applications of the method of correlation analysis of the changes in the diffraction microstructure of light field and quantities such as spectrum width, contrast, correlation coefficient or amount of widely scattered light have been used to quantify this effect. Well established is the relation effective plastic strain vs. intensity level of the speckle image relative to that of undeformed surface or speckle pattern decorrelation. [45, 48] A linear relationship for surface roughness and effective strains was observed when the von Mises yield criterion in the elasto-plasticity region was used.

The measurement of plastic deformation and plastic zone around a sharp notch or a crack in the metal is required not only to study the mechanism of fracture but, also, for design and failure analysis of a machine. The change in microstructural morphology of the surface often indicates the presence of irreversible plastic strains. As the elasto-plastic stress state around the crack tip in a steel material can be numerically computed on the basis of known material loading diagrams, the experimental results of the optical method of far speckle field observation can be confronted for. However, up to now a little effort has been done to explain the plastic strain/stress orthogonal components distribution at defined stress state.

#### 3.6.1 Experimental results

The optical diffraction evaluation was used to measure the samples of notched steel beams. The crack, whose plastic zone at the tip was to be measured, was simulated by a 0.2 mm wide and 17.5 mm long saw cut in the middle of the span. The beam with dimensions of  $180 \times 35 \times 3.6 \text{ mm}^3$  was made of high-strength, stainless steel. The observed plastic area at the position of crack tip was created by applying of load up to 3 000 N by three-point bending with a 140 mm span of force action. The material parameters were obtained by a standard tensile test. Elasto-

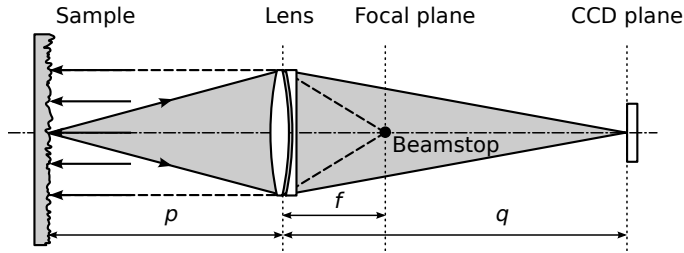


Fig. 3.28. Optical scheme of measurement of diffraction properties of microstructured surface. The beamstop serves as spatial filter eliminating specularly reflected light. Only diffracted and scattered rays are imaged by the lens on CCD.

plastic behaviour of the material is fitted by power law strain hardening constitutive model

$$\varepsilon_{ij}^0 = \frac{3}{2} \frac{\varepsilon^0}{\sigma} s_{ij}, \quad \varepsilon_0 = \varepsilon_r (\sigma / \sigma_r)^n, \quad (3.124)$$

where

$$\begin{aligned} \sigma &= \sqrt{\frac{3}{2} s_{ij} s_{ij}}, \\ \varepsilon^0 &= \sqrt{\frac{3}{2} \varepsilon_{ij}^0 \varepsilon_{ij}^0}, \\ s_{ij} &= \sigma_{ij} - \delta_{ij} \frac{\sigma_{kk}}{3}. \end{aligned}$$

In the above  $s_{ij}$  is the deviatoric part of the stress,  $\sigma_{ij}$  is the reference strain at some reference stress level  $\sigma_r$  and  $n$  is the index of power law (Ramberg-Osgood). The values  $\varepsilon_r$  (for a given value of  $\sigma_r$ ) and  $n$  are 0.015 and 9.1, respectively. Other basic material parameters are: Young modulus  $E = 2.08 \times 10^5$  MPa, Poisson ratio  $\nu = 0.3$  and yield stress  $\sigma_r = 280$  MPa.

The important condition of the correct results on measured roughness induced by elasto-plastic strains is a metallic surface finished by grinding and polishing before loading of the sample. The polishing does not require to be too high; in the case of rolled surfaces, a moderate mirror-like surface is sufficient.

In measurement of diffraction properties of the studied surface microstructure the specimen was illuminated nearly perpendicularly to the rough surface with a laser beam in a simple scheme of optical filtration (Fig. 3.28).

The monochromatic light of the He-Ne CW laser with an output power of 15 mW was collimated into the diameter of  $\varnothing = 20$  mm and directed onto area around crack tip. Long focal distance lens projects the surface image into the CCD chip of digital camera (Cannon EOS 300D). The area of plastic zone is identified by inserting the iris diaphragm as a low pass binary filter into the focal plane of the filtering lens. Figure 3.29 illustrates a filtered image of the area where the higher spatial frequencies are blocked. Identification of the zone with plastic deformations is well-marked, nevertheless, the interpretation of the zone boundaries is somewhat complicated.

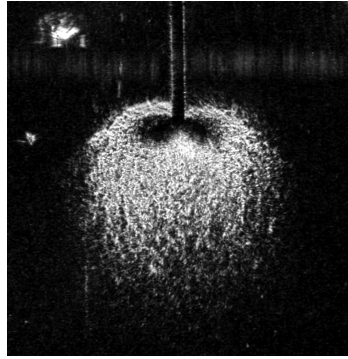


Fig. 3.29. Filtered image of the plastic zone near the notch in steel polished beam with the higher spatial frequencies blocked. The plastic zone around the notch tip can be clearly identified due to deformation induced local roughening of the polished metal surface [49].

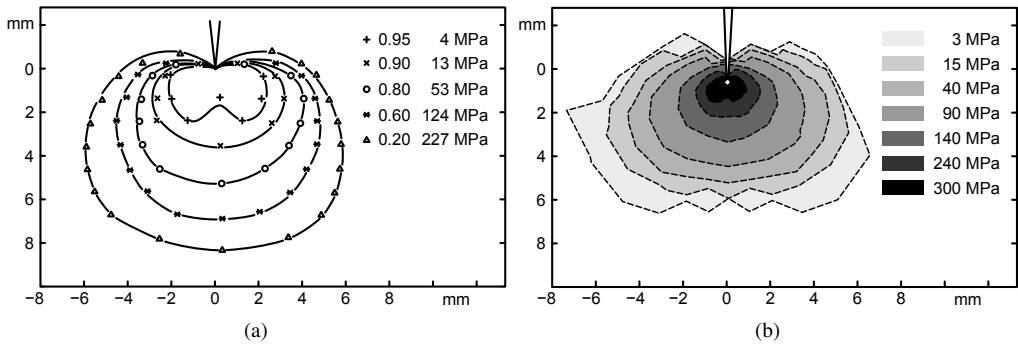


Fig. 3.30. Comparing the experimentally obtained values of principal stresses in plastic zone around the crack tip to the simulation by ANSYS [49].

The flatness of the mirror-like area is often affected by mutual inclination of parts of this area and the optical filtration makes difficulties. Then the amount of the scattered light can be quantified separately for each part of the plastic zone area by scanning the specimen point by point with narrow beam. Long focal lens concentrated the laser beam into the circular spot of 0.3 to 0.5 mm where it undergoes scattering on the surface. As the evaluation procedure is based on Eq. (3.123), only the intensity in the centre of diffraction halo was measured directly by photodiode detector. The read value of intensity was then normalized to the value of intensity observed on the reflection from the part of beam surface not damaged by plastic stress. To separate specularly reflected light, the photodiode effective area was screened by a diaphragm opening of  $\varnothing = 4.0\text{mm}$  in diameter which is diffraction angle of about  $0.5^\circ$ . The rays passed through are the rays within the diffraction limit for appropriate distance of observation.

Fig. 3.30 shows the curves with equal amount of scattered light from the area within the plastic zone around the crack tip. The curves plotted were obtained as fits of the measured

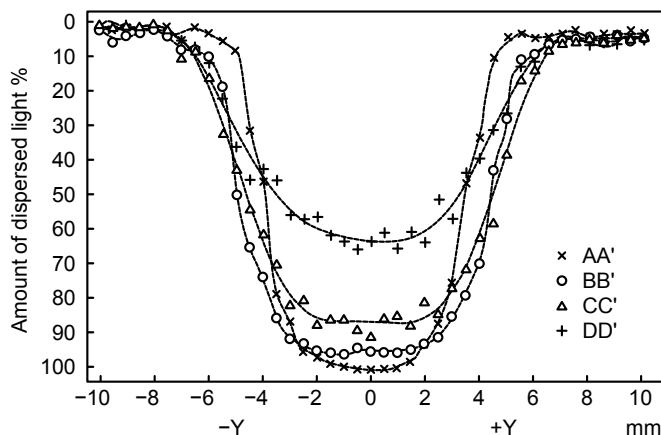


Fig. 3.31. Amount of dispersed light in several horizontal sections of the plastic zone.

points by the least squares method for the amounts of the dispersed light 95 %, 90 %, 80 %, 60 % and 20 % of the value specularly reflected from undamaged mirror-like area. Provided that we assume Gaussian height distribution of the roughness profile induced by plastic stress, the plotted curves present equal values of  $R_q$  (see Eq. (3.123)). In the figure the smooth character of the iso-curves is clearly visible in spite of some statistical dispersion of the measured data points. This is also demonstration of the obvious relation between the acting stress and the measure of surface damaging.

In order to verify the plastic strain determination method, a numerical simulation of the plastic stresses distribution around crack tip was performed by ANSYS SW [50]. In Fig. 3.30b the computed values of von Mises stresses are drawn. The results can be directly compared with those obtained on a calibration specimen for the evaluation of strains. In the calibration experiment, steel specimens were uniaxially loaded on a testing machine to the level of plastic deformation and the scattered field was recorded step by step. The actual strains were measured by testing machine. The acquired diffraction response of the rough specimen surfaces were coupled with the values of one-axis tension strains which can be interpreted as von Mises effective strains. It has to be noted that the numerical analyses were performed as a two-dimensional. For the thickness of the specimen of 3.6 mm the plane stress conditions are valid to the distance of about 1.0 mm to 1.5 mm from the crack tip, the near vicinity is affected by three-dimensionality of stress distribution. This is visible also from experimentally obtained roughness distribution in the vicinity of crack tip (Fig. 3.30a) where the shape of effective strain iso-curve is immediately related through von Mises criterion to 3-D stress state. Inside this zone the butterfly-like shape characteristic of plane strain conditions is visible.

Fig. 3.31 gives another representation of the results. The dependences of dispersed light found while scanning the elasto-plastic area in several horizontal sections (perpendicularly to crack path) are shown there. Sudden fall on the curves defines the boundaries of the plastic zone area. The mapping method was also tested by using the dynamic scanning of the plastic zone area by uniform motion of the illuminated spot on the rough surface. The signal on light intensity

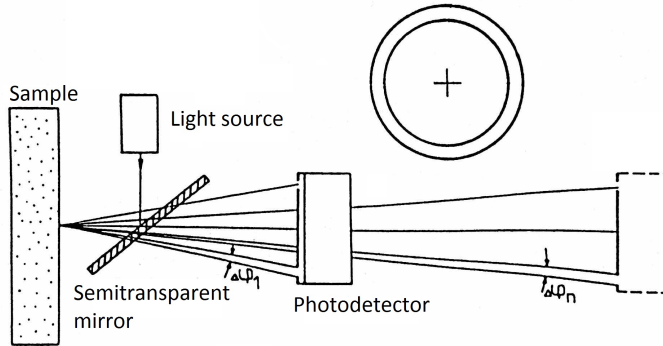


Fig. 3.32. Z-scanning diffraction halo measurement.

from the centre of diffraction halo was recorded by digital oscilloscope Trace 8086.

### 3.6.2 Separation of the principal strains

Another way to obtain more detailed information on the diffusion spreading of the sample surface is the transversal scanning of the speckle field – diffraction halo, with a suitable optical point-like detector. However, this method abounds in technical difficulties. The photoelectric signal obtained varies in a large range of intensity values up to  $10^3$ – $10^5$  and the measurement itself is sensitive to non-homogeneities in the diffraction field. These drawbacks can be eliminated by scanning the diffraction halo in line of sight direction – z-scanning (Fig. 3.32). Planary photodetector – two large effective area photodiodes were screened by the diaphragm shaped as two  $\pm 10^\circ$  annular sectors. By moving the photodetector along the optical axis, the light at the diffraction angles from  $1^\circ$  to  $20^\circ$  may be collected. The range of photoelectric signal is relatively narrow and the angular intensity distribution is obtained simply and the power spectrum is easily calculated. The angular distribution of the diffracted light was measured in this manner at several tenths of points on the specimen surface around the crack tip.

One of the characteristic phenomena observed at this scheme was the expressive directional anisotropy of the diffraction halo. The diffraction divergency in the x-axis in the crack direction line was lower than that in the y-axis. This arises from the surface roughness defects being distinctly elongated in shape with their longer dimensions oriented in the makro-crack line direction. In points out of crack path half-axes of the intensity distribution elliptical shape are inclined (Fig. 3.33). Considering the induced surface roughness governed by Gaussian distribution, the correlation lengths can be evaluated using Eq. (3.123).

Determination of the parameters such as speckle contrast, spectrum width or stress-induced surface roughness Eq. (3.119) together with the appropriate experimental calibration enables effective plastic strains to be evaluated quantitatively. The plastic strains evaluation is usually based on a condition defined by von Mises for the equivalent stress. However, the complete stress analysis (at least plane stress or plane strain state) to be carried out needs to know the absolute values of the orthogonal principal strain/stress components. The light scattered from the metallic

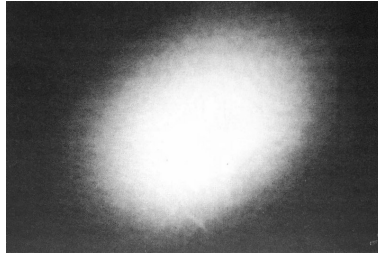


Fig. 3.33. Elliptical diffraction halo visualises directional anisotropy of surface microroughness. The surface roughness defects are elongated in the crack line direction [51].

surface with stress-induced roughness includes also information about the orientations of surface micro-unevennesses related to the orientations of stresses. When the surface inside the plastic zone is illuminated by quasi point-like spot, the elliptical shape of the diffraction halo is clearly visible. The size and orientation of the ellipse varies point by point on the scanned elastoplastic region. For simplicity we will assume the grains in a surface layer statistically as spherically shaped. These spheroids are deformed into ellipsoidal shape under the action of stresses. This is usual assumption in the method of microscopical measurement of the grains shape as well as in the method of plastic strains evaluation using technique of printed surface circular grids. Actually, empirical experience with metallic surface plastic deformation confirms that the micro-deformations on the base of the order of grain sizes is governed by normal law of distribution. Therefore, the evaluation of elasto-plastic strains has to be realized by detecting the in-plane displacements that is the microscopic changes in lateral direction.

Gaussian height distribution or standard deviation  $R_q$  cannot distinguish the surfaces with different correlation lengths. For isotropic surfaces the correlation length is independent of direction along the surface and can be evaluated by Eq. (3.123). Elliptical directional anisotropy of the diffraction halo (see Fig. 3.33) indicates power spectrum of anisotropic surface with the correlation length dependent on direction along the surface. A correlation function might then be written

$$c_f(x, y) = \exp \left[ - \left( \frac{x^2}{l_x^2} + \frac{y^2}{l_y^2} \right) \right], \quad (3.125)$$

where  $l_x$  and  $l_y$  are the correlation lengths in the  $x$  and  $y$  directions, respectively. Then the power spectrum for such surface with a Gaussian correlation function takes the form [52]

$$|H(\xi, \eta)|^2 = \frac{1}{4\pi} R_q^2 l_x l_y \exp(-\xi^2 l_x^2 / 4) \exp(-\eta^2 l_y^2 / 4). \quad (3.126)$$

Classic plasticity theory provides the equations with three stresses and three strains in the principal directions taking into account von Mises yield criterion and isotropic hardening. On the surface free of load, where strains are measured, the stress perpendicular to the surface  $\sigma_3 = 0$ . At a given point, the directions of the principal normal stresses  $\sigma_1$  and  $\sigma_2$  lie in a plane tangential to the surface. For a plane stress condition where  $\sigma_3 = 0$  the equivalent stress  $\sigma_\nu$  can

be expressed as follows

$$\sigma_\nu^2 = \sigma_1^2 + \sigma_2^2 - \sigma_1\sigma_2. \quad (3.127)$$

Since Hooke's equations represent a linear relationship between stresses and deformations, the equivalent strain  $\varepsilon_\nu$  can be determined directly from the principal strains. Thus, for the equivalent strain

$$\varepsilon_\nu = \frac{1}{1+\nu} (\varepsilon_1^2 + \varepsilon_2^2 + \varepsilon_3^2 - \varepsilon_1\varepsilon_3 - \varepsilon_2\varepsilon_3)^{1/2}, \quad (3.128)$$

where  $\nu$  is Poisson's ratio. The strain  $\varepsilon_3$  can be eliminated on the surface and we obtain

$$\varepsilon_3 = -\frac{1}{1-\nu}(\varepsilon_1 + \varepsilon_2). \quad (3.129)$$

Keil and Benning derived the relationship between the equivalent strain  $\varepsilon_\nu$  and the principal strains  $\varepsilon_1, \varepsilon_2$  [53]:

$$\varepsilon_\nu = [N_q (\varepsilon_1^2 + \varepsilon_2^2) + N_g \varepsilon_1 \varepsilon_2]^{1/2}. \quad (3.130)$$

In this expression  $N_q$  and  $N_g$  are functions of Poisson's ratio only, with constant  $\nu$  the  $N_q$  and  $N_g$  are the material parameters. For constant equivalent strain,  $\varepsilon_\nu$  is constant and Eq. (3.130) represents an ellipse. According to von Mises theory, if equivalent stress exceeds a certain material dependent limit, elasto-plastic strains occur. Elasto-plastic material response obtained by uniaxial tension test can be formally described in the same way as the linear elastic material.

#### **4 Laser and optical measurement techniques for testing in microelectronics**

At the designing process of integrated electronic circuitry, packaging of small structures and namely the micro/nano-electronic mechanical systems (M/NEMS) device structures the knowledge of structural mechanical properties are often essential to the right weighting of all the mechanical proposal aspects. Nowadays, the development and fabrication of such structures has been realized not only by using conventional well established procedures and known material parameters. Increasing design and performance demands in the near future will require more exact and complete information considering both the mechanical and thermo-mechanical materials properties and their mutual interaction in multilayer system. Acquisition of these data is made challenging by the small dimensions involved, mechanical test methods designed for bulk materials are generally not suitable for direct applications to thin film materials, and thin film are known to exhibit properties unlike their bulk counterparts. Nonetheless, the mechanical properties required for accurate prediction of device performance as well as for proper numerical modeling of the whole system, must be based on reliable, accurate tests. Although many of tools for such a purpose are now established, the fundamentals of mechanical characterization continue to be identified while there is growing need for methods allowing to measure both the material and structural element properties.

Laser based metrology in microelectronic technologies owes application in the field mainly to its specific features, particularly to the contactless and non-invasive way of working. Various forms of nondestructive, noncontact inspection techniques have been proposed in order to make possible the evaluating of microelectronic device shapes, their defects and stress induced deformations, surface roughness, as well as thermal and intrinsic residual stresses, material parameters, and also dynamic performances of MEMS structures. The inherent contactless nature of most of the optical measuring principles predestines many of them to be installed as an apparatus to perform in-situ measurements inside the vacuum chamber, or in other demanding ambient conditions. To test the wafers, structures and devices, the interferometrical principles are commonly used, however, the exploitation of photoelectric detecting and CCD camera observation enlarges province to phase shift, white light and scanning interferometry, but also to qualitative improvements of classical principles, such as the phase visualization, the Foucault knife or the confocal focusing. Several methods mentioned above have been applied to inspect the surface flatness and roughness of silicon (or GaAs) wafers, to evaluate thin film and membrane residual stresses and to measure both the static and dynamic mechanical characteristics of MEMS microcomponents.

##### **4.1 Specular and diffuse-like reflected surface flatness testing**

Flatness of upper polished side of silicone (or GaAs based) wafers is one of the vital factors, affecting the reliability of semiconductor device patterns structured by lithography. It can be characterized as the total indicator reading, or focal plane deviation, describing the distance of points on the top wafer surface to a plane, fitted to this surface. The reasons for such a surface waviness can be various. For example, the presence of residual stresses, which is often the case after mechanical treatment – polishing of the top wafer surface, can deform the overall shape of the wafer. Mostly, this global wafer deformation has an anisotropic nature, resulting from usual orthotropy of main mechanical parameters along the crystallographic axes. The demand

for precise image sharpening at the photolithographic pattern projection needs to know the values of surface height variations, particularly when we are dealing with high density circuits. It can be said that mainly geometrical profile parameters of the virgin polished surface determine the wafer quality with regard to its printability by lithography.

In principle, the measurement of small deviations of specular wafer surfaces can be accomplished by several optical methods. From the point of view of classical optics, handling with optically smooth surfaces is a well established metrological task. Therefore, there are many semiconductor device producers, that are equipped for inspection of wafer flatness and roughness with a commercially available testing apparatus.

In spite of that, the commercial, as a rule automated systems are aimed to solve a limited class of problems and not always can satisfy the specific and varying requirements, encountered often in research laboratories and designing teams. On account of that, the comparative analysis has been performed to evaluate several optical techniques, their possibilities, effectiveness, as well as limitations.

The surfaces of wafers are often tested by using the arrangement of laser white-field or standard laser interferometry [54]. With regard to wafer measurement, a common drawback of these interferometers is their sensitivity, frequently even out of proportion for the testing of relatively strongly deviating wafer surfaces. Consequently, there is an effort to install oblique incidence interferometry [55]. However, the large diameters of the substrates, nowadays usually 150 mm and more, need to have large precise optical elements, such as mirrors, prisms and collimators.

The comparative principle of holographic interferometry eliminates the necessity of precise large field of view optics that is why the real-time method of holographic interferometry has been tested. As known, the method is mutual interference of the etalon wave, reconstructed from the hologram, with that reflected off the real wafer surface. The reference hologram wavefront was created by recording of the hologram of flat mirror. If necessary, also the reference hologram of actual wafer surface is recorded and afterwards, the mutual comparison of both the initially not ideally flat surface and the surface after forced deformation, respectively, can be done.

Provided that at the hologram reconstruction we have used the wavefront identical to the reference wavefront at the etalon hologram recording, we can describe the intensity of interference with object wavefront as follows [42]

$$I = I_0 + 2|a|^2 \cos(\varphi_0 - \varphi_1), \quad (4.1)$$

where, for simplicity, the equal intensities of both the reconstructed and object waves are assumed. In Eq. (4.1),  $I_0$  is the light intensity of the zero order diffraction at the reconstruction,  $|a|$  is the modulus of complex amplitude, and  $\varphi_0 - \varphi_1$  is the phase difference between the wavefront, reflected from the wafer surface, and the wavefront, reconstructed from the etalon hologram. In general case, we have the resulting interference field in the form of reconstructed image of the object, which is covered by macroscopic interference pattern of dark and bright fringes. Argument in Eq. (4.1) characterizes the difference between the etalon and the tested surface. Phase, and consequently path difference depend on the geometry of the optical setup, by which the paths of both illuminating and reflected rays are specified. In the case of mirror-like reflection, for oblique incidence of parallel rays onto the specimen surface at an angle  $\alpha$  we have

$$w = \frac{N\lambda}{2 \cos \alpha}, \quad (4.2)$$



Fig. 4.1. Interference contours of silicon wafer surface deformation.

where  $w$  is the deflection of wafer,  $\lambda$  is the wavelength of light and  $N$  is the interference order of the fringes. In the experiments, the angle of  $\alpha = 27^\circ$  was adjusted, thus the height difference between two neighboring fringes was  $0.355 \mu\text{m}$ . The holographic record of the flat mirror surface was taken on AGFA-Gevaert 10 E 75 photo plates. Precise positioning of the etalon hologram after its developing was performed precisely to the original position by means of special 3D axes adjustable holder with micrometric screws. Adjusted hologram positioning is considerably simplified with regard to mirror-like character of wafer surface, where laser speckles are not present and lateral shifts are not critical. Also the accurate parallelity of both the collimated beams need not to be kept, even the spherical wavefronts from point-like pinholes give acceptable conditions for etalon hologram adjustment. Fig. 4.1 illustrates one of the holographic interferograms, visualizing deflection contours on the silicon wafer 4-inches in diameter. However, it must be noted that the flatness deviations of a number of wafers tested provided much denser interference pattern, and the evaluation in such a case became troublesome.

In order to overcome the problem with the range of measuring sensitivity, and also the unpractical properties of the experimental setup, the method based on Ronchi tests of optical systems has been developed. In the optical system, an analyzer grid is positioned exactly into the focal plane of an imaging objective lens. As it is shown below, in such an optical filtering scheme the fringes of slope contours are projected onto the image of object surface. Likewise in the interferometry, a specular specimen surface is needed. A basic scheme of the optical system is shown in Fig. 4.2. The specimen surface tested is illuminated by a beam of parallel rays, emitted by the point-like source, placed in the focus of a long-focal distance objective. For the sake of simplicity of the scheme, the light source on Fig. 4.2 is not drawn.

The wavefront under consideration, reflected from the specimen, is described by the complex amplitude  $a_0(x, y)$ . As it is well-known, the light reflected backward and passed through the objective lens is transformed in its back focal plane to the Fourier transform  $A_0(\xi, \eta)$  of the amplitude  $a_0(x, y)$ . In the focal plane, a rather coarse grid is positioned, which serves as a spatial filter. This spatial filter is essentially composed of rectangular slits in one dimension parallel to the  $y$ -axis. The field immediately to the right of this spatial filter is thus proportional to

$$A'_0(\xi, \eta) = \frac{1}{2} A_0(\xi, \eta) [1 + \exp(i2\pi\xi/d)], \quad (4.3)$$

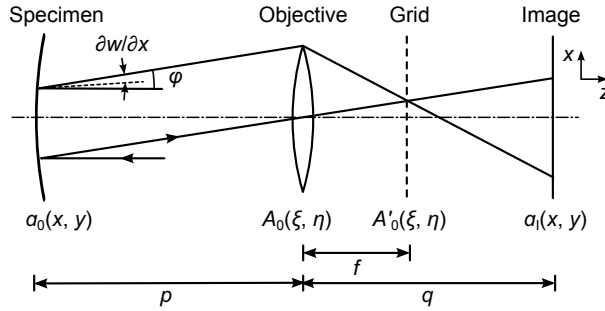


Fig. 4.2. Optical scheme of slope contours measurement.

where phase factors were omitted. In this composition, the second term is the amplitude transmittance, where  $d$  is the period of lines of the grid. We are searching for the field distribution in the image plane at a distance  $q$  from the lens, then the following convolution integral has to be solved

$$a_I(x_I, y_I) = \frac{ik}{2\pi(g-f)} \iint_{-\infty}^{\infty} \frac{1}{2} A_0(\xi, \eta) [1 + \exp(i2\pi\xi/d)] \times \exp\left[-\frac{ik}{2(g-f)} ((x-\xi)^2 + (y-\eta)^2)\right] d\xi d\eta, \quad (4.4)$$

where  $k$  is the wave number. Using Taylor series expansion and after adaptation of Eq. (4.4) we have

$$a_I(x_I, y_I) = \iint_{-\infty}^{\infty} A_0(\xi, \eta) \left[1 + \frac{1}{2} \frac{i2\pi\xi}{d} + \frac{1}{2 \cdot 2!} \left(\frac{i2\pi\xi}{d}\right)^2\right] \times \exp\left[-\frac{ik}{2(g-f)} (x\xi + y\eta)\right] d\xi d\eta. \quad (4.5)$$

Also in this equation, the quadratic terms have been omitted. Considering one of the properties of the Fourier transform

$$(i2\pi\xi)^m F(\xi) \rightarrow f^{(m)}(x), \quad (4.6)$$

where  $f^{(m)}$  is the  $m$ -th order derivative of the function  $f(x)$  and  $F(\xi)$  is the Fourier transform of  $f(x)$ . The field in the plane, where the image of the object is projected, can be summarized as follows

$$a_I(-Mx, -My) = \frac{1}{4\pi M^2} \exp[ikM(x^2 + y^2)/f] \times \left[ a_0(x, y) + \frac{\lambda f}{4\pi d} \frac{\partial}{\partial x} a_0(x, y) + \frac{1}{4} \left(\frac{\lambda f}{2\pi d}\right)^2 \frac{\partial^2}{\partial x^2} a_0(x, y) \right], \quad (4.7)$$

where  $M = f/(q-f)$  is the image magnification and  $f$  and  $q$  are the focal distance and the image plane distance, respectively. In the expression for complex amplitude, the basic terms

from the expansion of spatial filter function present zero, first and second order derivatives of the input complex amplitude. The relation between the height function of the reflected surface  $w(x, y)$  and the complex field in the  $(x, y)$  plane immediately to the right of the surface is a complex magnitude

$$a_0(x, y) = \exp[i2\pi w(x, y)/\lambda]. \quad (4.8)$$

For quadratic detection of the light intensity distribution, simply the complex amplitude must be multiplied by its complex conjugate value

$$I(-Mx, -My) = a_I^*(-Mx, -My)a_I(-Mx, -My). \quad (4.9)$$

Performing this multiplying, an expression is obtained, where the different derivatives are present

$$I(-Mx, -My) \sim \left| 1 + K_1 \frac{\partial w}{\partial x} + K_2 \left( C_1 \frac{\partial^2 w}{\partial x^2} + C_2 \left( \frac{\partial w}{\partial x} \right)^2 \right) \right|^2, \quad (4.10)$$

where the second derivative term has been taken as the last one.  $K_1, K_2, C_1, C_2$  are the constants related to the value of  $\lambda/d$ , the last quadratic term can be omitted due to its negligible value.

The influence of different terms on the resulting pattern is related to the ratio of  $\lambda/d$ . When the grid with a large distance between the slits is used, an image of object area is visible as the zero derivative of the input signal with the system of fringes of the first order derivative, overlapped on the image. Geometrically, the first order derivatives can be regarded as slope contours of surface deflections. Turning the grid around optical axis, the pattern of slope contours with regard to orthogonal  $y$ -axis can be simply obtained. In addition, by proper choice of the grid period, even the fringe pattern of slope contours, modulated by the second order derivatives – radii of curvatures – can be realized. The fringe value constant can be obtained simply by using elementary ray tracing. The rays under consideration, reflected from the specimen, are passing through the slits of the grid. These slits are projected onto the object image as a fringe pattern of slope contours. Taking into account the law of reflection and thin lens geometrical optics relations, we can get the expression for interpretation of fringes

$$\frac{\partial w}{\partial x} = \frac{N_x}{2\nu f}, \quad \frac{\partial w}{\partial y} = \frac{N_y}{2\nu f}, \quad (4.11)$$

where  $w$  is the plate deflection and  $\nu$  is the frequency of the grid.

As it can be seen from Eq. (4.11), by proper choice of grid frequency, the sensitivity of the measurement can be adjusted. Nevertheless, the limitation is obtained when high-frequency grid is used, which is followed by appearing of diffraction effects, as it is explained above. It implies the optimum frequency of the grid in a range 1–10 lines per mm at the optical arrangement with the focal distances of objective lens of about 500–1000 mm. In order to illustrate the fringe patterns, they are presented in Fig. 4.3. In the figure, there are orthogonal slope contours patterns on the same specimen.

For demonstration purpose Fig. 4.4 shows application of more dense linear grid, when also higher terms of Eq. (4.10) are considered. The additional system of clearly visible fringes presents second order derivatives curves of the thin plate surface deflections.

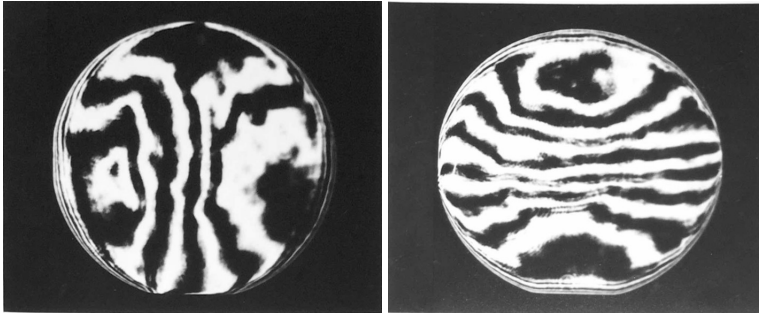


Fig. 4.3. Slope contours on the wafer surface visualized by the Ronchi grid.

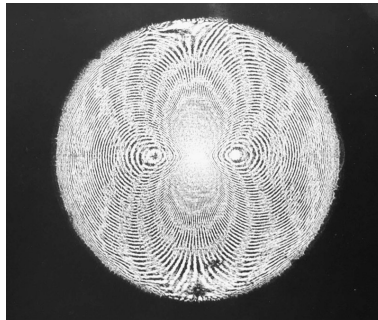


Fig. 4.4. Second order derivatives of the surface profile deformation on centrally loaded thin plate.

The problem of high sensitivity measurements of the interference contours on the surfaces of thin plates, which must often be solved by a special arrangement of the optical scheme, can be relatively easily removed by the shearing interferometry. Even large diameters of the field in the shearing interferometer can be implemented in the holographic variant, as described in section 2.3.

Mirror-like surfaces of semiconductor wafers or membranes are mostly deviated to the nearly spherical concave or convex shape and can thus be regarded as a simple optical element. Quasi-spherical mirror element reflects collimated light beam as a concave or convex mirror and creates real or virtual focus. In order to determine the focal distance or curvature, an autocollimation arrangement was adjusted (see Fig. 4.5). Besides the wafer specimen, the optical scheme is composed of only long focal distance lens and the screen moveable along the optical axis. Likewise in optical method of slope contours measurement, the specular surface of the tested object is illuminated by a collimated beam of parallel rays. The main objective lens oversized the specimen by the diameter and serves as a collimator with the point-like source placed precisely in the front focal point. After the reflection back off the wafer surface, a light beam enters the lens once more and the wavefront becomes convergent. If the light is reflected from a plane surface, the

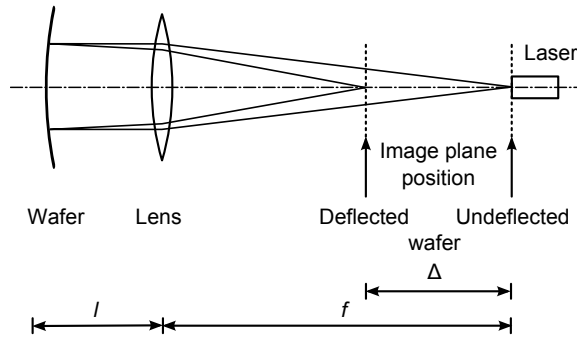


Fig. 4.5. Optical scheme of wafer curvature measurement based on autocollimation principle.

rays are collected backward into the focal spot. In Fig. 4.5, for the sake of simplicity, the light is not drawn. In technical realization, the illumination is installed from a side and directed along the optical axis by the splitting cube. In the case of either concave or convex shape of specular surface, the wafer acts as an optical element – spherical mirror – and this shifts the focus of reflected light along the optical axis either towards the objective or to the opposite direction.

Assuming the specimen as a spherical mirror, the change of focal distance of the returned wavefront can be expressed by the well known relationship for a system of two centered thin lenses at the mutual distance  $l$

$$\frac{1}{f} = \frac{1}{f_0} + \frac{1}{f_s} - \frac{l}{f_0 f_s}, \quad (4.12)$$

where  $f$  is the focal distance of two-lens combination and  $f_0$  and  $f_s$  are the focal distances of the objective and the specimen, respectively. Taking into account  $R = 2f_s$ , the radius of curvature of the mirror-like wafer can be written

$$R = 2 \left[ f_0 \left( 1 + \frac{f_0}{\Delta} \right) - l \right], \quad (4.13)$$

where  $\Delta$  is the shift of image (focal plane) of the whole system with respect to the original focal plane.

As it has been already noted, as a rule repeatedly the monocrystal wafers but also even thin membranes surfaces are deformed ellipsoidally due to materials anisotropy. In this case, the orthogonally unsymmetric surface shape reflects the rays in the form of an astigmatic beam of rectilinear rays. As it is known from basic ray tracing laws, two planes, which contain the shortest and the longest radius of curvature, are perpendicular to each other. The corresponding curvatures are usually called tangential field curvature  $1/R_t$  and sagittal field curvature  $1/R_s$ . The quantity

$$\frac{1}{R} = \frac{1}{2} \left( \frac{1}{R_t} + \frac{1}{R_s} \right) \quad (4.14)$$

is their arithmetic mean value. Both the radii  $R_t$  and  $R_s$  can be determined by using the autocollimation scheme. In this case, the backward astigmatic beam is focused into two focal lines,

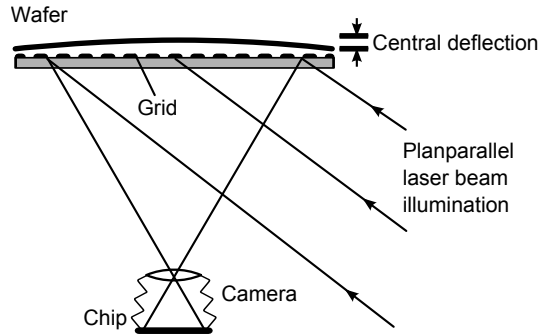


Fig. 4.6. Optical scheme of shadow moiré method.

oriented orthogonally one to the other at the separated focal planes, which by Eq. (4.12) define the corresponding values of  $R_t$  and  $R_s$ .

The realization of the optical setup consists of a laser diode chip as a point-like emitter 650 nm/10 mW, well corrected telescope doublet  $f = 1000$  mm,  $\varnothing = 152$  mm and a small ground screen, moveable together with nonius scale on a rail with a mm scale. For better searching, the focal spot is observed by a simple magnifier or by using of microscope eyepiece. The achievable precision of such a focal plane localization is under 1 mm. In spite of its simplicity, the method has proved to be very effective and reliable with the resolving power of radius of curvature determination comparable or even better to that of classic interferometry. Moreover, the presence of anisotropy in the wafer deformation is simply discovered and quantitatively determined. As for its main characteristics, it can be stated that there are no technical problems to deal with wafers of sizes from 10 mm to 150 mm and more in diameter, the method can be used to monitor the bulging of large membranes, and moreover, there are also expectations to solve simply the task of anisotropic thin film stress evaluation with a stress resolution of  $\pm 1$  MPa and up to 10 GPa range.

In testing of semiconductor substrates or when thin film residual stresses have to be determined, there is a class of problems, where the surface of the substrate scatters the light diffusely. In these conditions, the shadow moiré method has been analyzed to acquire the wafers deformation. The primary purpose of the method is to measure the out of plane shape of the plate. At the simple optical setup, the reference grid with the frequency of 10–40 lines/mm is contacted immediately on the tested surface (see Fig. 4.6). Observing this shadow perpendicularly to the surface, the specimen grating is distorted by the deflections of the surface. When such a distorted image of the grid is viewed through the same linear reference grating by eye or by CCD camera, moiré fringes are created. These fringes represent the surface contours i.e. the surface topology [56]. Dealing with wafers, the ability to measure small deflections is the basic criterion of the applicability of the method. In this meaning, the smallest measurable deflections are defined by diffraction phenomena on the reference grid. As it can be also deduced from the illustrative example in Fig. 4.7, taking the surface away from the grid plane in the wafer central part, the contrast of fringes is decreased due to diffraction, which is also the main limiting factor. The radii of curvatures of the presented specimens are  $R = 6$  m on the left-hand side and  $R = 71$  m on the

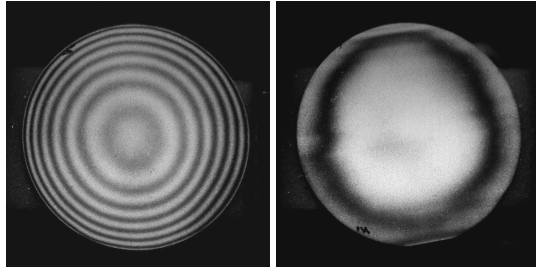


Fig. 4.7. Shadow moiré fringes on the diffuse-like slightly spherical surfaces of wafers.

right-hand side. In any case, the sensitivity of the measurement can be considerably improved by an intensity interpolation procedure between two neighboring fringes.

#### 4.2 Residual stress measurement of thin films, membranes and MEMS components

Thin films, deposited on substrates, are as a rule in a state of residual mechanical stress. Nanostructured thin films of controlled properties such as mechanical, electrical or piezoelectrical, are one of the main aims of nanotechnology. Multilayers and gradient thin films of continuously varying mechanical properties are exploited for controlled interphases in multiphase materials as nanocomposite materials. Mechanical stresses induced in mechanical structures can have a detrimental effect on their mechanical, but also electrical properties. Since the mechanical stress has a large influence on the stability, flatness and durability, particularly on thin membrane-like structures, their values have to be analysed together with the monitoring of stress response during several technological processes.

In general, experimental detection and evaluation of the mechanical stress state can be divided into two categories:

1. measurement of steady state deformation induced by residual stress in free-standing structural elements
2. measurement of deformation forced to clamped structural elements such as thin plate or membrane by controllable loading

At the present state there are some experimental-analytical methods intended especially to measure residual stress in thin multilayered wafer structures. The residual stress of the layered structure can be considered as the sum of two separate components, thermal stress  $\sigma_{th}$  and intrinsic stress  $\sigma_{in}$ , which are related by the additive manner

$$\sigma_r = \sigma_{th} + \sigma_{in} . \quad (4.15)$$

The thermal stress is a function of temperature change during deposition process and the main part of the intrinsic stress is induced by the mismatch of both the crystalline lattices at the interface of adjoining layers. Such a stress is related to the mutual combination of materials,

conditions of growing process and especially on a diffusion process. The thermal component of the clamped-clamped structure can be described by a simple relation

$$\sigma_{\text{th}} = \frac{E}{1 - \nu} \Delta\alpha \Delta T, \quad (4.16)$$

where  $E$  is Young's modulus,  $\Delta\alpha$  is the difference of thermal expansion coefficients and  $\Delta T$  is the temperature difference. To evaluate thin layer mechanical stress the simple analytical expressions are used but precise reliable residual stress distribution evaluation leads to the need of applying right constitutive strain-stress relationship. Moreover, there is also uncertainty in intrinsic stress assessment in crystalline mesh which is not covered by common approximations of classic continuum mechanics.

The well-known measurement of film stresses of coated wafer or substrate of cantilever beam belongs into the first category where the free deformation induced by stress is measured. The presence of residual stress creates the buckling residual deformation in thin plate type components. Knowing this deformation, thin film stress can be determined through the use of a simple analytical expression, Stoney's relation [57]. The biaxial stress in the film relates to the change in substrate curvature as follows

$$\sigma_f = M \frac{h_s^2}{6R h_f}, \quad (4.17)$$

where  $h_f$  is the film thickness,  $h_s$  is the substrate thickness,  $M$  is the biaxial modulus of the substrate and  $R$  is the induced curvature due to the residual stress. Since thin plate deformation for homogeneous isotropic material has only a simple spherical shape, experimentally the problem is reduced to the determination of radius of curvature of the buckling. In the field of microelectronics monocrystalline materials we are dealing mostly with orthogonal materials, consequently anisotropic residual stress distribution is present. Then, on the basic assumptions of thin plate elastic theory, for orthotropic substrate material it can be obtained

$$\begin{aligned} \frac{\partial^2 w}{\partial x^2} &= \frac{1}{R_x} = 6 \frac{h_f}{h_s^2} \left( \frac{1}{c_{11}} \sigma_{1f} + \frac{\nu_{12}}{c_{12}} \sigma_{2f} \right), \\ \frac{\partial^2 w}{\partial x^2} &= \frac{1}{R_y} = 6 \frac{h_f}{h_s^2} \left( \frac{\nu_{12}}{c_{12}} \sigma_{1f} + \frac{1}{c_{44}} \sigma_{2f} \right), \end{aligned} \quad (4.18)$$

where  $w$  is the deflection of thin plate wafer deformation,  $h_f$  and  $h_s$  are the thicknesses of thin layer and substrate respectively,  $\sigma_{1f}$ ,  $\sigma_{2f}$  are thin film layer anisotropic stress components and  $c_{11}$ ,  $c_{12}$ ,  $c_{44}$  are anisotropic thin plate – substrate parameters. As follows from Eq. (4.18) to determine both the anisotropic stress components only curvatures mutually orthogonal of the plate deformation have to be measured.

As it was mentioned above, a variety of optical methods for flatness inspection is possible to use for curvature measurement. From the point of view of easy realisation, for example, the residual stresses can be determined by autocollimation measurement with a reasonable precision of several MPa in a large range of film thicknesses from several nanometers to micrometers. The accuracy of the above described methods is usually satisfactory for reliable determination of stresses also on the samples as small as 10–20 mm in diameter, even without the installation of photoelectric or CCD based detection and/or somekind of signal processing.

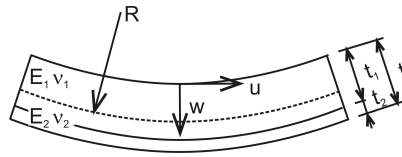


Fig. 4.8. Scheme of double-layer structure curving.

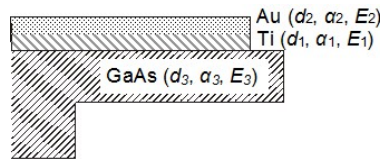


Fig. 4.9. Three-layers basic composition of the cantilever [24].

Similar residual stress determination, based on Eq. (4.17), can be realized also on free-standing double layer strips of cantilevered beams. Assuming the cylindrical-like curving of the cantilever in this case, the end of the beam clamped at one of the ends is deflected.

During the process of development of the sophisticated GaAs based microwave power sensors with the integrated thermal converter (MTC) device as a heart [58], the investigation of thermomechanical properties of the device was one of the essential parts of design. The multi-layer heterostructure based design is often complicated. It consists of various materials of each other different thermomechanical parameters. For optimization of the thermomechanical design using 2D models, especially for membrane-like structures, is reasonable.

To define the optimum configuration of GaAs based MTC device, three basic types of mechanical elements has been investigated, the cantilever beam, the doubly clamped bridge and also microisland element. All the elements have the same or similar GaAs or GaAs/AlGaAs multilayer membrane structure.

The numerical analysis of the structural element that was carried out required to be supported by experimental verification and testing of thermomechanical properties.

The characteristic feature of the clamped cantilever beam is its large steady state deformation induced by thermal stresses created at the process of deposition. The overall cantilever structure is composed of three basic layers – GaAs and metal films Ti/Au (see Fig. 4.8 and Fig 4.9). With regard to the flat shaped structure, thin plate plane strain model can be used based on the theory of bi-metal thermostats. Basic formulas for bi-layer strip element thermal deformation were derived e.g. in [59]:

$$\frac{d^2w}{dx^2} = \frac{1}{R} = \frac{\varepsilon_f(h_1 + h_2)}{2\Theta(D_1 + D_2)}, \tag{4.19}$$

$$\begin{aligned}\Theta &= \frac{1}{12} \left( \frac{h_1^2}{D_1} + \frac{h_2^2}{D_2} + \frac{3(h_1 + h_2)^2}{D_1 + D_2} \right), \\ D_1 &= \frac{E_1 h_1^3}{12(1 - \nu_1^2)}, \\ D_2 &= \frac{E_2 h_2^3}{12(1 - \nu_2^2)},\end{aligned}\tag{4.20}$$

where  $w$ ,  $h_1$ ,  $h_2$  are the magnitudes of double-layer geometry – deflection, thicknesses of the first and the second layer, respectively,  $E_1$ ,  $E_2$  and  $\nu_1$ ,  $\nu_2$  are the Young modulus and the Poisson ratio, respectively,  $D_1$ ,  $D_2$  are the flexural rigidities,  $R$  is the radius of curvature. The value of  $\varepsilon_f$  is the free-standing strain, that is for thermal problem

$$\varepsilon_f = \Delta\alpha_{th}\Delta T,\tag{4.21}$$

where  $\Delta\alpha_{th}$  is the difference between coefficients of thermal expansion of the layers and  $\Delta T$  is the temperature difference. The free-standing deformation induced by each of layers is additive, i.e. the multilayer system can be evaluated step by step after depositing of each of the layers.

$$\frac{1}{R} = \sum_{i=1}^N \frac{1}{R_i}.\tag{4.22}$$

For the specific case if the thickness  $h_1$  of the film is much more thin than the thickness of the substrate  $h_2$ , the previous formulas lead to the expression

$$\frac{1}{R} = \frac{6\varepsilon_f h_1}{h_2^2},\tag{4.23}$$

that is for film stress of each of the layer  $\sigma_i$  Stoney's formula Eq. (4.17) is obtained.

### 4.3 Microinterferometry

Dealing with specular surfaces in order to characterize 3D profile of small MEMS structures and elements, mostly the interference principle is used. Using the coherent laser light, the interference between light reflected from the surface and that returned back from a reference flat produces interference fringes. The resulting fringe pattern is a contour map of the phase differences between the two wavefronts.

The basic optical element of the microscopic laser interferometer setup is light splitting cube of two prisms. The interference effect is appeared in the air gap between the cantilever surface and outlying bottom flat of the splitting cube. That is the mutual interferency is created by the interaction of two light wavefronts, reflected from object surface and that reflected back from bottom flat of the cube.

The laser beam from He-Ne laser was extended to wide diameter beam of light by using collimator (see Fig. 4.10). This basic scheme of interferometry is generally named as Tolansky arrangement.

In the interferometer the optimal intensity conditions were adjusted by rotating of plane of polarisation of the laser source. By this way also disturbing secondary reflections can be minimised and the interference pattern is not blurred by parasitic fringes. In microelectronics elements the

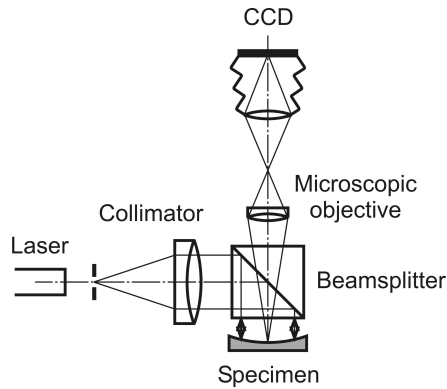


Fig. 4.10. Scheme of the Tolanski microinterferometer.

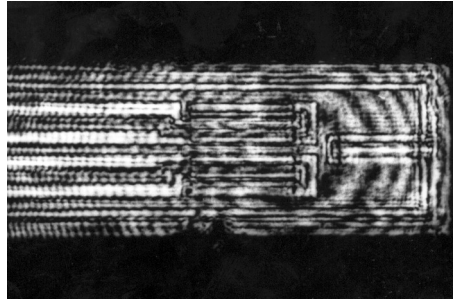


Fig. 4.11. Steady-state deformation of the multilayer membrane bridge [60].

amount of light reflected from the surface and that of flat reference glass surface not covered by a reflection coating are adequate to create contrast interference pattern. The splitting cube is fixed on a two axes adjustable holder. Besides the good flatness of the cube surfaces, the only critical element is aberration free collimator objective. The image of object is viewed and magnified at a suitable measure by microscopic objective and built-in CCD camera. Regarding finite size of the beamsplitter cube, a microobjective with long working distance has to be used. Large field of view, easy adaptation of the arrangement to variety of purposes and also the potential possibility of simultaneous observation of thin film interference pattern on transparent surface covering are the practical advantages of the device.

Several kinds of the structural elements made of Si, GaAs and GaN based technology of membrane-like structures have been observed by using this tool (see e.g. Fig. 4.11).

In Fig. 4.12 from the fringe pattern along the length of cantilever the profiles of curvature are drawn. As it can be seen, besides the visualisation of steady-state profile after its technological forming, the changes generated as a thermal response by acting different feeding power can be inspected, too.

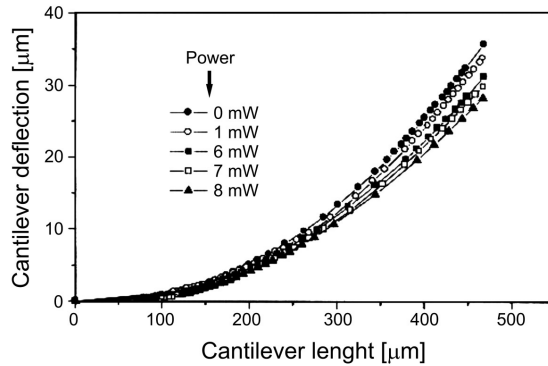


Fig. 4.12. Free-standing deformation of the GaAs based multilayer cantilever thermally loaded [61].

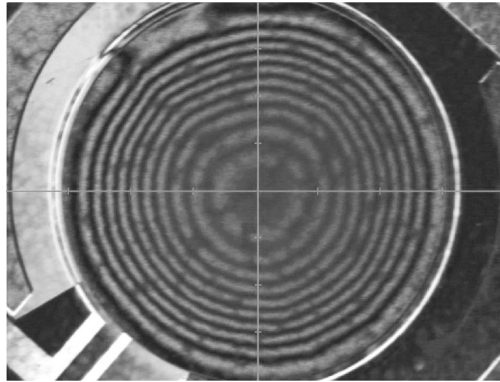


Fig. 4.13. The interference fringes obtained by white light interferometry of the bulging of AlGaIn/GaN membrane  $4.2 \mu\text{m}$  thick and  $1.52 \text{ mm}$  in diameter at pressure  $8 \text{ kPa}$ . Fringe value is  $0.263 \mu\text{m}$ .

In microinterferometry, there are three basic optical schemes – Michelson, Mirau and Tolan-sky interferometers, depending on the position of reference glass flat in the arrangement. As a rule, the optical arrangement is integrally built into the microscopic lens. Each of these types of geometry has its own specific features. Michelson type of interferometer is e.g. regularly used in connection with microscopic objectives of smaller magnification  $1\times$  to  $5\times$ , larger viewing field and also larger working distance. An example of deformation contours on the AlGaIn/GaN based membrane bulged by overpressure is shown in Fig. 4.13. The interference pattern was obtained by white light interferometry using  $525 \text{ nm}$  LED light wavelength (WLI Bruker Con-tour GT-K1). Low coherence or white light interference microscope is an advanced tool with some specific advantages over the “conventional” interferometric technique. It is primarily the ability to strongly reject light that has undergone scattering outside which gives the generation of speckles when illuminating by coherent light. When a low coherence light is used in inter-

ference microscope, and the microscope objective is moved continuously in line-of-sight axis, the contrast of interference fringes is modulated depending upon the optical path difference. A basic principle is searching for the position of maximum contrast simultaneously for an array of image points. Thus, a surface profile can be measured by finding the maximum peak position of the fringes modulation in a CCD camera. Nevertheless, the position of optimal fringe pattern contrast for low LED based light source can even be found, thus providing the opportunity to observe immediately the whole field of view as seen in Fig. 4.13.

The task to evaluate the stress of tensioned membrane can be solved by bulging method or by the method of resonant frequency determination. Bulge testing was one of the first techniques to study the membrane stress. During the test, a uniform pressure is applied to one side of the membrane, properly clamped or supported over its edge.

The bulging method of tensile stress measurement is based on the second order differential equilibrium equation by which the relationship membrane deflection vs. acting load is described. The deflection  $w(x, y)$  of the stretched membrane under an external pressure load  $p(x, y)$  is given by Poisson's equation

$$\Delta w(x, y) = -\frac{p(x, y)}{\tau}, \quad (4.24)$$

where  $\Delta$  is the Laplace operator,  $x, y$  are the coordinates of the point of the membrane surface under consideration,  $p(x, y)$  is the constant load, perpendicular to the membrane surface and  $\tau$  is the tension force per unit length of an arbitrary shaped membrane boundary. Membrane tensile stress is related to the force  $\tau$  and the membrane thickness  $h$  as

$$\sigma = \frac{\tau}{h}. \quad (4.25)$$

For small deflections assumption the second order derivatives in Eq. (4.24) can be express by the principal radii of curvatures  $R_x, R_y$  with respect to the orthogonal coordinates

$$\frac{1}{R_x} + \frac{1}{R_y} = -\frac{p}{\tau}. \quad (4.26)$$

For experimental of the membrane tension evaluation usually these radii of curvatures have to be measured.

Experimental evaluation of the initial membrane prestress is performed following Eq. (4.26). In order to distinguish between the intrinsic prestress  $\sigma_0$  and the membrane stress induced by the bulging deformation we get

$$\sigma_0 + \sigma_p = -\frac{pR}{2h}, \quad (4.27)$$

where  $\sigma_p$  is the induced tensile stress. The pressure induced stress can be simply calculated using Hooke's law and geometrical relations of the bulged membrane deformation

$$\sigma_p = \frac{E}{1-\nu} \frac{r^2}{6R^2}, \quad (4.28)$$

where  $r$  is the half diameter of the membrane contour.

For small sizes membrane like in Fig. 4.13 the tools of microinterferometry can be used, but for membranes with lateral diameter up to 150 mm the application of autocollimation technique

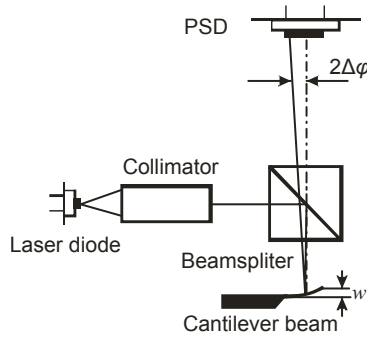


Fig. 4.14. Schematic drawing of the cantilever deflection measurement by PSD.

has been chosen. The deflected surfaces of the membrane in their central region are always nearly spherical, so that the autocollimation focus searching provides directly the information immediately necessary to find the tensioning of the membrane. In order to improve the sensitivity of the best focal plane searching, the Fourier diffraction analysis of the near vicinity of focal plane region has been done. In this region, the focal spot in detail visualizes any deviations of the membrane surface from an ideal spherical shape and the methodology has served to improve results to a very good measuring precision. Another advantage of this approach is also direct optical fitting of the mean spherical shape in the presence of local surface deviations. Such surface distortions are well observed as the focal spot blurring. The theoretical/experimental analysis of the best focus detection has led to a very good stress measurement accuracy achieved, not worse than some tenths of a MPa in the range of membrane tensions 1–20 MPa.

The steady-state deformation induced in double or multi-layer cantilever clamped in one of its leads to a simple circular shape. Therefore, the curvature can be deduced from inclination of its free end area. The laser reflectance scheme was arranged to monitor the deflections at the tip of microcantilever of only 340  $\mu\text{m}$  long. A narrow laser beam was focused through the small collimator onto the small area specularly reflecting the light backwards to the position sensitive detector (PSD), see Fig. 4.14. The linear PSD captures the differences in the electrical signals from two opposite ends of the common photodiode substrate. Provided that the characteristic of PSD is linear, the linear relation exists also between the output signal  $U$  and the change in surface inclination. At the small slopes of surface the deflection  $w$  is related to lateral coordinate  $x$

$$U = K2 \frac{dw}{dx}, \quad (4.29)$$

where  $K$  is the factor of proportionality – sensitivity value. The sensitivity value was calibrated at static conditions as a transfer characteristic by varying the angle of inclination. In the calibration a very good proportionality was obtained in spite of considerable distortion of the reflected light spot on the effective PSD area, it implies that the accuracy of measurement is not affected strongly by this frequently happened effect. Besides the coupling of the output signal with interferometrical deflection measurement, the comparison was made with the analytical solution of double material thermal deformation. Provided that the rectangular cross section cantilever

is composed of two uniformly thick layers, the radius of curvature of the arc-shaped microbeam should be

$$\frac{d^2w}{dx^2} = \frac{1}{R(x)} = \frac{h\Delta\alpha\Delta T}{2\Lambda D}, \quad (4.30)$$

where  $\Delta\alpha$ ,  $\Delta T$  are mismatches between coefficients of thermal expansion and temperatures, respectively,  $h$  is the whole thickness of the microbeam,  $D$  and  $\Lambda$  are constants related to material. Changing the radius  $R(x)$  the variations of inclination angle at the tip of clamped microbeam can simply be calculated.

#### 4.4 Vibration measurement of multilayer membrane-like microcomponents

As it was mentioned above, measurements of internal or residual stress in microstructures were commonly realized either by observing the static shape residual deformation or the deformation forced to element. The values of resonant frequencies of the membranes as structural elements are related predominantly to the tensile stress, acting to keep it flat. Thus, knowing the value of resonant frequency, the membrane stress can be calculated.

The apparatus of Laser Doppler Vibrometer with pointwise sensing of vibrations was used for the detection of vibration movements of both the macro as well as microelement of the membrane-like structural components. The applicability of resonant frequency values obtained in the ambient air was established experimentally only for stress evaluation on small size membranes as a maximum some mm in diameter. Then a proper frequency range for stressed membranes is 1–20 kHz. In the case of large membranes, such as e.g.  $\varnothing 126$  mm, the air damping is inaccessibly high and the stress evaluation is impossible. To overcome the problem, a vacuum apparatus was arranged, where the membrane inside the vacuum chamber was excited electrostatically and its periodical bulging vibrations were observed by Laser Doppler Vibrometer probing beam through the optical window. The developed methodology of membrane stress determination has achieved good accuracy in the order of 0.1 MPa.

Small dimensions of the bridges, with lengths varying from 150  $\mu\text{m}$  to 900  $\mu\text{m}$  and with width 90  $\mu\text{m}$ , limit the conditions of tiny mechanical loading. Frequently used the electrostatic method for mechanical exciting was not appropriate, then the loading through the acoustical coupling was chosen. Two variants of the acoustic excitation can be applied there – by short acoustic pulse or by scanning of the appropriate frequency range.

Circularly shaped micro-membranes with diameters of 750, 1 000 and 1 500  $\mu\text{m}$  were excited by acoustic short time pulse generated by mechanical shock. The frequency content of this pulse as a wide band excitation reached the frequencies up to 200–300 kHz. The excitation was carried out at atmospheric ambient conditions. The measured samples were fixed in a holder and the focused spot from the laser vibrometer head scanned the area of diaphragm point by point. Analog signal from the vibrometer head Polytec OFV-302 was preprocessed by OFV-2601 controller and then recorded by LeCroy 808Zi. The intrinsic membrane residual stress was evaluated by iterative procedure comparing experimental frequency value with that of numerically obtained by 3-D FEM modeling using ANSYS SW tool.

Another way of excitation of mechanical movement by sound can be regarded as very desirable because of its tenderness and simple handling with both intensity and frequency adjusting. The main difficulty here is the problem with quantifying of the acoustic pressure values. We

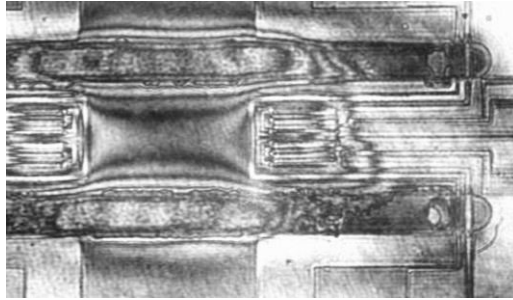


Fig. 4.15. Microinterferometrical view of the membrane bridge with coplanar waveguides.

attempted to get over this drawback by calibrating of acoustic pressure emitting on loud speaker membrane by precise measurement of membrane vibration velocities. The method was tested on microfabricated GaAs based membrane bridge  $790\ \mu\text{m}$  long with the thickness of about  $1.0\ \mu\text{m}$  (see Fig. 4.15). This absolute calibration of membrane element bulging is based on the relationship between the velocity of longitudinally vibrating air particles induced by speaker and the periodic pressure changes

$$p = \rho c v, \quad (4.31)$$

where  $v$  is the velocity of vibrations, and the composition of air density  $\rho$  and sound velocity  $c$  is the so-called wave resistance. At room conditions this value is  $\rho c = 415\ \text{kg m}^{-2}\text{s}^{-1}$ . In the nearest neighborhood of the exciting membrane the same value of acoustic pressure can be accepted. For plane wave of sound the acoustic pressure and acoustic velocity are in phase that in Eq. (4.31) can be used to calculate the pressure. LDV is an ideal tool to gauge the velocities of loud speaker membrane vibration, hence the value of acoustic pressure can be accurately determined precisely.

Another approach how to realize sound excitation with controlled value of acoustic pressure has been proposed. For this method a small chamber of pistonfon generated periodic harmonic changes of uniform pressure under the small membrane. Pistofon Metra RFT PF-101 designed for microphone calibration provides nominal pressure 118 dB sound level at 173 Hz, which is related to 15.8 Pa (RMS) of the acoustic pressure. Usually, the range of sound intensity of some tens of Pa is adequate to experiments with microcomponents.

The tension of a tested bridge membrane defines the first resonant mode at the region of 60–100 kHz, thus preventing the resonant excitation in the cavity of pistonfon. On the other hand the expressive bulging oscillations of the bridge are presented at low sound frequencies where the pistonfon or loud speaker actuation is very effective. The amplitudes of the oscillations are so high that the movements at hundreds of Hz have a quasi-static nature with negligible inertial effect. Therefore, the static bulging can be taken into account and the appropriate expressions for membrane bulging can be used to calculate the tension knowing the absolute value of acting acoustic pressure.

The schematic drawing of the LDV measurement setup used to perform the measurements of the membrane like elements is shown in Fig. 4.16. The heterodyne LDV was OFV-303 in-

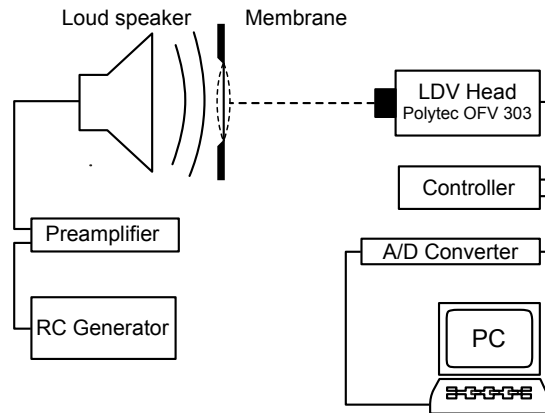


Fig. 4.16. Experimental setup of the micromembrane element bulging measurement by Laser Doppler Vibrometer.

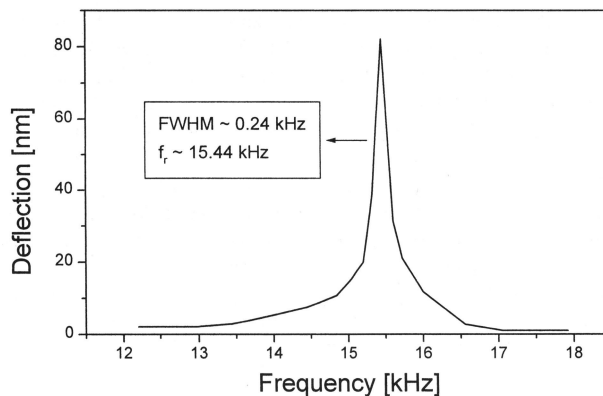


Fig. 4.17. Frequency characteristic of the multilayer microcantilever. The vibration of the cantilever was excited by sound pressure [61].

terferometric head with controller OFV-2601 made by Polytec. The useful signal from the head amplified and decoded by the controller proceeds in analog form through A/D converter Advantech PCL-818 to PC.

The maximum deflections measured varied from about 30 nm to 100 nm which values corresponded to 100–120 dB of acoustic pressure, accordingly the evaluated tension was found to be in the range 10–25 MPa. These stress values were approved independently by numerical computation using MEMCAD Coventor Ware simulator but also by residual stress state monitoring during the deposition and etching procedures.

Having a possibility to actuate simply such a double-layer system, the measurement of resonant frequency curve was offered by itself. The plotted resonant characteristic is shown in Fig. 4.17. As seen, the peak is remarkably sharp which fact leads to small damping factor. The

reduced damping factor  $\gamma = 4.5 \times 10^{-3}$  was obtained by using the half power bandwidth method. However, as it must be noticed, the experiment with the LDV detector was realized in the ambient air thus lowering the vibrations. Although the air damping effect tends to be negligible with smallest vibrating objects sizes, precision determination of the damping value needs the sample to be installed in vacuum.

Accordingly, the well defined ambient conditions are necessary when the effect of surface stress induced bending or thermal mismatch on resonant frequency shift is analyzed. We studied the same effect in connection with curved static residual deformation but the results were not convincing.

On the contrary, the effect of resonant frequency shift was detected on 3-inch silicon wafers deposited with 1  $\mu\text{m}$  film of amorphous silicon. Before and after the deposition, the wafer deformation (radius of curvature) was optically measured in order to determine the residual stress. The frequency characteristic of the wafers was evaluated by LDV in the same setup as it is drawn in Fig. 4.16. From the face side – polish surface of the specimen, the membrane of the loud speaker is acoustically coupled on the disc of wafer. For the tiny and thin walled elements of silicon wafers there is a key factor to secure the mechanical vibration to be free of any undesirable influences. In the experiment the wafer disc was hanged on two tiny textile fibers with orientation of disc surfaces vertically. The fixation with flexible hanging realizes reliably free-free boundary conditions, any other fixation either clamped or bending is not experimentally reproducible enough to avoid uncertainties. With regard to that aspect it is better to use the reflection of the probing laser beam from the back side diffusely scattering the light. In the case of using polished side reflection the small reflection angle fluctuations of the hanged specimen can cause problems with the loss of signal outside of LDV head objective. The resonant frequencies measured on two wafers are listed in Tab. 4.1 where also an analytical calculation values are given.

#### 4.4.1 Visualization of different mode shapes of thin membranes

In addition to the experiments on large 6-inch in diameter silicon stencil masks membranes the small silicon membranes with square-shaped geometry were analyzed on the membrane tension stresses. The specimens with the thickness of about 3  $\mu\text{m}$  and dimensions 10  $\times$  10  $\text{mm}^2$  or 5  $\times$  5  $\text{mm}^2$  respectively, were used.

To test the small membranes two concepts were designed, the former based on LDV detection of vibrating membranes deflections and the latter used the autocollimation scheme and photoelectrical signal acquisition.

Tab. 4.1. Experimentally measured shifts of resonant frequencies affected by film stresses.

Resonant frequency Hz		Without film		With film
		Experimental	Analytical	Experimental
<i>Sample 1</i>	Mode 1	1 105.5	1 103	1 113
	Mode 2	2 520.7	2 513	2 524
<i>Sample 2</i>	Mode 1	1 082.7	1 082	1 086
	Mode 2	2 471	2 465	2 471

In principle, no essential difference in measuring setup of membranes when using laser Doppler vibrometer was carried out (see Fig. 4.16). Though, handling with such a delicate structure in atmosphere, care must be taken with regard to adding mass of membrane neighboring air gas. This means that the acquired resonant frequencies in the air ambient have to be corrected for air damping to obtain their true values. Mostly the empirical expressions are used for such corrections more or less successfully. Analysing a number of our measurements performed, the frequency of the first natural mode has to be corrected by a factor of  $f_{vac}/f_{air} = 1.52$  for  $10 \times 10 \text{ mm}^2$  specimens or  $f_{vac}/f_{air} = 1.28$  for  $5 \times 5 \text{ mm}^2$  size, respectively.

The membrane stress evaluation was based on the known expression for square membrane natural frequency

$$f_{11} = \frac{\sqrt{2}}{2} \sqrt{\frac{\tau}{\mu A}}, \quad (4.32)$$

where  $\tau$  is the tension per unit length of edge,  $A$  is the area of membrane and  $\mu$  is the mass per unit area. As the value of stress is related to the square of frequency, any deviations of the real value will cause considerable errors in stress determination. That is why the measurement in vacuum conditions is highly desirable. Regarding this fact a vacuum apparatus was installed with an optical window for membranes illumination and reflection backward. To excite the membranes vibrations in vacuum an electrostatic loading was implemented.

A number of specimens were analyzed with the tension stresses varying from nearly zero to about 30 MPa, the corresponding resonant frequencies reached the values up to 20 kHz. Statistical assessment and the repeatability obtained allow us to estimate the measurement uncertainty to about  $\Delta\sigma = \pm 0.1 \text{ MPa}$  even on small mm sized samples which value seems to be a very good result for such a measurements.

Sometimes, either from designing or economical reasons, the use of LDV is not a profitable solution. That was also the case when the small membranes had to be measured in-situ during the process of their irradiation by ions flux. In accordance with this demand an optical autocollimation method intended for detection of dynamic membrane bulging immediately inside vacuum chamber has been developed. The autocollimation detector where the object is illuminated by a collimated parallel beam, detects the changes in membrane surface curving. In the layout the laser diode emits as a point-like source and after its reflection from the mirror-like membrane surface the rays are again collected on the opening of pinhole. Provided that the surface is flat, the properly chosen opening diameter (about  $\varnothing = 0.1 \text{ mm}$ ) ensures all the reflected light is passing through. The periodical bulging of vibrating membrane dissipates the light on the diaphragm screen thus reducing intensity on the photodiode. After its amplification the useful signal is processed by FFT and displayed in real time mode for frequency scanning. One of the practical benefits of the scheme is the possibility of installing it outside the vacuum chamber at arbitrary large working distance from the specimen. The sensitivity of detection is approved to be sufficient and moreover the detector can be installed immediately inside the vacuum, then only the electrical connections are needed. Such detector was used to monitor the degradation changes in thin layer films at the process of ions irradiation by means of continual stress evaluation successfully. The drawback of the confocal scheme follows from its limitation to measure the first natural mode of membrane bulging.

The analysis of vibration spectra of microcomponents and also membranes, as a rule abounds in uncertainties of main resonant peaks identification. Measuring the vibrations of “unknown”

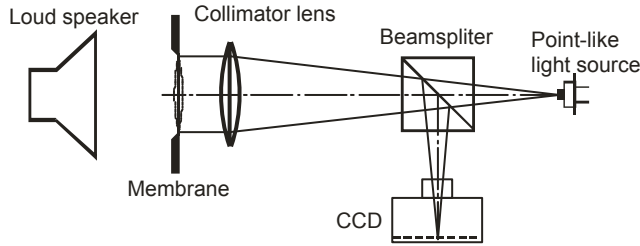


Fig. 4.18. Visualization of membranes vibration modes in focal plane of the lens.

peaks of considerable intensity are displayed as harmonic multiples due to non-harmonically shaped signals. When the bulging shapes exceed the approximations regularly assumed in analytical solutions, the observation and visualization of membrane shapes can become important. Frequently used manner of mode shapes visualization is the method of scanning LDV or eventually Electronic Speckle Pattern Interferometry (ESPI). Also microinterferometric technique can be used. Both, the classic interferometry and ESPI can operate either in time-average or in stroboscopic modes. Recently, we have developed the technique of vibration modes visualization based on observation of time-averaged intensity distribution at focal plane of autocollimation scheme. The principal layout is drawn in Fig. 4.18.

Based on the theory of diffraction the intensity distribution can be obtained by solving the Fourier transform integral. Provided that the membrane surface is expressed as a function  $w(x, y)$  and the constant distribution of illumination intensity on the membrane area is assumed, complex amplitude at focal plane of image lens will be given simply by Fourier transform of exponential function  $\exp[i2\pi/\lambda w(x, y)]$

$$a(x_f, y_f) = \iint_{-\infty}^{\infty} \exp \left[ i \frac{2\pi}{\lambda} w(x, y) \right] \exp \left[ -i \frac{2\pi}{\lambda f} (xx_f + yy_f) \right] dx dy \quad (4.33)$$

where the quadratic phase factor in front of the integral has been omitted as irrelevant when searching for intensity distribution. To find the distribution of intensity field across the focal plane of the lens a squared value of complex amplitude  $a(x_f, y_f)$  is derived. Furthermore, the time average mode needs the focal intensity pattern to be integrated in time with regard to the oscillating harmonic movement. As the bulging shapes can be mostly expressed in a simple analytical form of harmonic oscillation, the solution of integral either in a closed form or in discrete form numerically should be successfully performed. Experimental materialization of the proposed detector has shown that the method provides good conditions for identification of separated vibration modes. In the same way, the vibration at the intervals “between the resonances” is feasible to observe. An example of time-averaged intensity spots for three selected modes is shown in Fig. 4.19 where also in its left part the appropriate bulging shapes are drawn. The patterns listed show the bulging of square-shaped membrane  $10 \times 10 \text{ mm}^2$  with maximum central deflection in the range of  $5 \mu\text{m}$ . As it can be seen, the extrapolated sensitivity for bulging values detection is comparable or even exceeds the interferometrical measurements. Although time averaged, the clear and contrast patterns are obtained with excellent resolution of any membrane shape deviations.

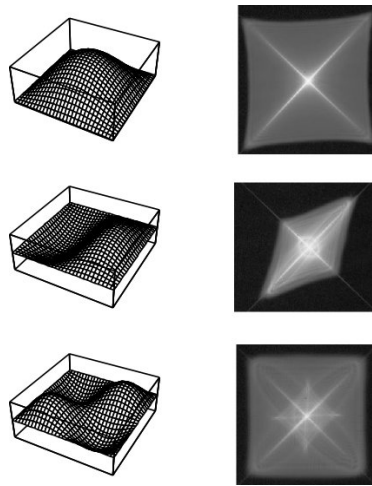


Fig. 4.19. The intensity patterns in the focal plane of the different vibration modes.

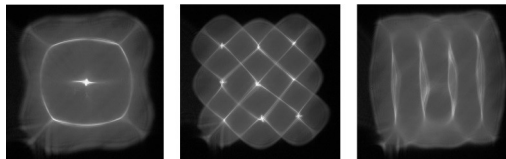


Fig. 4.20. The examples of higher order membrane vibration modes obtained by defocusing phase visualization.

Moreover, besides the use of time-average focal plane visual display, an optical method has been proposed where image defocusing near the image plane acts as a phase visualization. Observation plane shift of about 10 mm at the projecting lens focal distance  $f = 1000$  mm can detect shape variations of the mirror-like surface. As it was experimentally approved, subnanometer membrane deflections can be detected. Time-average microscopic phase visualization gives rise to characteristic patterns of different vibrating modes (See fig. 4.20). Both schemes are non-interferometric techniques of mode shapes visualization.

## 5 Conclusions

Addressing a large part of engineering but also scientific tasks cannot be imagined without the use of the experimental mechanics tools. Although computational methods based on finite elements or boundary elements are widely used today, experimental methods still have their interest in the testing and diagnostics of the deformable body. Significant share of these tools includes metrological methods using optical principles for monitoring and quantitative evaluation of mechanical quantities such as mechanical strain, vibration modes, thermal and moisture propagation measurement, surface roughness. About the last 50 years, optical methods in experimental mechanics have passed a long way of development, from the invention of new principles to their improvements and application in many areas. Today, optical measurements are still playing important role in the experimental field, although many of these procedures and equipment are now out-of-date.

Nevertheless, the historical development of the use of different principles, where the key point was the discovery of the holographic or speckle interferometry, respectively, may be in many respects instructive and useful even for a reader not directly interested in the subject-matter. This work more or less follows the mainstream in the last decades and on the basis of author's own experience and shows development directions of the fundamental principles based mainly on the exploitation of coherent light imaging. Apart from this, the physical aspects of imaging by coherent light and creating an interference pattern by light that is coherent per partes within a radius of correlation, are still relevant also for a design of new or improved interferometers.

As a rule, today, wet-processing of photographic material is not used. The design of laser diode as well as invention of CCD or CMOS matrix in connection with PC enabled immediate digitalization of the recorded image. Unfortunately, up to date, CCD (CMOS) pixel size is still too rough to record micro-interference pattern. Thus, direct hologram phase registration is problematic and only the speckle field intensity distribution can be analysed. This creates limitations for the holographic/speckle records and retards effort to obtain complete information on all the orthogonal components of the displacement vector. Moreover, noticeable limitations result also from interference sensitivity or resolving power of the electronic speckle pattern interferometry which is often insufficient to measure small scale deformation. Especially, stress analysis of the deformable body suffers from the necessity to convert information on displacement field into strains by mathematical processing. Mesh of incremental information on the interference fringes positions is usually too gappy to its direct derivation and high-performance fitting procedures is necessary to use. One of the perspective solution, as we have proposed, is the hybrid experimental-numerical approach, where the primary data obtained from experiment are evaluated with respect to wanted physical quantity distribution.

Finally, as it can be concluded against the background of past gradual development, the use of optical metrology tools has been accepted across the breath of engineering and scientific disciplines. The use of computers and the photoelectric data collection with the digital image and electric signal processing, including data fitting procedures, points to the new possibilities to enhance performances and extending the scope of the coherent light imaging for measurement purposes.

## Acknowledgement

This work was supported by the Slovak Research and Development Agency under the contracts No. APVV-0108-11 and No. APVV-0088-12.

## References

- [1] E. B. Alexandrov, A. M. Bonč-Brujevič: *Žurnal tech. fiziki* **37(2)** (1967) 360
- [2] J. M. Burch, J. M. J. Tokarski: *Opt. Acta* **15** (1968) 101
- [3] M. L. Williams: *J. Appl. Mech.* **19** (1952) 526
- [4] A. S. Kobayashi: *Linear elastic fracture mechanics in Computational Methods in the Mechanics of Fracture* (Ed. S. N. Atluri, North Holland, Amsterdam 1986)
- [5] M. M. Makogon, J. N. Ponomarjev: *Opt. i Spektrosk.* **4** (1973) 762
- [6] A. L. Mikaeljan, V. F. Kuprišov, J. G. Turkov, J. V. Andrejev, A. A. Ščerbakova: *Kvantovaja Elektronika, Sov. Radio* **1** (1971) 102
- [7] L. B. Freund: *J. Mech. Phys. Solids* **20** (1972) 129
- [8] J. A. Abersson, J. M. Anderson, W. W. King: *Dynamic analysis of crack propagation in elastic solids in Elastodynamic crack problems* (Ed. G. C. Sih, 1977)
- [9] R. Schirrer: *Int. J. Fracture* **14** (1978) 265
- [10] G. Martinček: *Some problems of dynamics of viscoelastic bodies* (Report SPZV III-6-8/18, USTARCH SAV, Bratislava 1974)
- [11] J. Balaš, M. Držík: *Staveb. čas.* **31(6/7)** (1983) 447
- [12] M. E. Fourney: *Exp. Mech.* **8(1)** (1966) 33
- [13] M. E. Fourney, K. V. Mate: *Exp. Mech.* **10(5)** (1970) 177
- [14] R. J. Sanford: *Fringe Patterns in Photoelastic Holography in Progress in Experimental Mechanics* (Ed. V. J. Parks, Cath. Univ. of Amer., Washington 1975) 167
- [15] R. Holloway, R. H. Johnson: *Exp. Mech.* **11(2)** (1971) 57
- [16] R. O'Regan, T. D. Dudderar: *Exp. Mech.* **11(6)** (1971) 241
- [17] J. D. Hovanessian *Recent Work in Absolute Measurement of Birefringence*
- [18] M. Nisida, H. Saito: *Sci. Papers of the Inst. of Phys. and Chem. Res.* **59(1)** (Tokyo 1965) 5
- [19] M. Držík, V. Szabó, V. Škunov: *Staveb. čas.* **34(2)** (1986) 83
- [20] D. C. Holloway, A. M. Patacca, W. L. Fourney: *Exp. Mech.* **17** (1977) 281
- [21] R. Aprahamian, D. A. Evensen, J. S. Mixcon, J. L. Jacoby: *Exp. Mech.* **11** (1971) 357
- [22] J. S. Popovics, J. L. Rose, S. Popovics, V. L. Newhouse, P. Lewin, N. Bilgutay: *Exp. Mech.* **35** (1995) 36
- [23] K. E. Fällström, H. Gustavsson, N. E. Molin, A. Wahlin: *Exp. Mech.* **29** (1989) 378
- [24] M. Držík, E. Loeschner, E. Haugeneder, W. Fallmann, P. Hudek, I. W. Rangelow, Y. Sarov, T. Lalinský, J. Chlpík: *Microelectronic Engineering* **84(4-9)** (2006) 1036
- [25] J. W. Goodman: *Introduction to Fourier optics* (New York 1968) in *Photoelastic Effect and its Application* (IUTAM Symp. Ottignies 1973, Berlin-Heidelberg-New York, Springer 1975)
- [26] A. Papoulis: *Systems and transforms with applications in optics* (New York 1968)
- [27] M. Držík: *Staveb. čas.* **30(9)** (1982) 703
- [28] D. E. Duffy: *Exp. Mech.* **14(9)** (1974) 378
- [29] J. Balaš, J. Sládek, M. Držík: *Exp. Mech* **23(2)** (1983) 196
- [30] J. E. Sollid: *Appl. Opt.* **8(8)** (1969) 1587
- [31] J. Balaš, M. Držík, J. Sládek: *Boundary element method and holographic interferometry for 3-D crack analysis in Proc. Comp. Methods and Exp. Measur.* (Washington 1982) 685
- [32] J. F. Doyle: *Hybrid methods in Springer handbook in experimental solid mechanics* (Ed. W. N. Scharpe, Springer 2008) 229

- [33] M. Držík: *Holographic interferometer for in-plane displacements measurement* (Czech-Slovak Pat. 272641, 1990)
- [34] J. A. Rakušin: *Optika i spektr.* **62(6)** (1987)
- [35] W. J. Bearanek, A. A. Bruinsma: *Sandwich speckle interferometry* in *VDI-Berichte Nr. 313* (1978)
- [36] J. N. Butters, J. A. Leendertz: *J. of Measurement and Control* **4(2)** (1971) 344
- [37] Ch. M. Vest: *Holographic Interferometry* (John Wiley & Sons, New York 1979)
- [38] K. Stetson, R. Powell: *J. Opt. Soc. Amer.* **55 (12)** (1965) 1694
- [39] C. Joenathan: *Speckle Photography Shaerography, and ESPI* in *Optical Measurement Techniques and Applications* (Ed.: P. K. Rastogi, Artech House 1997)
- [40] K. Creath, G. A. Slettemoen: *J. Opt. Soc. Amer. (A)* **2** (1985) 1629
- [41] J. Slabeycius, P. Košťial, M. Držík, Š. Rosina, Jr.: *Optical observation of the dynamic tyre rubber deformations* in *Proc. of. 5th Polish Slovak Conf. Computer Simulation in the Machine Design* (Wierzba, Poland September 2000) 137
- [42] R. Jones, C. Wykes: *Holographic and speckle interferometry* (Cambridge Univ. Press, Cambridge 1983)
- [43] J. W. Goodman: *Statistical properties of laser speckle patterns* in *Laser Speckle and Related Phenomena* (Ed. J. C. Dainty, Springer-Verlag, Berlin, 1975)
- [44] K. Yamaguchi, P. B. Mellor: *Int. Journal of Mech. Sci.* **18** (1976) 85
- [45] C. Lee, Y. J. Chao, M. A. Sutton, W. H. Peters, W. F. Ranson: *Exp. Mech.* **29** (1989) 214
- [46] A. Azuchima, M. Miyagava: *Measurement of plastic zone around a fatigue crack of a stainless steel structure member with a laser beam* in *Proc. 1982 Joint Conf. on Exp. Mech.* (Hawaii 1982)
- [47] Y. Z. Dai, F. P. Chiang: *Exp. Mech.* **31** (1991) 197
- [48] M. Fukuda, K. Yamaguchi, T. Fukiage: *Preprint of Spring-time Conf. Jap. Soc. Tech, Plasticity* **57(5)** (1973)
- [49] M. Držík, L. Mach: *Staveb. čas.* **40(10)** (1992) 637
- [50] O. Ivánková, M. Držík: *Určenie plastickej zóny okolo špičky trhliny meraním svetla roypýleného povrchom* in *Proc. Exp. Mech. – Appl. Opt.* **95** (Kočkovce 1995) 113
- [51] J. Sládek, V. Sládek, M. Držík: *Int. J. of Fracture* **71(2)** (1995) 165
- [52] J. A. Ogilvy: *Theory of wave scattering from random rough surfaces* (IOP Publishing Ltd., Bristol, 1992)
- [53] S. Keil, O. Bennig: *Exp. Mech.* **19(8)** (1979) 265
- [54] W. Doetzel: *Inspection/Test/Properties of MM-Structures* in *Proc. of the NEXUS-Workshop on Micro-Machining* (Bremen 1995) 13
- [55] J. Schwider, R. Burow, K.-E. Elssner, J. Grzanna, R. Spolaczyk: *Measurement* **5** (1987) 98
- [56] O. Kafri, I. Glat: *The physics of moire metrology*, (John Wiley & Sons, New York 1989)
- [57] M. Ohring: *The materials science of thin film* (Academic Press, London 1992)
- [58] T. Lalinský: *Proceedings of the 14-th Micromechanics Europe Workshop – MME03* (Delft 2003) 45
- [59] E. Suhir: *J. of Applied Mechanics* **53** (1986) 657
- [60] T. Lalinský, M. Držík, J. Jakovenko, M. Husák: *GaAs Thermally Based MEMS Devices: Fabrication Techniques, Characterization and Modeling* in *MEMS/NEMS HANDBOOK: TECHNIQUES AND APPLICATIONS* (Kluwer Academic Press, USA 2006) 49–109
- [61] T. Lalinský, E. Burian, M. Držík, Š. Haščík, Ž. Mozolová, J. Kuzmík: *J. Micromech. Microeng.* **10(2)** (2000) 293



**Milan Držík** studied the physics at Comenius University in Bratislava. Since 1974 he has been with Slovak Academy of Sciences, now is with International Laser Centre, Bratislava. He received PhD degree in 1981. His research interests have been focused on advanced applied optics measuring methods such as conventional, holographic and speckle interferometry, laser and CCD-based techniques and their applications to solve the problems of mechanics, investigation of optical, thermophysical and mechanical properties of microstructures.



**Juraj Chlπίk** recieved his PhD degree in Optics and Optoelectronics in 2010 at the Faculty of Mathematics, Physics and Informatics, Commenius University in Bratislava. He is working as a researcher in International Laser Centre in Bratislava, and since 2008 as an Assistant Professor at the Faculty of Electrical Engineering and Information Technology, Slovak University of Technology in Bratislava. His research efforts are focused on applying of optical methods for investigation of material properties of thin layers.